# METHODS FOR DETERMINATION OF STRUCTURE AND KINETICS IN THE STUDY OF MACROMOLECULES USING DISSOLUTION DNP NMR

A Dissertation

by

HSUEH-YING CHEN

Submitted to the Office of Graduate and Professional Studies of
Texas A&M University
in partial fulfillment of the requirements for the degree of

DOCTOR OF PHILOSOPHY

| | |
|---|---|
| Chair of Committee, | Christian Hilty |
| Committee Members, | Paul Cremer |
| | Joseph Ross |
| | Dong Hee Son |
| Head of Department, | François Gabbaï |

May 2015

Major Subject: Chemistry

# ABSTRACT

Solution nuclear magnetic resonance spectroscopy (NMR) is known as a powerful tool in many fields because of its remarkable atomic resolution. However, its applications to non-equilibrium systems are limited due to low sensitivity of detection. A new technique, dissolution dynamic nuclear polarization (D-DNP) provides a unprecedented enhancement on NMR signals and opens a variety of applications of D-DNP NMR on time-resolved measurements at subsecond to second time scales. This thesis made a first attempt to monitor a protein kinetics using D-DNP NMR. A medium-size model protein (a two-state folder, L23) was directly hyperpolarized on $^{13}$C nuclei. The focus was placed on quantitative kinetic analysis and evaluations of possibilities that may affect the observed kinetics. In addition, this thesis included developments of experimental setups and NMR acquisition methods to address encountered problems in studies of large biomolecules using D-DNP.

The refolding was triggered by changing the pH environment as a result of mixing acid-denatured L23 solution with a buffer of high pH. Chemical shift changes were observed in a series of time-resolved $^{13}$C spectra, indicating the formation of secondary structures. The re-folding rate constant was extracted by fitting fractions of folded/unfolded forms to a two-state folding kinetic model taking into account non-instantaneous mixing of two solutions. The assumption of equal relaxation time constants for folded/unfolded L23 and spectral artifacts arose from one-sided reaction were validated and evaluated. Consequently, the rate constants are in good agreement with those obtained from fluorescence experiments.

In the above experiment, gas was used to inject the protein into an NMR tube. Due to turbulence from the rapid injection, protein samples are prone to foam which broadens

NMR linewidths and leads to low signal-to-noise ratio. We have developed a new method to suppress air bubbles in which water was used to inject samples into a flow cell. Because of the incompressibility of liquid, the minimized residual sample motion was demonstrated as a parallel advantage that can alleviate signal loss in measurements using pulsed field gradients. In addition, the liquid driven injection permits studying biochemical reactions at a physiological condition since no need of using a mixture of organic solvent and water to dissolve protein sample for reducing propensity of foaming as in the above study.

Conventional multidimensional NMR is not immediately compatible with the dissolution DNP to interrogate spin correlations due to the need of iterative measurements and the limitation of non-renewable hyperpolarization. We have developed a new method that integrates flow NMR into D-DNP to perform Hadamard spectroscopy and used entroy maximization algorithm to reconstruct pseudo-multidimensional spectra that contains spin correlations.

As signal enhancement is critical for experiments that directly polarize large molecules, it is beneficial to monitor hyperpolarization level in the solid state and investigate field dependence of $T_1$ relaxation during sample delivery. For this purpose, we have constructed an NMR device based on field programmable gate arrays (FPGA) and surface mount technology as an ancillary diagnostic tool.

# ACKNOWLEDGEMENTS

Foremost, I want to express my sincere gratitude to my advisor, Dr. Christian Hilty, for his guidance and patience on my experiments and my academic writing. Most importantly, he provided me so many opportunities that allow me to learn NMR spectroscopy through different projects. Although it's a little painful when facing problems in new projects, he always had valuable suggestions and ideas help me solve the problems. Without his guidance, I could not have completed those works. I will not forget these years in this lab. This is definitely an unforgettable adventure in my life.

I would also like to thank my committee members, Dr. Paul Cremer, Dr. David Russell, Dr. Joseph Ross and Dr. Dong Hee Son for serving as my committee members. I cannot believe I was able to schedule my final defense within 48 hours. Thanks for your prompt responses that let me feel less anxious. Also, thank you for the valuable suggestions and comments both in my thesis and final defense meeting. Thank you for letting my defense an enjoyable moment.

I also wish to thank my past instructors, Dr. Po-Yuan Cheng and Dr. Jim Jr-Min Lin for their encouragement to pursue my higher education. Without them, I would not have a chance to write this dissertation. I would also like to thank my group members for their help. I like to discuss with you and come up with ideas to solve problems in the experiments.

A special thanks to my family. Words cannot express how grateful I am to my parents. They always provided me unconditional supports. Even though we cannot see each other face-to-face very often, I can feel your care and love through phone. I will forever be thankful to my wife, Shu-Hua Chen, for being there with me through the good times and the bad times and my good friends, A-mau and Kissme for their inspiration.

# NOMENCLATURE

| | |
|---|---|
| BDPA | $\alpha$,$\gamma$-BisDiphenylene-$\beta$-PhenylAllyl |
| CE | Cross Effect |
| CIDNP | Chemically Induced Dynamic Nuclear Polarization |
| CPMG | Carr-Purcell Meiboom-Gill |
| D-DNP | Dissolution Dynamic Nuclear Polarization |
| DMSO | DiMethyl SulfOxide |
| DSS | 4,4-Dimethyl-4-Silapentane-1-Sulfonic acid |
| ESR | Electron Spin Resonance |
| EXSY | EXchange SpectroscopY |
| FFT | Fast Fourier Transform |
| FID | Free Induction Decay |
| FPGA | Field Programmable Gate Arrays |
| GARP | Globally optimized Alternating phase Rectangular Pulse |
| HMQC | Heternuclear Multiple Quantum Coherence |
| HPLC | High Performance Liquid Chromatography |
| HSQC | Heternuclear Single Quantum Coherence |
| INEPT | Insensitive Nuclear Enhanced Polarization Transfer |
| LLS | Long-Lived Spin |
| MAS | Magic Angle Spinning |
| MASER | Molecular Amplification by Stimulated Emission of Radiation |
| MES | 4-MorpholinoEthaneSulfonic acid |
| MRI | Magnetic Resonance Imaging |
| NMR | Nuclear Magnetic Resonance |

| | |
|---|---|
| O-DNP | Overhauser Dynamic Nuclear Polarization |
| OX63 | (tris-(8-carboxyl-2,2,6,6-tetrakis(2-hydroxyethyl) |
| | -1,3,5,7- tetrathia-2,6-dihydro-s-indacene-4-yl)methyl sodium salt) |
| PEEK | PolyEther Ether Ketone |
| PFGSE | Pulsed Field Gradient Spin Echo |
| PHIP | ParaHydrogen-Induced Polarization |
| PLL | Phase Locked Loop |
| RD | Radiation Damping |
| SE | Solid Effect |
| SEOP | Spin-Exchange Optical Pumping |
| SHOT | Scaling of Heteronuclear coupling by Optimal Tracking |
| TEMPO | (2,2,6,6-TEtraMethylPiperidin-1-yl)Oxy |
| TEMPOL | 4-hydroxy-(2,2,6,6-TEtraMethylPiperidin-1-yl)Oxy |
| TM | Thermal Mixing |
| Tx/Rx | Transmitter and Receiver |

TABLE OF CONTENTS

Page

LIST OF FIGURES

# LIST OF TABLES

# 1. INTRODUCTION

## 1.1 NMR Spectroscopy

Nuclear magnetic resonance (NMR) spectroscopy has evolved into a powerful analytical technique in the field of protein science as numerous properties of proteins can be probed by different NMR-based methods.[1,2] Protein dynamics span a wide range of time scales from femtosecond to minutes and include side chain rotation, loop motion, molecular tumbling and folding. Many protein conformational changes can be investigated using nuclear spins as a probe. Although the molecular system is at equilibrium conditions, protein dynamics can be derived from different NMR parameters.[3] For example, using EXchange SpectroscopY (EXSY), the association/dissociation rate constants in a protein-ligand complex system that undergoes an exchange on a timescale from ms to seconds can be derived by fitting signals of diagonal and cross peaks obtained at different exchange times to a two-state exchange model.[4] Relaxation measurements are often used to exploit fast conformational exchange processes on a timescale of ps to ms. For instance, interconversion rates between different intermediates in the catalysis cycle of dihydrofloate reductase has been interrogated using a Carr-Purcell Meiboom-Gill relaxation dispersion (CPMG RD) measurements.[5] The transverse relaxation rates obtained from the CPMG experiment are dependent on parameters such as exchange rates between states, populations of states and chemical shift difference between states. Thus, CPMG experiments can provide informative insights on kinetics and structures.[6] On the other hand, real-time NMR is a relatively straightforward approach in which direct time-dependence of NMR signals are monitored while the molecular system is under a non-equilibrium condition. The applicable timescale is from subsecond to minutes and corresponding conformational changes on this timescale include folding, proton exchange with solvents, and relatively slow *cis*-

*trans* proline isomerization or domain motions. For instance, a folding intermediate of $\beta$2-microglobulin protein has been characterized at a high magnetic field (800 MHz) in real time[7] by acquiring multi-dimensional NMR spectra. Two important keys are responsible for success of this experiment. First, NMR acquisition time for multi-dimensional spectra is greatly reduced by implementing fast pulsing techniques such as BEST-HSQC, SOFAST-HMQC.[8,9] Second, the lifetime of this intermediate is quite long ($\sim$ 20 mins), allowing sufficient time for signal averaging and signal sampling on indirect dimensions. However, most of the events related to protein folding such as formation of secondary structures and tertiary contacts are fast, and the lifetime of folding intermediates is often short.[10] In addition to fast acquisition techniques, a number of emerging techniques that can significantly enhance NMR signals are developed[11] to remove signal averaging. Combing the advantages of rapid acquisition and signal enhancement, the time resolution can be improved and faster kinetics cant be directly studied by using real-time NMR.

## 1.2 NMR Sensitivity

The NMR signal is proportional to the total number of the spins, but the effective factor for available signals lies in the spin population difference among the Zeeman states.[12] For a spin-1/2 nuclear spin system at thermal equilibrium, spins will populate either the $\alpha$ state ($m_{\mathrm{I}}$=1/2, lower energy) or the $\beta$ state ($m_{\mathrm{I}}$=-1/2, higher energy)[a] following the Boltzmann distribution. The normalized population difference between two states can be quantitatively described using a term, *spin polarization* as expressed in Equation (1.1)

$$P = \frac{N_\alpha - N_\beta}{N_\alpha + N_\beta} = \tanh\left(\frac{\gamma\hbar B_0}{2k_B T}\right) \sim \frac{\gamma\hbar B_0}{2k_B T} \tag{1.1}$$

where $N_\alpha$ and $N_\beta$ are number of spins at $\alpha$ and $\beta$ states, $\gamma$, $B_0$ and $T$ are the gyromagnetic ratio, strength of the applied magnetic field and absolute sample temperature, $\hbar$ and $k_B$

are the Plank and Boltzmann constants. In a higher magnetic field, signals from the same number of spins are stronger given that other experimental conditions are the same. However, if the population is equalized, there will be no detectable NMR signals because of zero difference in populations. In addition to field strength, spin polarization is dependent on types of spin and temperature. For an illustration, the polarization of electron, $^{13}$C and $^{1}$H spins are selectively plotted as a function of temperature at $B_0$=9.4 T and 3.35 T (two available magnetic fields in our lab) in Figure 1.1. At 298 K, for the most abundant nuclei, $^{1}$H, nuclear spin polarization in a 400 MHz (9.4 T) NMR spectrometer is only 0.0034%. In other words, only about one thousandth of molecules contribute to NMR signals. Compared to other commonly used optical detection methods, the nuclear magnetic resonance is hence an extremely insensitive technique. Despite low detection sensitivity, because nuclear spins are sensitive to the surrounding chemical environments, NMR spectroscopy is an indispensable analytical tools with atomic resolution in various research fields.

During the 60-year development of the NMR technology, detection sensitivity has been increasingly improved by using different strategies. Equation (1.2) summarizes parameters that govern the signal-to-noise ratio (SNR) in NMR measurements, including number of spins (n) in the detection region, the gyromagnetic ratios of excited nucleus ($\gamma_e$) and detected nucleus ($\gamma_d$), static magnetic field ($B_0$), current ($I_{coil}$) applied on the coil and the corresponding $B_1$ field, receiver bandwidth ($\Delta f$), temperature of the coil and samples ($T_c$ and $T_s$), resistance of the coil ($R_c$), induced resistance by samples in the coil ($R_s$) and noise temperature of the preamplifier ($T_a$).[14–16]

$$\frac{S}{N} \propto \frac{n \cdot \gamma_e \sqrt{\gamma_d^3 \cdot B_0^3} \cdot (B_1/I_{coil})}{\sqrt{4k_B \cdot \Delta f \cdot (R_c \cdot (T_c + T_a) - R_s(T_s + T_a))}} \tag{1.2}$$

[a]The $\alpha$ state always refers to the state with lower energy where the magnetic dipole moment is in parallel with the applied field, but the sign of the associated spin quantum number is dependent on the sign of the gyromagnetic ratio.[13]

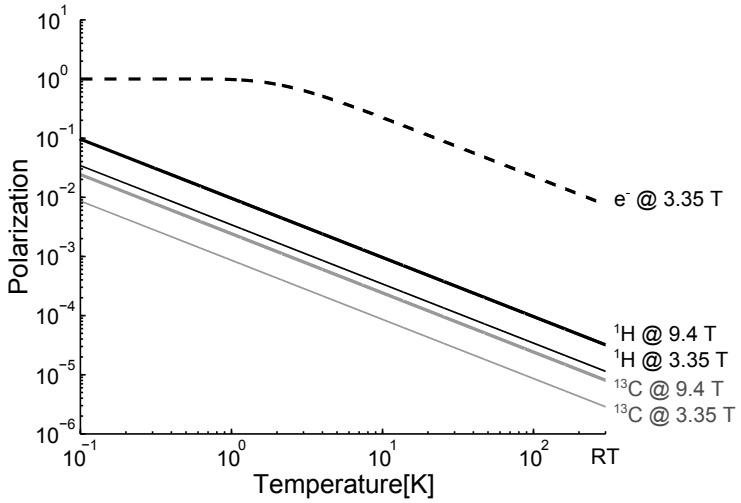


Figure 1.1: The polarization of electron, $^{13}$C and $^{1}$H spins at 9.4 T and 3.35 T at different temperatures plotted in a logarithmic scale. Two field strengths are chosen according to magnetic fields available in our lab.

Efforts were first devoted to increasing the magnetic field strength ($B_0$) to gain better SNR (nonlinearly proportional to $B_0$). However, the enhancement is limited to within an order of magnitude, as field strength of a commercially available magnet at present is about 23.5 T. In addition to the increased sensitivity, an improvement in spectral dispersion (linearly proportional to $B_0$) is a parallel advantage.[17] Various pulse sequences were developed to transfer spin polarization from nuclei of the larger gyromagnetic ratios to a smaller one for enhancement of the sensitivity.[18,19] For example, compared to a one-dimensional direct $^{13}$C measurement ($\gamma_e = \gamma_d = \gamma_C$), a gain of 4 in sensitivity is achieved by transferring magnetization of proton nuclei (covalently bonded to $^{13}$C nuclei of interest) to carbon nuclei for detection since in this case, the $\gamma_e = \gamma_H$ and $\gamma_d = \gamma_C$. Similarly, in a heternuclear chemical shift correlation measurement, higher sensitivity can be obtained by both exciting and detecting the nucleus of the larger gyromagnetic ratio, while the spin evolution takes place on the nucleus of the lower gyromagnetic constant.[20] More recently, reduction of noise has further increased the sensitivity. The strategy is to manipulate pa-

rameters of $T_c$ and $T_a$ in Equation (1.2) by using cooled He gas to lower the temperature to $\sim$ 20 K so that thermal noise from electronic circuits are minimized. Consequently, a 3 – 4 times enhancement of the detection sensitivity compared to corresponding room temperature probes is readily achieved.[16]

In addition to using higher magnetic field to generate a larger nuclear spin polarization, a variety of techniques have been developed to create highly non-equilibrium spin populations among nuclear Zeeman levels with respect to thermal equilibrium, *i.e. hyperpolarization*. Methods that have been used to generate hyperpolarization include spin-exchange optical pumping (SEOP),[21,22] photochemically induced dynamic nuclear polarization (photo-CIDNP),[23,24] parahydrogen-induced polarization (PHIP)[25,26] and microwave driven dynamic nuclear polarization (MWDNP).[27,28] In PHIP, the population difference between spin states is increased when parahydrogen is incorporated into unsaturated molecules of interest. As for photo-CIDNP, a radical pair in a photochemical system composed of target molecules and dye photosensitizers is responsible for non-Boltzmann nuclear spin distribution. SEOP and MWDNP are based on the same idea that a nuclear spin ensemble of interest is coupled to a spin reservoir of larger polarization. A substantial nuclear polarization is then created by transferring polarization from the reservoir to nuclear spins. The most common source of polarization is the electron spin, since it has significantly larger polarization than the nuclear spin at the same magnetic field and temperature as shown in Figure 1.1. Details of these methods and comparison among them have been thoroughly reviewed and discussed.[11,29] All of above-mentioned hyperpolarization techniques are able to enhance signals in solution NMR, but not all of them are applicable to the same variety of molecules. For example, only the molecules that are capable of binding with noble gas such as $^{129}$Xe, are compatible with the SEOP method; besides, the NMR detection is limited to $^{129}$Xe. Photo-CIDNP is applicable to molecules contain-

ing solvent-exposed aromatic amino acids. For hydrogenative PHIP, only samples that can undergo covalent modification can be polarized; however, recently a new approach using a metal center as medium for polarization transfer has been developed to overcome this limitation.[30] On the other hand, microwave driven DNP is applicable to a number of nuclei to create considerable polarization without too many restrictions on the type of molecule. For instance, nuclei such as $^{1}$H, $^{19}$F, $^{13}$C, $^{15}$N, $^{31}$P, $^{89}$Y, $^{107}$Ag/$^{109}$Ag, and quadroploar nuclei such as $^{2}$H have been successfully polarized in the solid state.[31–33] Therefore, microwave driven DNP is becoming a promising technique to boost NMR signals in various research fields.[34,35]

## 1.3 Microwave Driven Dynamic Nuclear Polarization

### *1.3.1 Mechanisms for Continuous Wave DNP*

To understand mechanisms of the dynamic nuclear polarization process, an electron-nuclear spin system is described in the view of quantum mechanics by a generalized Hamiltonian:

$$H = H_e + H_n + H_{ee} + H_{en} + H_{nn} \tag{1.3}$$

where $H_e$ and $H_n$ are the Zeeman Hamiltonians of electrons and nuclei. $H_{ee}$ and $H_{nn}$ are electron-electron and nuclear-nuclear interactions. The most important term for the DNP is $H_{en}$, the hyperfine interaction which in general can be split into an isotropic term and an anisotropic term:

$$H_{en} = H_{en}^{iso} + H_{en}^{aniso} \tag{1.4}$$

The isotropic part (orientation-independent) is due to the nonzero electron density at the nuclear site. In contrast, the anisotropic part denotes the interaction between nuclei and electrons which locates in the non-spherical orbital.[36]

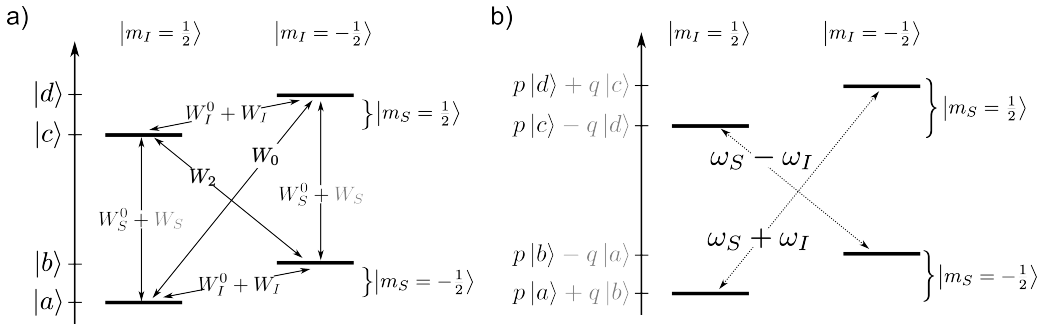


Figure 1.2: The energy levels of an electron-nucleus ($I$=1/2) spin pair system a) Time-dependent hyperfine interaction allows the cross-relaxation via flip-flop ($W_0$) and flip-flip ($W_2$) transitions. $W_S$ and $W_I$ are electron and nuclear spin relaxation through mechanisms of hyperfine coupling; however, $W_S^0$ and $W_I^0$ are intrinsic electron spin and nuclear spin relaxation via other mechanisms. b) Due to the nonzero non-secular part in the anisotropic interaction, the four pure states are partially mixed. The small contributions from other states are indicated in a gray color. $p$ and $q$ are fractions of each of pure states. $\omega_S$ and $\omega_I$ are electron and nuclear Larmor frequencies.

The time-dependence of the $H_{en}$ determines the type of mechanism in the DNP process. When $H_{en}$ is time-dependent in a scale of $\omega_e^{-1}$ (the inverse of electron Larmor frequency), the Overhauser effect is responsible for the DNP process.[37–39] The process is thus termed as Overhauser DNP (O-DNP). The feature of time-dependent Hamiltonian in liquid or metal renders the mutual spin transitions $W_0$ and $W_2$ become effective (*i.e.* cross relaxations) as shown in the Figure 1.2a. In the case of pure dipolar coupling (the anisotropic term only), the relaxation through $W_2$ dominates, which results in enhanced NMR spectrum with opposite phase to the non-enhanced signal. When scalar coupling dominates (the isotropic term only), however, $W_0$ is responsible for enhanced nuclear polarization. The maximal enhancement occurs when the irradiation of microwave $\omega$ is the same as $\omega_e$.[40]

DNP also occurs in dielectric solids, but follows different mechanisms from that in liquid, because $H_{en}$ is time-independent in this case.[36,41] This leads to the mixing of the four pure states in an electron-nucleus spin system as shown in Figure 1.2b. The mixing

of states allows the original forbidden electron spin resonance (ESR) transitions (ESR selection rule: $\Delta M_s = \pm 1, \Delta M_I = 0$).[42] Although the mixing coefficient $q$ is small (on the order of $10^{-3} - 10^{-4}$), the consequence of mixing enables the polarization transfer from direct irradiation of microwave at $\omega_S \pm \omega_I$ and causes the zero or double quantum transition, resulting in enhanced nuclear polarization. This DNP process is termed as the solid effect (SE). As the transition probabilities are proportional to $\omega_I^{-2}$, the enhancement of nuclear polarization caused by solid-effect is restricted at high field. The thermal mixing effect (TM) is another common mechanism that causes DNP in dielectric solids. TM takes place when the concentration of unpaired electrons is large so that the ESR line is homogeneously broadened by multiple dipolar coupled electrons, and thus becomes comparable to $\omega_n$. The maximal enhancement occurs when microwave frequency $\omega \approx \omega_e \pm \delta\omega_{e1/2}$ (here, $\delta\omega_{e1/2}$ is the homogeneous half width of the ESR signal). At high magnetic field, however, a mechanism called cross-effect (CE) becomes important for the DNP process. In CE, the three spins are involved (two dipolar coupled electron spins and one nuclear spin). When the relation in Equation (1.5) is satisfied, the efficiency of the DNP is dramatically improved.[43] Here, $\omega_{e1}$, $\omega_{e2}$ and $\omega_n$ are precession frequencies of electron spins and the nuclear spin.

$$\omega_{e2} - \omega_{e1} = \omega_n \tag{1.5}$$

The three different solid-state DNP mechanisms can be distinguished from the relations between ESR inhomogeneous breadth ($\Delta$), ESR homogeneous line broadening ($\delta$) and nuclear Larmor frequency ($\omega_n$). Table 1.1 summarizes the conditions required for the corresponding DNP processes.

Table 1.1: The requirements for different DNP mechanisms in the dielectric solid.[44]

| Mechanism | Solid effect | Cross effect | Thermal mixing |
|---|---|---|---|
| Conditions | $\delta, \Delta < \omega_n$ | $\delta < \Delta < \omega_n$ | $\omega_n < \delta, \Delta$ |

### *1.3.2 Optimization of Enhancement in Solid State*

In practice, stable radicals (a source for electron spins), microwave irradiation and low temperature are basic elements for nuclear polarization enhancements. As indicated in Figure 1.1, a better electron reservoir can be prepared by decreasing the temperature. A few stable radicals commonly used in DNP are shown in Figure 1.3a. For example, water soluble radicals, nitroxides (TEMPO, TEMPOL) and trityl radicals (OX63, Finland) are often used for $^{1}$H and $^{13}$C hyperpolarization, respectively.[39] For polarizing organic samples, the hydrophobic BDPA radical is one of the candidates.[45] Besides stable radicals, a co-solvent that can form an amorphous solid (glassing solvent) with the sample of interest is also important to ensure the homogeneous distribution of radicals. Some glassing solvents, such as sulfolane-based matrices, allow to polarize water soluble compounds with BDPA radicals.[45] Polarization transfer from electron spins to nearby nuclear spins is just an initiation of the DNP process. A subsequent spin diffusion effect is required to spread hyperpolarization to the entire nuclear spin network.[39] Therefore, it has been shown that an additional enhancement up to 15 times for $^{13}$C labeled amino acids was obtained by adding $^{13}$C solvents as a copolarizing agent to increase spin diffusion.[46] Moreover, the lanthanide ion such as $Gd^{3+}$ is added in the sample to further enhance the solid-state polarization by decreasing the electronic spin lattice relaxation time ($T_{1e}$) of the free radical electrons.[47] Deuteration of glassing solvents has been reported to have different effects on enhancement depending on the ESR linewidth of the free radical in use. For example,

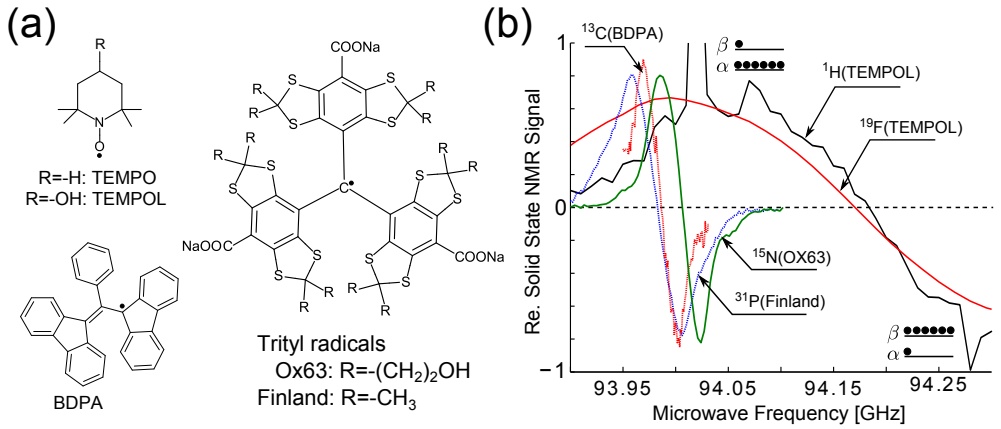


Figure 1.3: a) Typical radicals used in D-DNP such as TEMPOL used for $^{1}$H polarization, and BDPA used to polarize $^{13}$C of organic samples. OX63 and Finland are ofter used for $^{13}$C polarization of water soluble samples. b) Microwave frequency dependence (”sweep”) of selected nuclei shows that spin population can be manipulated by microwave frequency. At positive maximum of signal in each sweep, the nuclear spins populate at lower energy state mostly dominate; in contrast, negative signals indicate that the spin population is inverted.

the $^{13}$C polarization was further enhanced 2 – 3 fold when the sample was doped with the galvinoxyl radical that has large electron spin linewidth.[48] In addition, various rigid biradicals have been customized and studied in order to utilize the most efficient DNP mechanism (cross-effect) in the high field.[43,49]

Figure 1.3b shows the microwave frequency-dependence of NMR signals (frequency sweep) from several nuclei at magnetic field of 3.35 T (field strength of the HyperSense Polarizer in our lab) at 1.4 K. Profiles of frequency sweep depend on the radicals involved, but all have the same feature of one positive and one negative maximum. When applying different frequencies of microwave, different electron spin resonance (ESR) transitions are saturated. As a result, the nuclear spins are mostly accumulated at either the $\alpha$ state or the $\beta$ state (assuming a spin-1/2 system) at the corresponding microwave frequency (see mechanism section 1.3.1).

### *1.3.3 Applications of Solid-State DNP NMR and Overhauser DNP NMR*

DNP has been combined with magic angle spinning (MAS) to improve the spectral signal-to-noise ratio in solid-state NMR spectroscopy.[50] For example, a DNP-assisted solid state MAS NMR experiment on T4 lysozyme shows ~50 times enhancement on one-dimensional signals of $^{15}$N alanine amide at a magnetic field of 5 T and temperature of 90 K.[51] The total experimental time was about 40 minutes since 64 scans were averaged. In each scan, polarization time and NMR recycle delay are 20 and 15 seconds. To achieve the same SNR without DNP enhancement, 160,000 scans are required, leading to an extremely long experimental time. Therefore, by coupling DNP to solid-state MAS NMR, it becomes feasible to acquire multi-dimensional spectra within a reasonable experimental time, enabling the structural studies of proteins that are not accessible via solution NMR spectroscopy or X-ray crystallography such as amyloid and membrane proteins.[34] For instance, the rapid acquisition of a $^{13}$C – $^{13}$C correlation spectrum of a crystalline peptide (100-200 nm) from yeast prion proteins has been demonstrated.[52] Well resolved signals with high SNR prove the potential of solid-state DNP NMR on studies of heterogeneous biological systems. In addition, with the development of high frequency microwave sources such as gyrotron oscillators, DNP can be applied to solid-state NMR at fields up to 800 MHz for utilizing the benefit of high spectral resolution at high fields.[53]

Water polarized via Overhauser DNP has been used as a contrast agent for *in-vivo* magnetic resonance imaging (MRI).[54] In addition, it can be used to site-specifically investigate protein dynamics. For instance, when a protein is labeled with paramagnetic spin probes at specific sites in an aqueous solution, the surrounding water molecules can be locally polarized via O-DNP. The selective signal enhancement hence reports the surface and internal hydration dynamics of the protein, providing valuable information on solute-solvent interactions.[55] Although excessive heating of aqueous samples can become an

issue in biomolecular applications due to microwave absorption of water molecules, novel designs of microwave cavities have been reported to overcome this problem.[56,57] However, the applications so far are limited to water or small molecules and enhancements become lower at high fields.[11]

## 1.4 Dissolution Dynamic Nuclear Polarization NMR Spectroscopy

In addition to directly hyperpolarizng samples in the liquid state via the Overhauser effect, hyperpolarization generated in the solid state can be brought into a solution phase[58] so that not only the advantage of high atomic resolution in solution NMR but also a larger enhancement can be obtained.[59] Figure 1.4a shows a picture of a commercial HyperSense polarizer (Oxford Instruments, Abingdon, UK), rapid sample injectors and a 400 MHz spectrometer (Bruker) in our lab. The corresponding schematic is displayed in Figure 1.4b. Two separate magnets are involved in a typical experimental configuration; one for dynamic nuclear polarization and one for NMR measurement (also known as ex-situ DNP NMR). Nuclear hyperpolarization of target samples is first created at a low magnetic field (3 – 5 T), in the solid state at low temperature ($\sim$ 1.4 K). Afterwards, the frozen sample is rapidly dissolved and transfered to another magnet of higher field at room temperature for NMR measurements. The technique is thus termed dissolution dynamic nuclear polarization NMR spectroscopy (D-DNP NMR). Either high pressure gas or liquid can be used as driving forces to deliver dissolved samples through tubing into the NMR detection region. A selection of important parameters for the measurement is shown in Figure 1.4c. For example, the sample will experience a field cycle from 3.5 T to one near to the Earth's field, and finally to a measurement field. Theoretically, the maximal enhancement in the solid state can be obtained via DNP is the ratio of gyromagnetic constants of electron spin and nuclear spin, $\epsilon_0 = \gamma_e/\gamma_n$.[39] However, as expressed in the Equation (1.6), the change

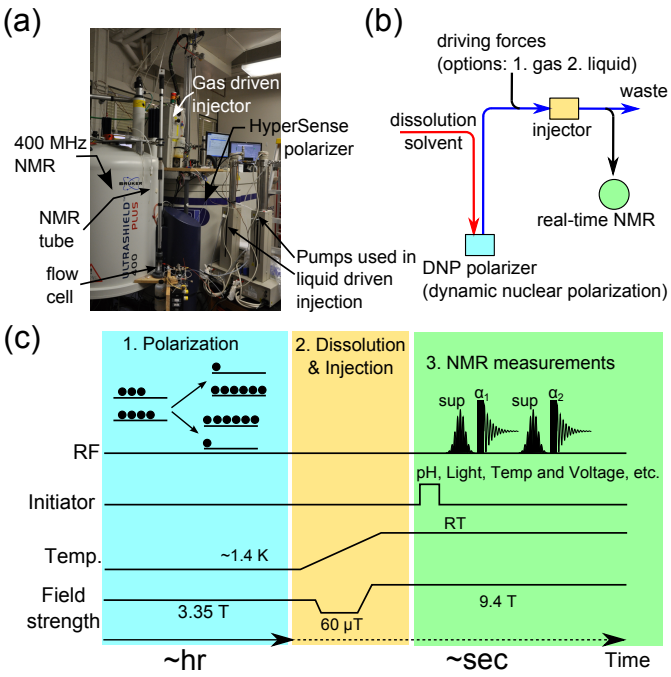


Figure 1.4: (a) A picture of a D-DNP coupled NMR spectrometer with sample injectors. (b) A schematic diagram of experimental setups for D-DNP NMR. (c) Three basic steps of the experiment and major parameters in each step. The time axis is not linearly scaled. The polarization stage takes 30 mins to a few hours depending on the type of nuclei. Time required for the dissolution process and the NMR measurement is within a few seconds.

of temperature in D-DNP results in an additional enhancement, making D-DNP an excellent technique to boost solution NMR signals. It has been reported that an enhancement >10,000 was readily achieved.[58] It is noted that Equation (1.6) is assuming that the polarization is linearly proportional to temperature (see Equation 1.1 and Figure 1.1).

$$\epsilon = \epsilon_0 \frac{B_{DNP} T_{NMR}}{B_{NMR} T_{DNP}} \tag{1.6}$$

### *1.4.1 Optimization of Enhancement and Efficiency*

In order to maximize electron polarization, samples doped with stable radicals are first cooled by using liquid helium. As displayed in the Figure 1.1 (dashed line), the electron polarization at a magnetic field of 3.35 T closes to the maximum when temperature is approaching ~1 K. While applying microwave irradiation on frozen samples, the polarization increased over time and the build-up rate is dependent on the type of nucleus. As shown in Figure 1.5 (0 – 15000 s), the build-up time for proton is about 30 mins; however, for nuclei of low-gyromagnetic ratio such as $^{13}C$, polarization build-up time can be longer. Doping lanthanide ions such as $Gd^{3+}$ and $Ho^{3+}$ in the polarized samples were found to increase the solid-state $^{13}C$ polarization and to shorten the build-up time.[60] In addition, utilizing cross polarization from proton to carbon has been shown to greatly reduce the build-up time; however, additional requirements on design of the cryogenic probe and polarization transfer methods are required to minimize arcing of the probe in the helium gas atmosphere due to the use of high power pulses of radio frequency.[61,62]

After the hyperpolarization has been created, the samples need to be dissolved and brought into the NMR magnet as quickly as possible due to the limited lifetime of hyperpolarization that is governed by the spin lattice relaxation ($T_1$ relaxation). In general, as illustrated in Figure 1.5 (15000 – 15015 s), hyperpolarization of larger molecules decays more rapidly than for small molecules. Several strategies can be employed to retain the hyperpolarization. For example, time required for sample delivery is shortened by utilizing a high pressure gas to inject the hyperpolarized (HP) sample into an NMR tube pre-placed in a high-resolution magnet.[63] As a result, the measurement dead time has been reduced to about 1–2 seconds given that traveling distance of samples is about 3.5 m long. Shortening the distance between polarizer and high-resolution magnet is proposed by Leggett et al. to further reduce the loss caused by spin relaxation.[64] A single magnet designed with two

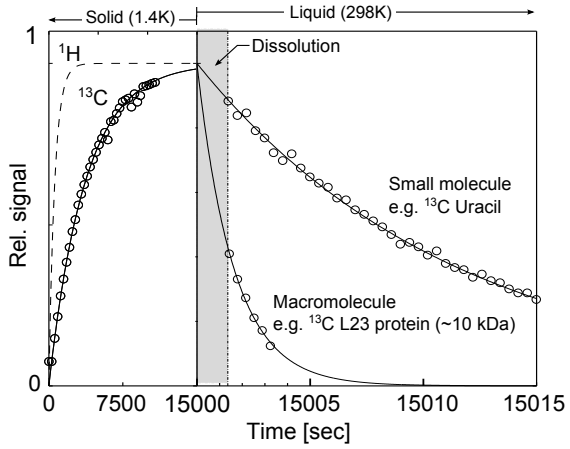


Figure 1.5: A composite diagram showing the build up curves of proton and carbon polarization in solid-state at 1.4 K (0 – 15000 s) and hyperpolarization lifetime of two molecules of different molecular sizes in liquid state (15000 – 15015 s). It is noted that the signal in the solid and liquid states cannot be compared directly. The grey strip indicates the dead time of the NMR measurement, required for dissolution and delivery of HP samples.

isocenters has been constructed to polarize target samples in an upper compartment (3.35 T) and to perform high resolution NMR measurements in a lower compartment (9.4 T). Thus, the distance between polarization and measurement locations was reduced to 80 cm and larger enhancement can be obtained. As dipolar interactions play the most important role on the $T_1$ relaxation in solution NMR, substitution of $^1$H covalently bonded to $^{13}$C nuclei with $^2$H to increase relaxation time constants is an alternative way to reduce the loss of $^{13}$C signal during the dissolution process.[65,66] In addition, gently heating dissolved samples during the transportation can increase the $T_1$ relaxation time[67] by changing the rotational correlation times ($\tau_c$) of molecules.[68] Since dissolved polarized samples undergo a field cycle during transportation (Figure 1.4c), systematic evaluation on field dependence of spin-lattice relaxation times can provide valuable information for optimizing the performance of D-DNP.[69] For this purpose, auxiliary NMR devices can be used. We have developed a basic NMR device based on FPGA and surface mount technology that can be configured to acquire NMR signal of frequency ranging from ~100 kHz to 50 MHz

as described in **Chapter 6**. In addition, it can serve as a polarimetry device to monitor polarization in the solid-state during DNP process.

Although rapid dissolution/injection retains hyperpolarization, accompanied side effects can interfere the subsequent NMR measurements. For example, foam or air bubbles are likely present after dissolution and injection using gas. This outcome can lead to non-uniform magnetic field around samples so that linewidths of NMR resonances are broadened. It was proposed to use pressurized gas to suppress bubbles,[63] but for certain sample conditions, they cannot be completely removed,[70] especially when protein molecules are involved.[65] To address this issue, a binary mixture was used as dissolution solvent to decrease surface tension of solution for reducing propensity of foaming.[71] Alternatively, in **Chapter 5**, we have proposed to use pressurized fluids as a driving force for sample injection. The results suggested a better performance was offered by using liquid driven injection. In addition, this new injection method minimized residual motion (due to the rapid injection) which can be an issue in NMR measurements especially for that used pulse field gradients.

Due to the process of dissolution in D-DNP, the sample aliquot is often diluted into a larger volume than the NMR detection volume. In other words, not all of polarized sample is used in the measurements. In order to fully utilize all hyperpolarized samples from a single prepareation, as demonstrated in **Chapter 4**, we have integrated flow NMR with D-DNP to sequentially deliver HP samples that originally were dispersed in the tubing after dissolution, into a flow cell for the NMR detection. As a result, up to eight 'fresh samples' can be obtained from a single batch of hyperpolarization.[72] Typically, the dilution factor is between 100–500, depending on the initial volume polarized in the solid state.[63] This factor can be reduced by using immiscible organic and aqueous solvents to melt frozen HP samples.[67] In addition, using high power laser to rapidly melt the frozen sample (100 K) at a location where the NMR experiments will be performed has been demonstrated to not

only avoid the large dilution as in a configuration of ex-situ DNP but to extend lifetime of hyperpolarization since the $T_1$ relaxation is often slower in the solid state and in high field.[73] Although this method was implemented in solid-state DNP at temperature of 100 K, it is potentially possible to be integrated into the low temperature DNP (1.4 K).

Paramagnetic species are known to accelerate spin relaxation.[68] Therefore, the doped stable radicals in the dissolved sample will reduce the lifetime of hyperpolarization despite they were diluted in dissolution process. It is possible to remove radicals during sample delivery. For example, the ascorbic acid was mixed with dissolved HP samples to reduce TEMPOL radicals.[74] TEMPO radical can be extracted by adding organic solvent in water as dissolution solvent.[67] A simple filter consisting of a cotton plug has also been used in the tubing to remove BDPA radical.[45]

Radiation damping (RD) is an intrinsic phenomenon in NMR experiments. When a strong bulk magnetization interacts with an NMR coil of a high quality factor, a feedback field will be generated and has a reverse effect on the bulk magnetization.[75] Because of significant signal enhancement, RD is more readily present in a hyperpolarized sample. The RD effect was known as one of reasons for an observation of chaotic emissions in a hyperpolarized $^{129}$Xe polarized via SEOP.[76] In **Chapter 2**, we have investigated a hyperpolarized proton spin system and attributed multiple NMR emissions that were observed in the absence of radio frequency (RF) excitation to the effect of radiation damping. In addition, it was found that samples of negative spin temperature[b] have less enhancement than samples of positive spin temperature due to accelerated relaxation induced by RD.[77] Although the RD effect broadens NMR linewidths and shortens the recovery time from non-equilibrium back to thermal equilibrium states, several constructive applications such as a new solvent suppression scheme exist.[78]

[b] A spin system at a negative spin temperature has distribution of populations dominated at higher energy states, and vice versa.[79]

### *1.4.2 NMR Acquisition*

With the significant polarization from DNP hyperpolarization, it is possible to monitor kinetics of chemical reactions or other time-dependent events in real time with an improved time-resolution, as signal averaging is not needed. The reaction can be initiated by mixing HP samples with other reactants pre-loaded in an NMR tube or mixing with other reactant in a mixer before delivered into a flow cell. A series of RF pulses with a fixed small tip angle is then applied to acquire a set of one dimensional (1D) NMR spectra at different times. The obtained time-dependent signals cannot directly describe kinetics since the depletion of bulk magnetization resulting from applying RF pulses needs to be considered. Consequently, an additional signal decay needs to be added in the kinetic model to describe signal intensities.[80] An alternative acquisition scheme has been used to avoid the aforementioned complication. In this scheme, the tip angle of the excitation pulse is varied to project the same proportion of longitudinal magnetization for NMR detection in each scan. As a result, no modification is required in kinetic models. In addition, more uniform distribution of SNR among scans can be obtained.[81]

Chemical shift correlations in NMR spectroscopy are of considerable value, especially since they provide for structural elucidation. Multi-dimensional NMR experiments are often used to retrieve such spin correlations.[82] Due to the limited lifetime and non-renewable feature of hyperpolarization, the conventional iterative data acquisition scheme in multi-dimension NMR experiments is not immediately applicable. However, a variety of methods have been developed to retrieve such information on spin correlation in D-DNP NMR experiments. For example, one-dimensional (1D) measurements with application of continuous-wave excitation can provide $^{13}$C-$^{1}$H heteronuclear correlation by calculating the proton chemical shift from the observed coupling constant in the $^{13}$C spectrum under the influence of off-resonance decoupling.[83] A similar method using a SHOT

(scaling of heteronuclear coupling by optimal tracking) decoupling pulse has results in a linear relation between effective coupling constants and decoupling frequency offsets, providing better accuracy of chemical shift determination.[84] The above-mentioned 1D measurements require resolved chemical shifts in the detection dimension. In contrast, a little modification on a conventional $^{13}$C-$^{1}$H heternuclear multiple quantum coherence (HMQC) experiment allows one to sequentially acquire two-dimensional (2D) spectra from hyperpolarized samples, and hence to resolve overlapping resonances. Moreover, instead of using the conventional evolution time incremented scheme, the ultrafast single-scan NMR methodology has shown promising acquisitions of 2D NMR spectra with measurement time in the order of 100 ms, making it particularly well suited for D-DNP.[85] In ultrafast 2D NMR, the sample is spatially encoded using two chirped $\pi$ pulses with the same sweep direction[c] but under reverse gradients. Since spins at different positions in the sample are excited sequentially by the chirped pulses, different phases are accumulated, resulting magnetization helices with their pitch of winding proportional to indirect chemical shifts ($\Omega_1$).[86] After coherence is transfered between the correlated spins, field gradients are applied to unwind magnetization helices to decode the previous $\Omega_1$ labeling, resulting in a time-domain data that is equivalent to a spectrum in indirect domains. The subsequent readouts are repeated with the field gradient reversed back and forth several times and finally a mixed frequency/time-domain interferogram is obtained. Then, a 2D NMR spectrum can be reconstructed by a 1D Fourier transformation.[87]

Alternatively, direct frequency-encoded Hadamard spectroscopy (non-Fourier method, signal from the entire sample) can be implemented to acquire multi-dimensional NMR spectra. In this method, the spectral regions without the NMR resonances present are not sampled; therefore, the acquisition is accelerated.[88] Recently, a combination of ultrafast and Hadamard measurements (single-scan 2D Hadamard spectroscopy) has been demonstrated to perform fast acquisition.[89] In **Chapter 4**, we have combined flow NMR

with D-DNP to perform the original multi-scan Hadamard spectroscopy on a sequentially injected hyperpolarized samples.[72] Since NMR signal from the same resonance has non-identical intensity among scans due to spin relaxation and concentration difference, the conventional Hadamard reconstruction procedure cannot provide distinct and correct spin correlations. We have adopted an algorithm of entropy maximization to quickly scale amplitude of each scan and obtained well-resolved pseudo-2D correlation spectra without prior knowledge of spin relaxation and concentration distribution in the tubing.

### *1.4.3 Applications of D-DNP NMR*

Combining the advantage of high site resolution and the improved time resolution benefiting from the enhanced signals, D-DNP has become an emerging technique for applications of real-time NMR or MRI.[39,59,90] Currently, predominant applications are in the area of *in-vivo* detection of $^{13}$C labeled metabolic molecules using MRI. Conventionally, measurements of MRI mostly detect proton nuclei because of the features of high natural abundance. However, recently, hyperpolarized $^{13}$C labeled molecules are introduced to overcome disadvantages of using $^{1}$H as target nuclei, including limited range of proton chemical shifts of metabolites and interference from huge solvent signals. Development of D-DNP $^{13}$C MRI was first focused on the area of angiography in which endogenous substrates of lower toxicity to living organism were used. Urea ($NH_3$), a metabolic product of proteins, is one such substances, with a natural concentration of 1-10 mM in the blood and body fluids. It has been shown that $^{13}$C angiography with a SNR of $\sim$ 275 was obtained by injecting $^{13}$C urea into a rat.[91] Many other hyperpolarized $^{13}$C molecules were used in real-time metabolic MRI.[92] Figure 1.6 lists some commonly used substrates for

[c] A chirped RF pulse has its phase varied as a function of time, leading to different excitation frequencies at different time. Frequency can sweep from high to low values or *vice versa*, depending on how the phase is varied.

*in-vivo* metabolic applications, including pyruvate, dehydroascorbate and fumarate.[93–95] All of them feature low toxicity, rapid uptake and fast conversion to metabolic products. Carbonyl carbons are used as target nuclei because of their long $T_1$ relaxation time. As a result, the hyperpolarization can be preserved for a longer time and hence a wider detection time window is possible. For example, 1-$^{13}$C pyruvate has been used as a tracer to map the distribution of metabolic products. A quantitative measurement of 1-$^{13}$C pyruvate transportation and 1-$^{13}$C lactate levels (metabolic products) in the normal brain of rat were obtained.[96] In addition, many studies of cancer diseases in animal models using $^{13}$C DNP metabolic MRI have been demonstrated.[97,98] The signal levels of $^{13}$C pyruvate and its metabolic product, $^{13}$C lactate were found significantly higher in tumors than normal tissue of rat brain.[99] Dissolution DNP has also been developed toward clinical applications. For example, an instrument has been designed to include sterile environment throughout the polarization and dissolution processes for a clinical purpose.[100] Moreover, hyperpolarized $H^{13}CO_3^-$ has been proposed as an non-toxic pH probe for high resolution human pH imaging[101] as the tissue pH can be altered through many pathological processes such as cancer, inflammation and ischaemia. The pH values can be calculated from relative concentrations of $H^{13}CO_3^-$ and $CO_2$. Without signal enhancement from DNP, it is difficult to measure this relative ratio, as the plasma bicarbonate concentration in humans is $\sim$ 24 mM and the natural abundance of the $^{13}$C nucleus is low (1.1%). Furthermore, hyperpolarized $^{13}$C, $^{2}H_7$-glucose has been used to study metabolic processes in living human breast cancel cells.[102] Kinetics of the product, lactate, was characterized by the Michaelis-Menten equation, and glycolytic intermediates such dihydroxyacetone phosphate and 3-phosphoglycerate were observed. Most recently, a clinical trial of $^{13}$C MR metabolic imaging in patients with prostate cancer has been successfully conducted.[103] The results confirmed the safety of using $^{13}$C substrates in humans and showed elevated ratio between lactate and pyruvate in regions where cancer cells exist.

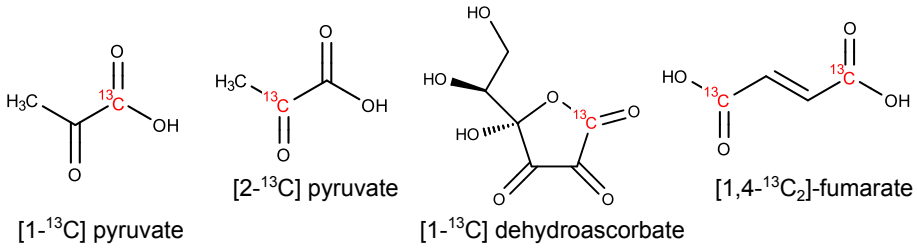


Figure 1.6: Commonly used hyperpolarized substrates for *in-vivo* metabolic studies using D-DNP NMR, such as 1-$^{13}$C pyruvate, 2-$^{13}$C pyruvate, 1-$^{13}$C dehydroascorbate and 1,4-$^{13}C_2$ fumarate.

Besides *in-vivo* experiments, D-DNP NMR has already been applied to a number of *in-vitro* experiments. For instance, it has been used to monitor kinetics of reactions including polymerization, oxidation/reduction, hydration, acetylation, etc.[90] To name a few, hyperpolairzed dehydroascorbate (DHA) was chemically reduced with a reagent $NaBH_3CN$. The obtained DNP spectrum showed several resonances rather than a single peak from the reduced DHA as observed in the thermally polarized counterpart,[104] suggesting the presence of a transient tautomers of DHA during reaction. In addition, reaction intermediates in a living polymerization of hyperpolarized styrene were identified by temporal correlation experiments using selective inversion on the spins in question.[80] These experiments demonstrate the capability of D-DNP to identify the reaction intermediates that have short lifetime, which was not detectable by conventional NMR spectroscopy due to low SNR. An application to enzymatic reactions, trypsin-catalyzed conversion of $N_a$-benzoyl-L-arginine ethyl ester (BAEE) to $N_a$-benzoyl-L-arginine (BA), was first demonstrated in our group.[105] The catalysis rate has been obtained from a series of $^{13}$C time-resolved spectra over the course of 3 s. Also, enzymatic phosphorylation kinetics of glucose by a hexokinase has been studied.[106] The acquired $^{13}$C spectra in a time window of ~10 s showed phosphorylation rates of $\alpha$ and $\beta$ glucose anomers are similar. A slower reaction, adenosine triphosphate-dependent phosphorylation of choline have be followed using

quaternary $^{15}$N of choline as a target spin because of its extremely long $T_1$ relaxation time (> 200 s).[107] As shown in **Chapter3**, despite the intrinsically short $T_1$ time constant of larger molecules, by using strategies introduced in Section 1.4.1, we have investigated a re-folding process of a protein (L23, 96 amino acids) in a time period of ~2 s. These experiments proved the potential of D-DNP NMR on studying kinetics over a range of time scales.

In addition to studying kinetics, hyperpolarized small molecules can be used as a probe to interrogate molecular interactions such as protein-ligand and host-guest interactions. For example, hyperpolarized benzoic acid has been used as a contrast agent in a cyclodextrin ligand-receptor pair. Once the benzoic acid binds to $\beta$ cyclodextrin, the relaxation time constant, $T_1$ of benzoic acid will decrease. This change of spin-lattice relaxation times can be used to weight the MRI images in a cyclodextrin ligand-receptor system that is often used to mimic protein and drug molecules.[108] In addition, hyperpolarized fluorinated ligands have been used to evaluate protein-ligand binding constants,[109] which is important in the field of drug discovery. Detecting $^{19}$F signals of ligands instead of $^{1}$H is beneficial due to the absence of interference from signals of solvents. For those drug candidates containing no fluorine atoms, hyperpolarized fluorinated ligands can be used as reporters to obtain dissociation constants using a single-scan CPMG experiment, without the need of titration.[110] Moreover, in the case of competitive binding, site-specific information on binding pocket in a protein-ligand system can be obtained by observing magnetization transfer between two ligands, known as the INPHARMA experiment.[111] This magnetization transfer relies on the nuclear Overhauser effect (NOE)[d] and is mediated by the protein. With the hyperpolarization offered by DNP, signals due to this NOE effect can be enhanced.[112] Similar, the $^{15}$N signals of amino acids have been amplified by a combination of chemical exchange and the NOE effect.[67] Water molecules were first hyperpolarized and the protons were exchanged with amide protons. Due to spontaneous one-bond Overhauser

processes, $^{15}N$ signal enhancements > 500 at 11.7 T has been observed. This result opens possibilities to investigate interesting interactions between solutes and different solvents.

Combing enhanced SNR from dissolution DNP with high spectral resolution inherently from liquid NMR, dissolution DNP-NMR has become a useful tool to investigate chemical systems that have previously been impossible to access, including those systems that are in a non-equilibrium state.

[d]Nuclear Overhauser effect is similar to Overhauser effect introduced in the liquid state DNP (see Section 1.3.1). The interactive partner are two nuclear spin instead of one nuclear and one electron spins.

# 2. SPONTANEOUS EMISSION FROM HYPERPOLARIZED $^{1}$H SPIN SYSTEM*

## 2.1 Introduction

Hyperpolarization of nuclear spins is gaining considerable momentum for the enhancement of the signal in magnetic resonance, with applications ranging from medical imaging to high-resolution spectroscopy of chemical compounds. In the widespread application of hyperpolarization, however, it is often overlooked that due to the highly polarized spin system, effects not commonly encountered in conventional NMR spectroscopy need to be considered. Such effects include phenomena related to the emission or absorption of spin noise that have been previously described using thermal polarization,[76,113–115] but may become more prominent in hyperpolarized samples. Desvaux et al.[116] have shown that $^{129}$Xe, hyperpolarized by optical pumping, can enhance the absorption of noise at the Larmor frequency of that nucleus. Recently, the same phenomenon has been observed by Giraudeau et al.[117] using hyperpolarized $^{1}$H nuclei. However, when a sample is polarized to negative spin temperature, an unusual and chaotic behavior arises, where a series of beats of NMR signal can be observed under certain conditions. The physical origin of such spontaneous emissions has been attributed to interplay between radiation damping and the effect of distant dipolar fields. In the absence of radio-frequency pulses, it has been proposed that the emission of such bursts may be triggered by random spin noise.[118] These emissions therefore arise from positive feedback through coupling with the resonant detection coil circuit, and are different from the previously observed spontaneous emissions of signal from a saturated spin system with zero polarization.[114] The observation of noise triggered spontaneous emission is highly dependent on the conditions used, and it has also been noted that

*Reprinted from "Spontaneous Emission of NMR Signals in Hyperpolarized Proton Spin Systems" by H. Y. Chen, Y. Lee, S. Bowen and C. Hilty, *J. Magn. Reson.*, **2011**, Copyright 2010 Elsevier Inc.

observation of multiple signal emissions in hyperpolarized samples of $^1$H is less likely due to the shorter relaxation time[117] and the higher gyromagnetic ratio.[118] With the recent development of various technologies for dynamic nuclear polarization (DNP), it has become commonplace to polarize many different nuclei. Of particular importance is $^1$H, the NMR active nucleus with highest abundance. Due to the large signal enhancement provided by DNP (on the order of $10^2 - 10^4$ as compared to thermally polarized spins), applications of this technique in traditional areas of NMR spectroscopy, such as analytical and organic chemistry, are forthcoming. In this context, it may be interesting to investigate in more detail the non-canonical behavior that hyperpolarized spin systems can exhibit. Here, we show that the spontaneous emission of multiple beats of NMR signal could be observed for $^1$H nuclei when the spin system has been hyperpolarized to a negative spin temperature and the sample is injected into an NMR spectrometer for measurement. We examine the conditions under which this phenomenon can be observed, rationalize the appearance of these emissions, and discuss their implications for the application of hyperpolarized spectroscopy.

## 2.2 Experimental Section

### *2.2.1 Hyperpolarization*

The optimal frequencies for DNP polarization were determined by measuring the frequency dependence of the NMR signal in the solid state (Fig. 2.1).[31] To accomplish this, a sample of 10% $H_2O$, 40% $D_2O$ and 50% DMSO-d6 containing 15 mM free radical, 4-Hydroxy- 2,2,6,6-tetramethylpiperidine 1-oxyl (TEMPOL, Sigma Aldrich, St. Louis, MO) was irradiated for 60 s at each of 66 frequencies between 93.66 GHz and 94.31 GHz. The irradiation frequency was verified using a frequency counter (EIP 578B, Phase Matrix, San Jose, CA). NMR spectra were measured using the detection coil in the Hyper-

Sense DNP polarizer (Oxford Instruments, Tubney Woods, UK) and a separate 400 MHz NMR console (Bruker, Billerica, MA). The resulting series of free induction decays (FID) was Fourier transformed, and the frequency profile was generated by integration of each spectrum. For hyperpolarized NMR spectroscopy, samples of dimethyl sulfoxide (DMSO) were prepared in $H_2O$ (1:1 v/v) mixtures with 15 mM TEMPOL and 1 mM gadolinium diethylene triamine pentaacetic acid (Gd-DTPA, Sigma Aldrich, St. Louis, MO). 20 ul of the sample was polarized for 30 min, at a temperature of 1.4 K, using mm-waves of 100 mW power at the frequencies corresponding to positive or negative spin temperature. Subsequently, 4 mL of deuterium oxide (Cambridge Isotope Laboratories, Andover, MA) at 160 °C and 10 bar pressure was used to dissolve and carry the hyperpolarized sample into a sample injector device. The first 500 uL of the liquid was injected into a 5 mm NMR tube that was preinstalled in the NMR spectrometer, using nitrogen gas at a forward pressure of 1.8 MPa, against a back-pressure of 1.0 MPa to prevent outgassing.[63] The final concentration of hyperpolarized analyte in the NMR tube was estimated to be 115 mM DMSO and 453 mM $H_2O$.

### *2.2.2 NMR Spectroscopy*

The magnetic field was shimmed to a homogeneity < 2.5 ppb using a sample of identical volume and composition prior to the experiment. Single NMR scans were acquired either with or without prior application of a $\pi/2$ radio frequency (RF) pulse. Measurements without RF pulse were triggered at the start of sample injection, prior to the arrival of the polarized solution in the NMR tube. Measurements with RF pulse were initiated 815 ms after the start of sample injection, to ensure a sufficient amount of time for sample injection and stabilization. The total experimental time was 190 s, during which 1,201,922 complex data points were acquired. All measurements from hyperpolarized sample were

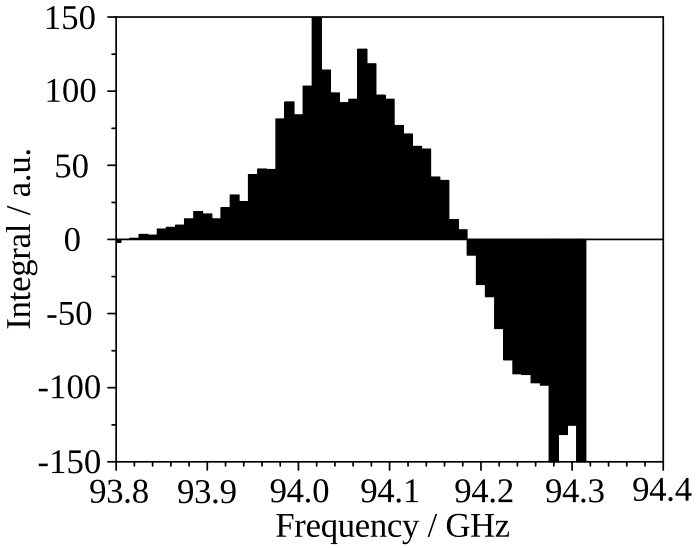


Figure 2.1: Dependence of solid-state $^1$H polarization on microwave frequency for a sample of 10% $H_2O$/40% $D_2O$/50% DMSO-d6 containing 15 mM TEMPOL free radical. Spurious points of large intensity (clipped in the figure) are likely due to arcing of the NMR coil immersed in liquid helium.

carried out without the use of a lock system. Time-frequency analysis was performed by a Fast Fourier Transform (FFT) of data contained in a sliding window of 256 complex points in length. Data processing and plotting was done in the program MATLAB (MathWorks Inc., Natick, MA). The actual timing of sample delivery (time points A and B in Fig. 2.2, for the start and end of arrival of sample in the NMR tube, respectively) was determined on a sample outside of the NMR magnet, using a camera. $T_1$ relaxation times under the experimental conditions used for the DNP experiments were estimated from hyperpolarized samples with positive spin temperature using a sequence of small flip angle excitations[81,119] as well as from inversion recovery experiments. For reference, the radiation damping time constant was measured in a non-hyperpolarized sample of 95% DMSO and 5% $D_2O$ in the 400 MHz NMR spectrometer. An inversion recovery experiment was applied as described in ref.120 and the equation (2.1) was fitted to the experimental data. Here, $M_z^{eq}$, $R_{rd}$ and $t_0$ are the initial thermal magnetization in the z direction, the radiation

damping rate, and the latency interval, respectively.

$$M_z = M_z^{eq} \tanh[R_{rd}(t - t_0)] \tag{2.1}$$

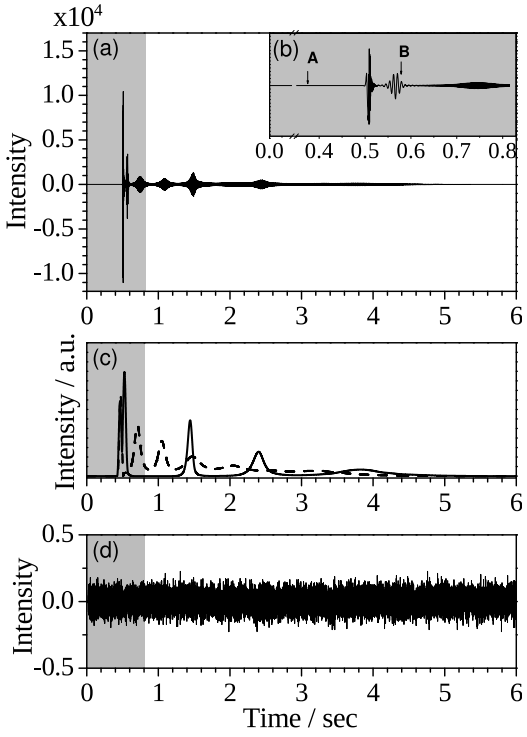


Figure 2.2: (a) Signals from a sample of DMSO/$H_2O$ (1:1 v/v) polarized to negative spin temperature and dissolved in $D_2O$. (b) Inset: expanded view of the signal in the time window from 0 to 815 ms. The time point t=0 is the point of triggering of the injection valve. The sample starts arriving in the NMR tube at time point A, and tube is completely filled at time point B. (c) The corresponding time-frequency analysis of FID (a) was performed by a FFT of data contained in a sliding window of 256 complex points in length (time window of 40 ms). The peak height of the spectra was plotted as a function of time. The solid and dashed lines refer to $H_2O$ and DMSO signals, respectively. (d) The hyperpolarized sample of DMSO/$H_2O$ (1:1 v/v) with positive temperature was dissolved by $D_2O$ and measured under early triggered acquisition mode, showing no signals inside the blind time (grey area: the time before the sample injection and stabilization in the normal measurement, 815 ms).

## 2.3 Results and Discussion

### *2.3.1 Hyperpolarization to Negative Spin Temperature*

Using DNP in the solid state, spin systems with positive or negative spin temperature are readily produced.[41] Fig. 2.1 shows the frequency dependence of polarization, recorded within the frequency range accessible by the microwave source used. The intensity maximum at 94.005 GHz corresponds to $^1$H polarization with positive spin temperature, where the majority of spins are aligned parallel with the magnetic field, and the negative intensity maximum at 94.270 GHz corresponds to the negative spin temperature, where the majority of spins are aligned anti-parallel with the magnetic field. It can also be noted that the frequency difference between the maxima is 265 MHz, which indicates that the DNP polarization process under the conditions used takes place via a multi-electron process.[121] DNP polarized samples were dissolved and injected into the NMR spectrometer in order to analyze their NMR signal. In the archetypal pulsed NMR experiment, a single $\pi/2$ radio-frequency pulse would be applied to a tuned coil surrounding the sample, and the resulting free induction decay (FID) would be observed. This experiment was used in order to estimate the level of polarization obtained, by comparison with a spectrum acquired in the same spectrometer using a thermally polarized sample. For the DMSO signal, a typical polarization level of ca. 4% is achieved, corresponding to a signal enhancement of approximately 1300 as compared to the thermal polarization in the field of the 400 MHz NMR spectrometer.

### *2.3.2 Spontaneous Signal Emission*

For a hyperpolarized sample with negative spin temperature, spontaneous emission of signals is readily observed as soon as the sample is introduced into the active region of an NMR coil, even in the absence of RF pulses. Fig. 2.2 shows such emissions from

a mixture of DMSO and $H_2O$, which was hyperpolarized on proton spins, and dissolved in deuterium oxide ($D_2O$) before injection into the NMR detection coil. Since the NMR experiments measuring spontaneous emission do not require a radio-frequency pulse, data acquisition was initiated before the solution arrived in the NMR spectrometer, in order to detect all potential signals. The grey areas in Fig. 2.2 designate the time for sample injection and stabilization that would normally elapse before the start of an NMR experiment. The data in Fig. 2.2a and b indicate the emission of strong, recurring signals, starting almost immediately after the arrival of polarized solution in the detection coil. In order to distinguish the identity of the sample constituents giving rise to the different recurring signals, a time–frequency analysis was performed by a sliding Fourier transform. The resulting peak intensity at the chemical shifts corresponding to $H_2O$ and DMSO is plotted in function of time in Fig. 2.2c. Due to substantial inhomogeneity during sample injection, the intensities obtained for the grayed time window (0–815 ms) may not be quantitative, and the signals appear less regular. Nevertheless, in Fig. 2.2b the appearance of signals with different frequency stemming from water and DMSO protons can be seen. After this time, the sample has settled, and the line width in the spectra obtained with sliding Fourier transform remains constant, since the true line width had fallen below the frequency resolution given by the window used for the Fourier transform. From Fig. 2.2, it can however be seen that the recurring beats become longer in duration at larger time. From this observation, it can be inferred that the true line width decreases with each emission. The time-frequency representation of the signal shows multiple emissions both from $H_2O$ and DMSO spins. Presumably due to chaotic processes during sample injection, if the experiment is repeated under identical conditions, the appearance of the signal can vary. However, in all experiments that were carried out, the signal between two consecutive recurrences was nonzero and the intensity of a later recurrence was smaller than that of an earlier one. In Fig. 2.2d, the measurement of a sample hyperpolarized to positive

spin temperature serves as a control experiment. The absence of coherent signal excludes the possibility that the spin emission from the other samples is due to influences unrelated to the spin system, such as electronic interferences or external excitation of the detection circuit during sample injection.

### *2.3.3 Radiation Damping*

Coherent emissions in the form of radiation damping are common from solvent signals in high-resolution NMR spectroscopy. A typical signal from radiation damping arises shortly after generating the inverted spin state in the NMR coil, and is characterized by a rising, then falling signal amplitude.[122] In typical NMR experiments, radiation damping is triggered by a small amount of transverse magnetization that is present in the sample following a non-ideal $\pi$ inversion pulse. The coupling of spin magnetization to the tuned detection coil of the NMR receiver can be described semi-classically by modified Bloch equations[118,123,124] as shown below.

$$\frac{dM_T}{dt} = -\frac{M_T}{T_2^*} - \frac{M_T M_z}{M_0 \tau_{rd}} \tag{2.2}$$

$$\frac{dM_Z}{dt} = -\frac{M_Z}{T_1} + \frac{M_T^2}{M_0 \tau_{rd}} \tag{2.3}$$

Here, $M_0$ is length of the initial magnetization vector, which is aligned with the direction of the magnetic field (z-direction), and $\tau_{rd}$ is the characteristic radiation damping time. $M_Z$ is the magnetization in the longitudinal direction, and $M_T = \sqrt{M_x^2 + M_y^2}$ is the magnitude of transverse magnetization. Since in the hyperpolarized experiment the magnetization at thermal equilibrium is much smaller than the initial magnetization, $M_{eq} \ll M_0$, it is neglected in Eq. (2.3). In order to compare the observed signal to a radiation damping

model, the magnetization $M_{\alpha,815ms}$ and $M_{\beta,815ms}$ of the hyperpolarized DMSO spin system with positive and negative spin temperature, respectively, was estimated by applying a $\pi/2$ pulse at t~815 ms after the start of sample injection. It was found that $M_{\beta,815ms}\big/M_{\alpha,815ms}$ = 0.4. Since the solid-state polarization levels (Fig. 2.1) for polarization to positive and negative spin temperature are similar, this observation implies that the initial magnetization $M_{\beta,0}$ decays more rapidly than the initial $M_{\alpha,0}$, presumably due to radiation damping. The characteristic radiation damping time constants of polarized samples were estimated by comparison to a measurement of radiation damping in a thermally polarized reference sample of DMSO. From fitting of the data obtained with the non-hyperpolarized reference sample (DMSO, filled circles in Fig. 2.3) the radiation damping rate ($R_{rd}$) and the latency interval ($t_0$) were determined to be ~23 $s^{-1}$ and 0.048 s, respectively.

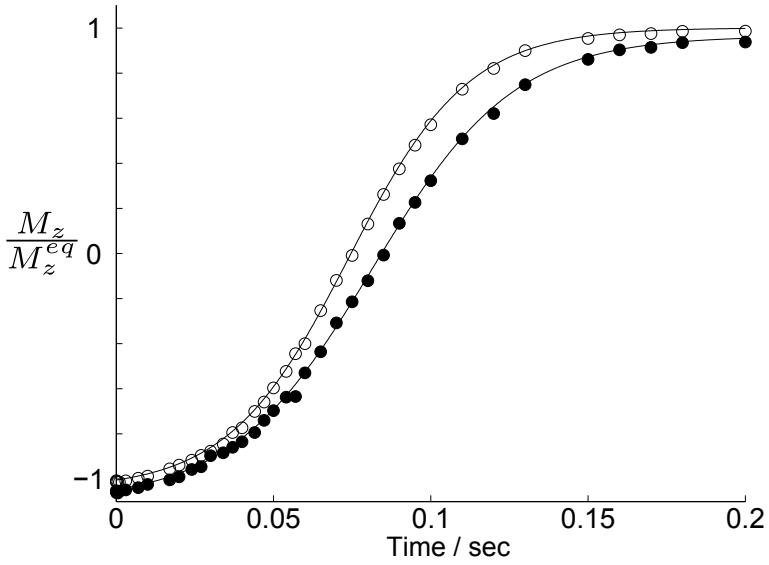


Figure 2.3: Radiation damping rates of 95% of DMSO/5 % $D_2O$ (filled circles) and 90% $H_2O$/10%$D_2O$ (hollow circles) are obtained by fitting experimental data to equation (2.1), giving $R_{rd}$ ≈22.7 and 26.3 $s^{-1}$ of $^1H$ nuclei of DMSO and $H_2O$.

The radiation damping rate can also be expressed as

$$R_{rd} = \frac{1}{\tau_{rd}} = \frac{\mu_0}{2}\eta Q\,|\gamma M_0| \tag{2.4}$$

where $\mu_0, \eta, Q, \gamma, M_0$ are the vacuum permeability, the filling factor and the quality factor of the probe, the gyromagnetic ratio, and the initial magnetization, respectively.[118] This equation can be used to infer the radiation damping rate for other samples, if the relative sample magnetizations are known. For DMSO, this ratio was estimated to be 12.5, by comparing the intensities obtained by applying a $\pi/2$ pulse to the thermally polarized reference sample and to a hyperpolarized sample, respectively. According to Eq.(2.1), the radiation damping rate of the hyperpolarized sample is therefore 275 $s^{-1}$. For water, the rate is of the same order in magnitude; however the exact number is more difficult to determine due to the possibility of the presence of residual non-polarized water in the dissolution solvent, which would affect the estimate of the absolute polarization level. Not surprisingly, the radiation damping is more significant in the hyperpolarized sample, even though the spin concentration is two orders of magnitude lower than in the thermally polarized reference sample.

### *2.3.4 Origin of Multiple Emissions*

Radiation damping appears to be the most reasonable explanation for the observed emission of signals. However, the Bloch equations with radiation damping (Eqs. 2.2 and 2.3) can describe only one single emission, where the observed signal rises, then falls. For illustration, a numerical solution of these equations using parameters close to the expected experimental conditions for a DMSO spin system is shown in Figs. 2.4a and b. This is in contrast to the present observation of multiple beats in the signal from samples that have been hyperpolarized to negative spin temperature, and subsequently injected into the NMR

spectrometer.

In similar experiments conducted with hyperpolarized xenon, the occurrence of multiple MASER emissions has been attributed to a chaotic behavior of the spin system resulting from interplay between radiation damping and the effect of distant dipolar field.[124] It was further apparent that in that case, individual emissions were independently triggered by spin noise. For the proton signal emission observed here, the situation appears to be different. The residual signal between the consecutive beats in our observation is always larger than the noise level (see Fig. 2.2). Therefore, in contrast to the observations with hyperpolarized xenon, in the present case it seems unlikely that emissions are triggered independently by noise originating from the spin system itself. However, the experimental conditions are different; in the present case the sample is injected into the NMR tube, and initial emissions appear already during the injection process. While, as stated above, the Bloch equations by themselves cannot describe the observed evolution of magnetization, it is noted that in experiments where hyperpolarization is used to generate a sustained MASER emission, for example for the purpose of magnetic field measurements, such transient oscillations are commonplace.[125] In those experiments, however, spins with negative spin temperature are continuously supplied to the system under observation.

Likewise, in the present case the signal oscillations observed can at least phenomenologically be explained by inclusion of an additional term in the Bloch equations in an attempt to describe a similar physical process:

$$\frac{dM_T}{dt} = -\frac{M_T}{T_2^*} - \frac{M_T M_z}{M_0 \tau_{rd}} \tag{2.5}$$

$$\frac{dM_Z}{dt} = -\frac{M_Z}{T_1} + \frac{M_T^2}{M_0 \tau_{rd}} - \alpha e^{-t/\tau_a} \tag{2.6}$$

In Eq. (2.6), the last term continuously supplies negative polarization from a reservoir

not coupled to the coil. The parameter $\alpha$ indicates the initial rate of addition of magnetization, and $\tau_a$ is a time constant describing an exponential reduction in the rate of added magnetization as time progresses. The addition of magnetization during the initial time (between time points A and B in Fig. 2.2) arises naturally due to the sample injection process, whereas the addition of magnetization at later times would be expected due to sample motions. Therefore, $\tau_a$ should be understood as an average parameter that includes all of these contributions. Specifically, $\tau_a$ would be dependent both on spin-relaxation in the volume outside of the active coil region, as well as on the rate of sample introduction.

Fig. 2.4 shows a numerical solution of Eqs. (2.2) and (2.3), which corresponds to the typical radiation damping process, as well as of the modified Eqs. (2.5) and (2.6). The

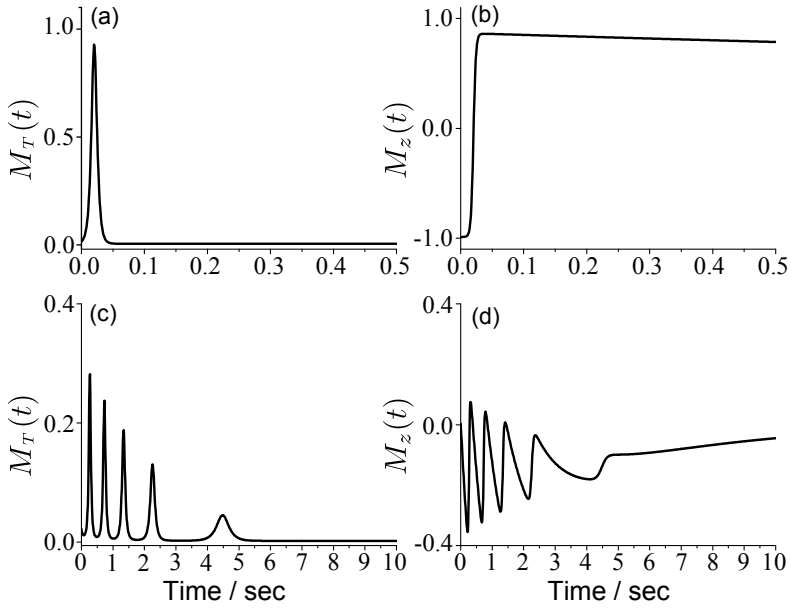


Figure 2.4: (a) and (b) transverse and longitudinal magnetization obtained from original Eqs. (2.2) and (2.3), (c) and (d) magnetization obtained from Eqs. (2.5) and (2.6), with inclusion of an additional term supplying negative polarization during the course of the experiment. Parameters were $T_2$=50 ms, $T_1$=5 s, $\tau_{rd}$=3.6 ms, $M_0$=1, $\alpha$=1, $\tau_a$=1 s. Boundary conditions were $M_T(0)$=0.01 and $M_Z(0)$=$-M_0$ for (a) and (b), and $M_Z(0)$=0.01 and $M_Z(0)$=0 for (c) and (d).

parameters used are indicated in the figure caption. In these parameters, the relaxation times were estimated from actual conditions for DMSO samples, the radiation damping time was taken from the results of Eq. (2.1) and Fig. 2.3, and a relative scale is used for the numerical value for the magnetization. Further, in contrast to the solutions to the regular Bloch equations with radiation damping, here, a boundary condition $M_Z(0)=0$ was used. This is due to the fact that initially, no sample is present in the NMR coil. The conditions of the simulation reasonably correspond to the actual hyperpolarized experiment. It can be seen from comparing Fig. 2.4 to the experimental results in Fig. 2.2 that the numerical solutions to Eqs. (2.5) and (2.6) qualitatively describe all of the features of the observed signal. Notably, there are multiple recurrences of signal of decaying amplitude, both with increased spacing, and of increased duration as time progresses. Furthermore, the longitudinal magnetization $M_Z$ is reduced after the last of the recurring signals.

The initial occurrence of signal, by the above equations, would depend on the amount of initially present transverse magnetization. Since this magnetization is presumably generated by random perturbations (noise) and is small, the observed signal occurrences may be expected to be irreproducible. Indeed, as stated above, the timing of signal occurrence varies from experiment to experiment. In the simulation, this is equivalent to a change in the relative magnitude of $M_Z(0)$. In agreement with the narrow spectral region affected by radiation damping, the emissions of the two hyperpolarized spins in Fig. 2.2, from water and DMSO, appear to be independent. Finally, it should be noted that, similar to observations by Giraudeau et al.[117] if the $^1$H nuclei are polarized to a positive spin temperature, and after injection and stabilization, the magnetization is inverted by a $\pi$ pulse followed by a pulsed field gradient, no signal recurrences were observed. Such a behavior would also be expected by the above model, as in this case only the spins that are within the NMR coil at the time of the pulse are inverted, and no additional negative polarization can be supplied. These conditions are therefore approximated by the solutions to Eqs. (2.2) and

(2.3), which are represented in Figs. 2.4a and b.

In order to further confirm that introduction of fresh magnetization due to sample movement is the likely cause for the multiple beats of signal emission, experiments were carried out under varying injection conditions (Fig. 2.5). A trend is apparent, where an increased pressure differential for sample injection increases the number of recurrences of signal. The larger pressure differential gives rise to a larger amount of sample motion. The same is true for a variation in the height of the injection tube over the bottom of the NMR sample. Here, a lower height gives rise to a larger amount of turbulence.[63,105] Both of these observations provide support for a model, where sample replenishment leads to multiple signal emissions through radiation damping.

While an equation that fully describes the turbulent and inhomogeneous sample injection process would likely be impossible to write, it is remarkable that Eqs. (2.5) and (2.6), despite their simplicity, can capture most of the observed features of the signal. This includes the occurrence of multiple signals, the observation that these signals persist for a longer time, but appear less frequently at later points in time, and that their amplitude is decreasing. The functional form of the term used for introduction of the magnetization during the experiment was chosen as an exponential, in analogy to a physical relaxation process. It is possible, however, that this term underestimates the introduction of new sample at the beginning of the injection, and overestimates the residual motions of the sample at later times.

The observations presented here substantiate the notion that the process of introduction of a hyperpolarized sample, coupled with radiation damping gives rise to a complicated and perhaps unexpected behavior of the spin system. On a more practical level, the observation of the signal occurrences due to radiation damping in a $^{1}$H spin system hyperpolarized to a negative spin temperature may be useful to judge the amount of residual turbulence after sample injection.

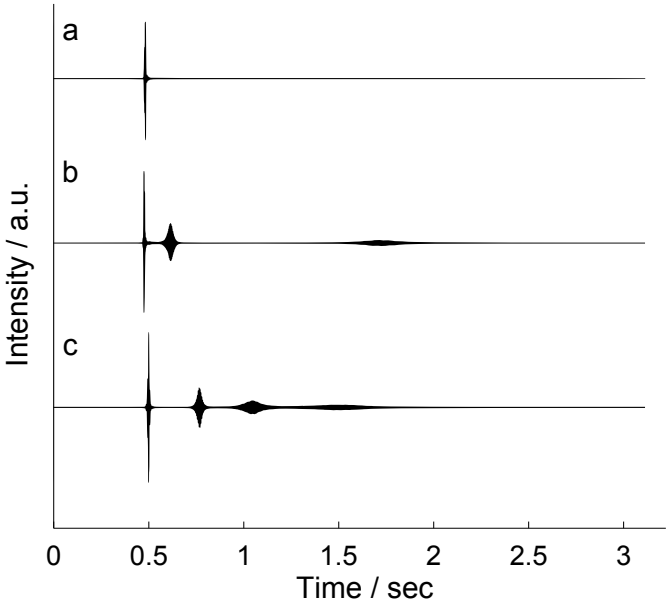


Figure 2.5: Emissions of $^{1}$H signal from mixtures of DMSO and $D_2O$ (1:1 v/v) hyperpolarized to negative spin temperature, under varying conditions for injection of the sample into the NMR spectrometer. (a) "slow" injection with a differential pressure of 770 kPa and a tube height of 54 mm (tube height is the distance between the tip of the injection tube and the bottom of the NMR tube), (b) injection as in a, but with a tube height of 36 mm and (c) "fast" injection with a pressure differential of 820 kPa and a tube height of 30 mm.

## 2.4 Conclusion

Currently available commercial instrumentation is poised to make hyperpolarization readily accessible for routine spectroscopy, and a variety of approaches for efficient hyperpolarization are being developed. For example, it has been reported that $^{13}$C polarization in some cases is more efficient at negative spin temperature.[126] In the case of $^{13}$C polarization with small samples, radiation damping may not be an issue due to the lower overall magnetization. However, for spectroscopy with protons, the most abundant NMR active nuclei, as well as perhaps for NMR with probes exhibiting a high Q-factor, such as cryogenically cooled probes, this effect can become dominant. In the data shown here, the

majority of the signal from a sample with negative spin-polarization is lost to radiation damping during sample injection, even before an NMR pulse can be applied. It is noted that in this case, the resonances affected by radiation damping stem from analytes at relatively low concentration (100 mM), as opposed to highly abundant solvent species that would normally be the only ones expected to be subject to radiation damping. Such effects therefore need to be taken into account when working with hyperpolarized samples, and merit further exploration. The observations presented here also serve to demonstrate that when pursuing new applications of hyperpolarized NMR, even well-known effects such as radiation damping may give rise to highly unexpected behavior of the spin system.

# 3. INVESTIGATION ON KINETICS OF PROTEIN FOLDING USING DNP-NMR*

## 3.1 Introduction

Protein folding occurs on a timescale that is not directly observable with most traditional nuclear magnetic resonance (NMR) spectroscopy methods.[127,128] The insights into this complex process that can potentially be gained from the high site-resolution of NMR has led to developments such as stopped-flow NMR,[129] incorporation of specific isotope labels,[130] and pulse sequences tailored for rapid data acquisition.[131] Hyperpolarization, the generation of a non-equilibrium spin state, shows significant promise to enhance the sensitivity and, by removing the need for signal averaging, dramatically decrease signal acquisition time.[105,132] For the study of protein folding, chemically induced dynamic nuclear polarization (CIDNP) has been used to hyperpolarize tryptophan residues that undergo a cyclic reaction with a photosensitizer.[133] A different technique, dynamic nuclear polarization (DNP),[41] hyperpolarizes nuclei throughout a molecule via an admixed stable free radical. Combined with solid state NMR, DNP provides unique information on protein structure.[50] Using dissolution DNP,[58] NMR in the liquid state would be sensitive to structural changes across the entire macromolecule during the folding process. Liquid-state NMR signals of a DNP hyperpolarized, denatured protein, the ribosomal protein L23,[134,135] have recently been observed.[65] Here, the re-folding of this hyperpolarized polypeptide is monitored following a pH jump (Figure 3.1).

*Reprinted in part from "Protein Folding Studied by Dissolution Dynamic Nuclear Polarization" by H. Y. Chen, M. Ragavan and C. Hilty, *Angew. Chem. Int. Ed.*, **2013**, Copyright 2013 WILEY-VCH Verlag GmbH & Co. KGaA, Weinheim

## 3.2 Experimental Section

Basically, the protein of interest is directly polarized, dissolved and injected into the 5 mm NMR tube pre-installed in the 400 MHz magnet. The protein re-folding is triggered via pH-jump and monitored by a series of rf excitation with small tip angle. The obtained set of $^{13}C$ spectra are individually decomposed into a linear combination of unfolded and folded reference spectra, giving protein kinetic data. The protein folding rate constant is obtained by fitting data to kinetic models and compared to folding rate constants measured by the fluorescence method.

### *3.2.1 DNP-NMR Spectroscopy*

Sample aliquots consisted of 10 uL of nominally 4 mM protein (Ribosomal protein L23) in 60%/40% (v/v) ethylene glycol/water, 6M urea, 15 mM OX63 radical (Oxford Instruments, Abingdon, U.K.), and 1 mM Gd-DTPA (SigmaAldrich, St. Louis, MO). Samples were hyperpolarized on $^{13}C$ for 4–6 h in a HyperSense DNP polarizer (Oxford Instruments) at T= 1.4 K, using microwaves of 60 mW power at 93.974 GHz. Samples were then dissolved in 10% (v/v) methanol (MeOH)/5 mM $KH_2PO_4$ in water, pH 3.1, heated to a vapor pressure of 10 bar. Dissolved samples were injected into a 400 MHz NMR spectrometer (Bruker Biospin, Billerica, MA) using customized rapid sample injector.[63] In the NMR spectrometer, samples were mixed at a ratio of 17:1 (v/v) with 25 uL of 810 mM 4-morpholineethanesulfonic acid (MES) buffer, pH 5.6–6.2. The NMR acquisition was triggered automatically. The temperature at the time of NMR measurement was 301 K. Solvent suppression was achieved in the experiment by using a 15 ms $\pi/2$ E-Burp selective pulse with pulse field gradient to de-phase the coherence. Multiple spectra were acquired by applying radio frequency pulses of variable flip angles followed by data acquisition in order to monitor the folding process.[81] During the data acquisition, $^{1}H$

and $^{2}$H decoupling were applied at field strengths of $\gamma B_1$=10.2 kHz and 0.7 kHz, respectively. Thermally polarized reference spectra of folded and unfolded L23 for use in the linear decomposition of each transient DNP-NMR spectrum (Figure 3.2) were measured using signal averaging on a 500 MHz NMR spectrometer with cryoprobe (Bruker). Data was processed (20 Hz line broadening, polynomial baseline correction) with TopSpin 3.0 (Bruker). $^{13}$C chemical shift in all spectra were calibrated indirectly to a standard of DSS at 0 ppm.

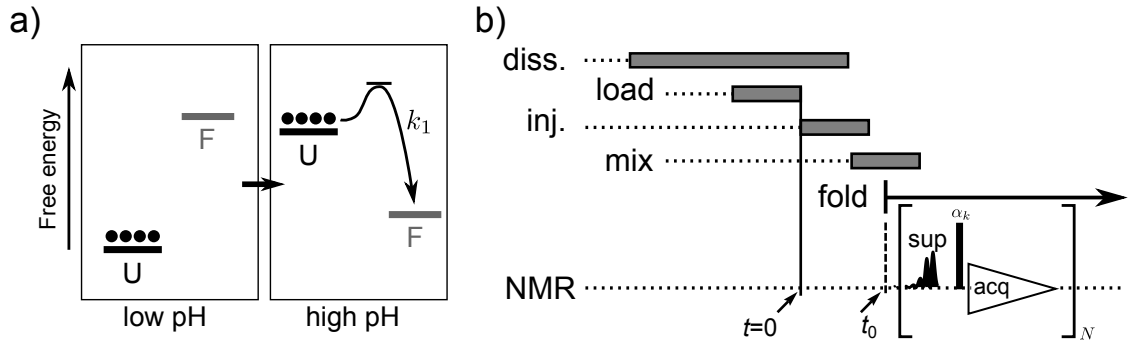


Figure 3.1: a) Representation of a pH jump experiment for re-folding of a protein (two-state folder shown). b) Experimental timeline, indicating dissolution ("diss."), loading into the injector ("load"), injection into the NMR instrument ("inj"), and mixing with refolding buffer. Acquisition of $^{13}$C spectra ("acq") is preceded by solvent suppression ("sup") and excitation with small flip angle of radio frequency pulses, $\alpha_k$ up to $N$ scans.

### *3.2.2 Stopped-Flow Fluorescence Measurements*

Intrinsic tryptophan fluorescence kinetics experiments were performed on a Quantamaster-80 fluorimeter (Photon Technology International, Birmingham, NJ) equipped with a stopped flow accessory (RX. 2000, Applied Photophysics, Surrey, UK). For fluorescence measurements, 1 uM of unlabeled L23 was dissolved in 10 mM phosphate buffer, pH 3.1, contain-

ing 10% MeOH. Protein folding was triggered by stopped flow mixing at a ratio of 1:1 (v/v) with a second buffer containing 90 mM urea, 200 mM ethylene glycol, 90 mM MES with 10% MeOH, and various pH values in the range from 5.5 to 6.3. Fluorescence was excited at a wavelength of 280 nm, and detected at 355 nm. Pulses from the photomultiplier were counted with a time resolution of 50 ms over a total time window of 5 s, using a PCIe-6259 data acquisition board and LabView (National Instruments, Austin, TX).

## 3.3 Results

### *3.3.1 pH-Jump Induced Protein Refolding Monitored by $^{13}C$ DNP-NMR*

Once the hyperpolarized L23 is transfered into the 400 MHz magnet, the pH-jump induced folding is then monitored over a period of seconds by acquisition of a series of NMR spectra using small flip-angle excitation (Figure 3.2a). The signal intensity in these spectra gradually decreases because of spin relaxation and the effect of excitation pulses. Relative signal changes, which can occur from folding as well as non-uniform spin relaxation, become visible in Figure 3.2b. Only the differences to the first and to the last scan in the time series are shown, after rescaling of each spectrum to equal intensity integrated over carbonyl and aliphatic regions. Relative intensity increases are observed in the chemical-shift region corresponding to the carbonyl chemical-shift range (170–185 ppm). The latter ”shoulders”, which are characteristic of the folded protein, are readily visible in re-normalized traces of the corresponding region (arrows in Figure 3.2c). Specifically, intensity from $\alpha$-helix and $\beta$-sheet secondary structure is broadly centered around 177.9 ppm and 174.5 ppm, respectively.[136]

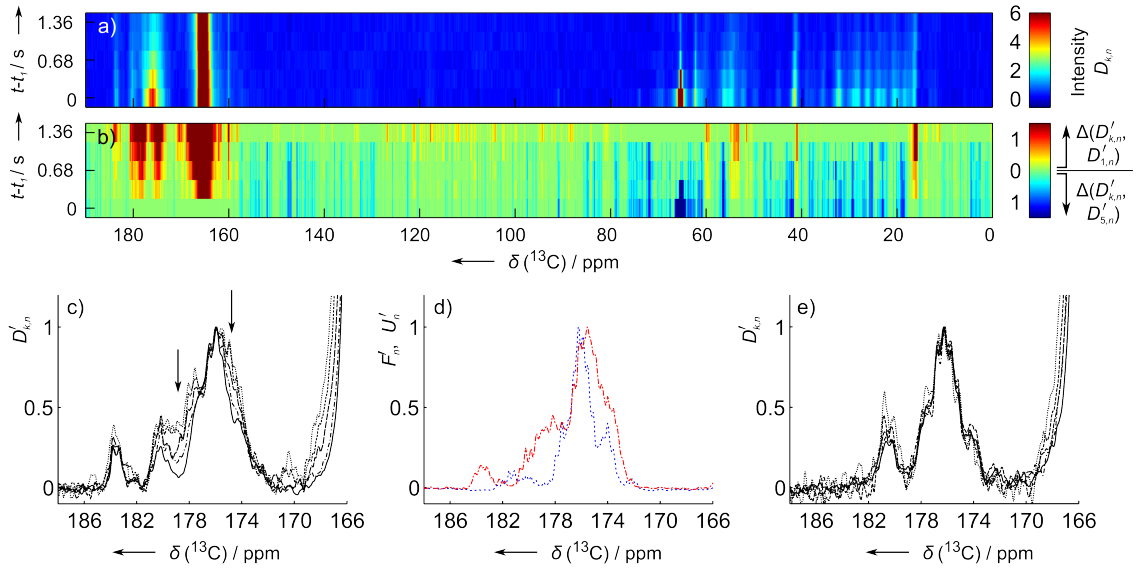


Figure 3.2: a) Intensity plot of a time series of 5 spectra from a single hyperpolarized sample of [u-$^{13}$C, 50%-$^{2}$H]-L23, after pH jump to initiate protein folding (40 $\mu$M L23, 100 mM ethylene glycol, 45 mM urea, 10% (v/v) MeOH, 5 mM $KH_2PO_4$ and 45 mM MES buffer, pH 5.8, $T$=301 K, $B$=9.4 T). $t_1$ is the time of the first scan. b) Composite plot showing in cyan–blue the difference compared to the last spectrum, and in yellow–red the difference compared to the first spectrum in the time series. Each spectrum ($D_{k,n}$) was re-scaled to unit maximum intensity near 176 ppm prior to taking the difference. The spectra after taking the difference are denoted by $D'_{k,n}$. c) Time evolution of carbonyl resonances (increasingly shorter dashes for later time; spectra are re-scaled to unit maximum intensity near 176 ppm). d) Reference spectra measured without hyperpolarization, of unfolded L23 (blue - - -; 40 $\mu$M L23, 100 mM ethylene glycol, 45 mM urea, 10% (v/v) MeOH, 5 mM $KH_2PO_4$, pH 3.1, 32,000 scans) and folded L23 (red –·–·; using sample from (a), 32,000 scans), cryoprobe at $B$=11.7 T. e) Series of spectra as in (c), but without pH jump.

### *3.3.2 Kinetic Analysis by Linear Decomposition of DNP-NMR Spectra into Fold/Unfolded References*

Quantitatively, the kinetic rate constant of folding can be extracted from analysis of the signal intensities in the DNP-NMR spectra. As L23 has been reported to follow a two-state folding process,[135] the populations of the folded and unfolded species at each time point are obtained by decomposing the individual scans into a linear combination

of reference spectra of folded and acid-denatured L23 (Figure 3.2d). The reconstructed spectra are in good agreement with the DNP-NMR spectra, except for deviations near 180 ppm and 183 ppm (the latter outside of the fitted region), which likely pertain to side-chain carbonyl chemical shifts (Figure 3.3a). Side-chain carbonyl chemical shifts exhibit a pH dependence in function of protonation state, and furthermore relative intensity differences can arise because the spin-lattice relaxation time ($T_1$) is longer in side chains than in the backbone. Figure 3.3b shows the time evolution of the signal fractions obtained from the decompositions. The first data point already contains a contribution from folded protein, as folding starts during the dead time of the experiment. Nevertheless, from a fit with kinetic model equations, folding and spin relaxation rates can be determined. The folding rate constants from several measurements with different final pH are shown in Figure 3.3c and are in excellent agreement with stopped flow fluorescence measurements. The model used here is based on a two-state folding mechanism, and assumes equal $T_1$ for folded and unfolded forms.

For decomposition, reference spectra and first scan of the DNP-NMR experiments were normalized to the integral of signal intensities between 170 and 181.7 ppm. Unfolded ($\tilde{\upsilon}_k$) and folded ($\tilde{\phi}_k$) fractions were determined by minimizing the root mean square difference between linear combinations of the reference spectra and individual scans from the DNP-NMR experiment. The apparent relaxation rate was found by fitting a single exponential to total signal intensity, then the folding rate was determined by fitting $\phi(t) = c \cdot e^{-r(t-t_0)}\left(1 - e^{-k_1(t-t_0)}\right)$ and $\upsilon(t) = c \cdot e^{-(k_1+r)(t-t_0)}$.

$$\sum_n U_n = \sum_n F_n = \sum_n D_{1,n} = 1 \tag{3.1}$$

The subsequent scans of DNP spectra were scaled to keep their relative intensity ratio

compared to the first scan. Integrals of the DNP spectra were calculated as

$$\tilde{\delta}_k = \sum_n D_{k,n}, \tag{3.2}$$

where the summation is over the data points corresponding to the backbone carbonyl region (170–181.7 ppm). Due to normalization, $\tilde{\delta}_1 = 1$. Subsequently, DNP spectra were decomposed into an unfolded part $\tilde{\upsilon}_k$ and a folded part $\tilde{\phi}_k$, by computing the following minimum independently for each $k$

$$\min_{\tilde{\upsilon}_k} \sum_n \left| \tilde{\upsilon}_k \cdot U_n + (\tilde{\delta}_k - \tilde{\upsilon}_k) \cdot F_n - D_{k,n} \right|^2 \tag{3.3}$$

with

$$\tilde{\phi}_k = \tilde{\delta}_k - \tilde{\upsilon}_k \tag{3.4}$$

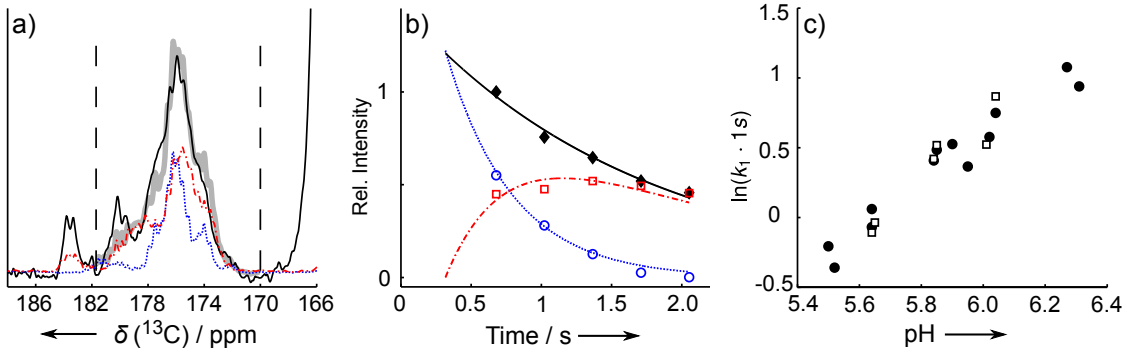


Figure 3.3: a) Decomposition of a representative spectrum (black —; 2nd scan of 5-scan time series) into a linear combination of unfolded (blue - - -) and folded (red –·–·) reference spectra. Reference spectra are drawn to scale according to their fractional contribution. The spectrum reconstituted by linear combination is shown as a thick gray line. Vertical dashed lines indicate fitting region. b) Time course of signal intentities. Shown are total signal (◆), and fractions of folded (red, □) and unfolded (blue, ○) forms obtained from linear decompositions. Fit results are $r = 0.59\ \mathrm{s}^{-1}$, $k_1 = 1.52\ \mathrm{s}^{-1}$ and $t_0 = 0.32$ s. c) pH dependence of folding rates for L23 from DNP measurements (□) and from fluorescence measurements (●) for validation.

The apparent relaxation rate $r$ was determined from a fit of the function $q \cdot e^{-rt}$ to $(t_k, \tilde{\delta}_k)$. The folding rate $k_1$ was then determined by

$$\min_{c,k_1,t_0} \sum_k \left|\tilde{\upsilon}_k - \upsilon(t_k)\right|^2 + \left|\tilde{\phi}_k - \phi(t_k)\right|^2 \tag{3.5}$$

with

$$\upsilon(t) = c \cdot e^{-(k_1+r)(t-t_0)} \tag{3.6}$$

and

$$\phi(t) = c \cdot e^{-r(t-t_0)} \left(1 - e^{-k_1(t-t_0)}\right). \tag{3.7}$$

Here, $\upsilon(t)$ and $\phi(t)$ are unfolded and folded protein fractions as a function of time. The derivation of these two equations, along with alternatives is given in the following section. The fit parameter $t_0$ designates the effective start of the folding reaction.

### *3.3.3 Monitoring Kinetics Using the Intrinsic Side-Chain Chromophore Probe*

Intrinsic fluorescence of the protein comes from the three aromatic amino acids, tryptophan, tryosine and phenylalanine. These fluorophores are often used as the probe to monitor the kinetic and structural change of proteins. The three residues have distinct absorption and emission wavelengths. In L23, there is one tryptophan residue which has the largest fluorescence quantum yield. Stopped-flow fluorescence experiment is performed to validate the kinetics derived from DNP-NMR method herein.

Fluorescence recovery upon protein folding is represented by a series of raw photomultiplier counts $\tilde{y}_k$ (Figure 3.4a). This data was fitted to a single exponential in order to extract the folding rate $k_1$ using eq. (3.8). Here, $y_0$ accounts for the fluorescence of the unfolded protein, as well as for folding during the dead time of the apparatus, and $a$ is the

maximum amplitude change.

$$y(t) = y_0 + a \cdot (1 - e^{-k_1 t}) \tag{3.8}$$

The top trace in Figure 3.4a shows a folding experiment, and the bottom trace a control measurement in the absence of pH jump. While the lack of change of fluorescence intensity in bottom trace in Figure 3.4a shows that there is no folding, the absolute values of fluorescence intensities should not be compared with the trace of the folding reaction, since the quantum yield of fluorescence at acidic pH is lower than at basic pH.[137] The pH dependence of the folding rate is shown in Figure 3.4b, indicating a strong pH dependence of the folding rate at slightly acidic pH. Data in each trace was renormalized according to $(\tilde{y}_k - y_0)/a$ to allow presentation on the same axis. The folding rates obtained from Figure 3.4b are included in 3.3c and compared with those measured by DNP-NMR.

It is noted that the tryptophan fluorescence experiments were performed using non-isotope enriched samples, whereas the DNP-NMR spectra used samples labeled with $^{13}C$ and $^{2}H$ at non-exchangeable positions. Significant kinetic isotope effects[138] in the NMR experiments are not expected, since amide and hydroxyl groups, which are typically involved in hydrogen bonding, underwent exchange with water protons. These positions were therefore not deuterated. A potential kinetic isotope effect in the folding was further investigated experimentally using [u-$^{13}C$, 50%-$^{2}H$]–L23 samples. This experiment yielded rate constants $k_1 = 3.53\ s^{-1}$ at pH 6.3; $k_1 = 1.72\ s^{-1}$ at pH 5.95 and $k_1 = 0.75\ s^{-1}$ at pH 5.5. These values compare favorably with the rate constants obtained from samples that are not isotopically labeled.

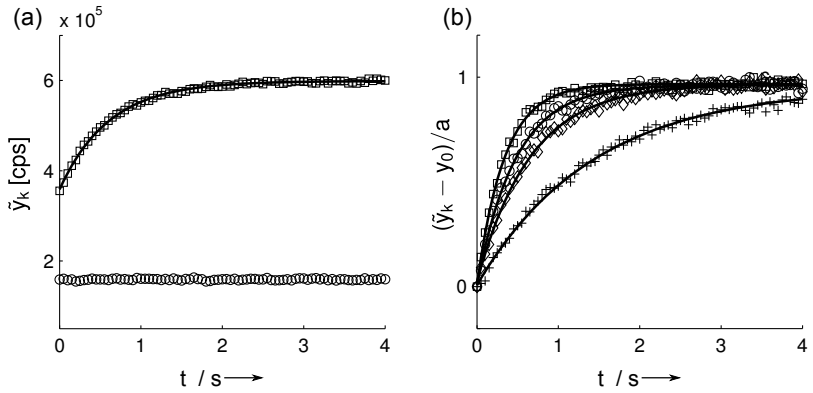


Figure 3.4: Stopped flow tryptophan fluorescence measurements of L23 under various conditions. L23 used in these experiments was denatured in 5 mM potassium phosphate, pH 3.1/10% MeOH mixture. a) Denatured L23 was mixed with 90 mM MES buffer containing 10% MeOH, 200 mM ethylene glycol and 90 mM urea for pH jump to pH=5.9 (□). The folding rate was $k_1 = 1.65\ s^{-1}$. The lower trace (○) shows a measurement without pH jump. b) pH jump experiments involving denatured L23 to various pH values, pH=6.3 (□), 6.0 (○), 5.7 (◇) and 5.5 (+), illustrating the pH dependence of the folding rate. The folding rates were $k_1 = 2.91\ s^{-1}$, $2.11\ s^{-1}$, $1.5\ s^{-1}$ and $0.7\ s^{-1}$, respectively.

## 3.4 Discussion

Several assumptions are applied in the kinetic analysis of DNP-NMR spectra. The validation of each assumption is discussed as follows. As a result, these scrutinies support the kinetic analysis of DNP-NMR data is reasonable and generally accepted.

### *3.4.1 Choice of the Reference Spectra in the Kinetic Analysis*

Since the pH change in the pH-jump experiment is instantaneous, the ”state” of unfolded L23 at the start of re-folding is ambiguous. In the Results section, acid-denatured unfolded spectrum (blue in Figure 3.5a) is used as the reference. An alternative urea-denatured reference spectrum (green in Figure 3.5a) has different chemical shifts especially in the range of side chains (182–185 ppm). In order to test the influence of side chain peak intensity on the decomposition, a reference spectrum of urea denatured protein

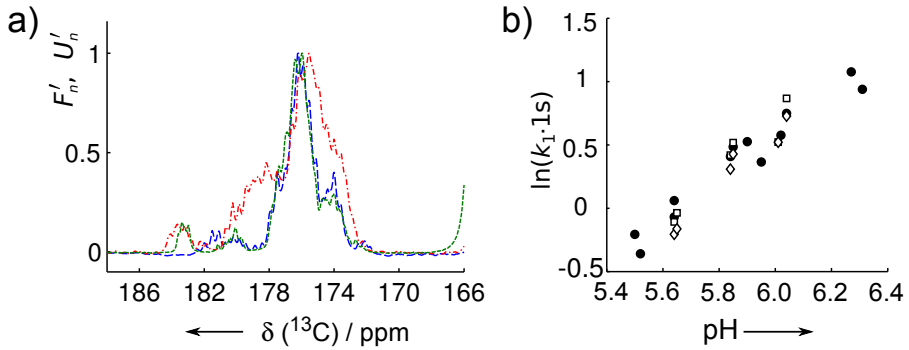


Figure 3.5: a) Reference spectra measured without hyperpolarization, of acid denatured L23 (blue – –; 40 $\mu$M L23, 100 mM ethylene glycol, 45 mM urea, 10% (v/v) MeOH, 5 mM $KH_2PO_4$, pH 3.1, 32,000 scans) and folded L23 (red –·–·; same sample as in DNP experiment, 32,000 scans). Green - - - indicates an alternative reference spectrum acquired from urea denatured L23 at pH=5.8 (0.4 mM L23, 100 mM ethylene glycol, 8 M urea, 10% (v/v) MeOH, 14,000 scans). All spectra were acquired using a cryoprobe at $B$=11.7 T. b) Comparison of folding rates obtained from fluorescence measurements (●) and from linear decomposition using the spectrum of acid denatured L23 (□) or urea denatured L23 (◇) as reference for the unfolded protein.

at pH 5.8 was further used. Results of folding kinetics were indistinguishable within experimental error (Figure 3.5b), suggesting that the effect of side chain carbonyl chemical shift variations is not significant.

### *3.4.2 Kinetic Models*

A protein with a two-state folding mechanism without the presence of folding intermediates such as L23, follows the reaction

$$U \underset{k_{-1}}{\overset{k_1}{\rightleftharpoons}} F \tag{3.9}$$

where $U$ and $F$ are the unfolded and folded species, respectively. The signals intensities

$$\overrightarrow{I}(t) = \begin{pmatrix} \upsilon(t) \\ \phi(t) \end{pmatrix} \tag{3.10}$$

observed in the NMR spectra are from the unfolded and folded form and are expressed as $\upsilon$ and $\phi$, respectively. Signal intensities follow the equation

$$\frac{d\overrightarrow{I}(t)}{dt} = (K + R) \cdot \overrightarrow{I}(t) \tag{3.11}$$

containing the kinetics and relaxation matrices

$$K = \begin{pmatrix} -k_1 & k_{-1} \\ k_1 & -k_{-1} \end{pmatrix} \tag{3.12}$$

and

$$R = \begin{pmatrix} -r_U & 0 \\ 0 & -r_F \end{pmatrix}. \tag{3.13}$$

$k_1$ and $k_{-1}$ are the first order rate constants for the folding and unfolding process, respectively. $r_U$ and $r_F$ are relaxation rates corresponding to the unfolded and folded forms of the protein.

In the dissolution DNP-NMR spectroscopy, observed signal intensities are in principle convolved with an input function due to sample mixing. Therefore, it is necessary to consider the process of sample injection and mixing. Under certain conditions, this could simply be accomplished by choosing appropriate boundary conditions when solving Equation (3.11). More generally, Equation (3.11) may be modified to include a term that

describes the addition of unfolded protein at the beginning of the experiment

$$\frac{d\overrightarrow{I}(t)}{dt} = (K + R) \cdot \overrightarrow{I}(t) + \overrightarrow{A}(t) \tag{3.14}$$

with

$$\overrightarrow{A}(t) = \begin{pmatrix} \alpha(t) \\ 0 \end{pmatrix} \tag{3.15}$$

In the simplest case, sample injection and mixing may be assumed to occur instantaneously at a time $t_0 > 0$. Then,

$$\alpha(t) = c \cdot Dirac(t - t_0) \tag{3.16}$$

where $Dirac(t)$ is the Dirac delta function, and $c$ is a constant.

The solution to equation (3.14) gives the time dependence of the observed signal intensities. For simplicity, it is assumed that the relaxation rates $r_U$ and $r_F$ are equal to a global relaxation rate $r$, and that $k_{-1} = 0$ (for a discussion of these assumptions, see below). Using the boundary conditions

$$\overrightarrow{I}(0) = \begin{pmatrix} 0 \\ 0 \end{pmatrix} \tag{3.17}$$

the solutions are

$$\upsilon(t) = \begin{cases} 0 & t < t_0 \\ c \cdot e^{-(k_1 + r)(t - t_0)} & t \geq t_0 \end{cases} \tag{3.18}$$

$$\phi(t) = \begin{cases} 0 & t < t_0 \\ c \cdot e^{-r(t - t_0)} \left(1 - e^{-k_1(t - t_0)}\right) & t \geq t_0 \end{cases} \tag{3.19}$$

with unknown parameters $c$, $r$, $k_1$ and $t_0$. From Equations (3.18) and (3.19), it can also

be seen that $k_1 > r$ should be fulfilled, as otherwise the decay of signal due to relaxation dominates. Using the above idealized model, the total signal simply follows the spin relaxation rate

$$\upsilon(t) + \phi(t) = \begin{cases} 0 & t < t_0 \\ c \cdot e^{-r(t-t_0)} & t \geq t_0 \end{cases} \tag{3.20}$$

Hence, it is possible to determine the relaxation rate directly from the experimental data, from a separate fit to the total signal intensity prior to decomposition of the spectra.

In reality, sample injection and mixing in the stopped-flow NMR experiment is a process that occurs over a certain amount of time. We have previously proposed to consider an exponentially subsiding addition of hyperpolarized sample.[77] In this case,

$$\alpha(t) = \begin{cases} 0 & t < t_0 \\ c \cdot (r + r_i) \cdot e^{-(r+r_i)(t-t_0)} & t \geq t_0 \end{cases} \tag{3.21}$$

The parameter $r_i$ describes the rate with which sample addition subsides. It appears together with $r$ in the exponent of Equation (3.21), since the injected sample is also subject to spin relaxation. The solutions become

$$\upsilon(t) = \begin{cases} 0 & t < t_0 \\ c \cdot \frac{r+r_i}{r_i-k_1} e^{-(k_1+r)(t-t_0)} \left[1 - e^{-(r_i-k_1)(t-t_0)}\right] & t \geq t_0 \end{cases} \tag{3.22}$$

$$\phi(t) = \begin{cases} 0 & t < t_0 \\ c \cdot \frac{r+r_i}{r_i-k_1} e^{-r(t-t_0)} \left[1 - e^{-k_1(t-t_0)} - \frac{k_1}{r_i}\left(1 - e^{-r_i(t-t_0)}\right)\right] & t \geq t_0 \end{cases} \tag{3.23}$$

with unknown parameters $c$, $r$, $k_1$, $t_0$ and $r_i$. It should be noted that in this model, sample addition never ends, but the rate of addition becomes very small for long times $t$. Under usual conditions, $r_i > r$. It can be seen that in the limit of rapid injection, $r_i \to \infty$,

Equations (3.22) and (3.23) converge to (3.18) and (3.19).

Finally, it may be interesting to consider a case, where sample is added for a finite time but at constant rate. Then,

$$\alpha(t) = \begin{cases} 0 & t < t_0 \\ \frac{c}{b} \cdot e^{-r(t-t_0)} & t_0 \leq t < t_0 + b \\ 0 & t \geq t_0 + b \end{cases} \tag{3.24}$$

The duration of the injection is given by $b$, and the exponential term in Equation (3.24) accounts for the spin relaxation of the injected sample. The solutions are

$$\upsilon(t) = \begin{cases} 0 & t < t_0 \\ c \cdot e^{-(k_1+r)(t-t_0)} \cdot \frac{e^{k_1(t-t_0)}-1}{bk_1} & t_0 \leq t < t_0 + b \\ c \cdot e^{-(k_1+r)(t-t_0)} \cdot \frac{e^{bk_1}-1}{bk_1} & t \geq t_0 + b \end{cases} \tag{3.25}$$

$$\phi(t) = \begin{cases} 0 & t < t_0 \\ c \cdot e^{-r(t-t_0)} \left( \frac{e^{-k_1(t-t_0)}-1}{bk_1} + \frac{t-t_0}{b} \right) & t_0 \leq t < t_0 + b \\ c \cdot e^{-r(t-t_0)} \left( 1 - \frac{e^{bk_1}-1}{bk_1} e^{-k_1(t-t_0)} \right) & t \geq t_0 + b \end{cases} \tag{3.26}$$

with unknown parameters $c$, $r$, $k_1$, $t_0$ and $b$. Likewise, for $b \to 0$, Equations (3.25) and (3.26) converge to (3.18) and (3.19).

The result from using the three different models for sample injection that are discussed above, is shown in Figure 3.6. In each panel, the function $\alpha(t)$, which describes the addition of magnetization, is plotted along with the experimental data and fitted curves $\upsilon(t)$ and $\phi(t)$. As long as the sample injection is set up to occur in a sufficiently short time, it is apparent that the main difference in the result between the three models occurs during the

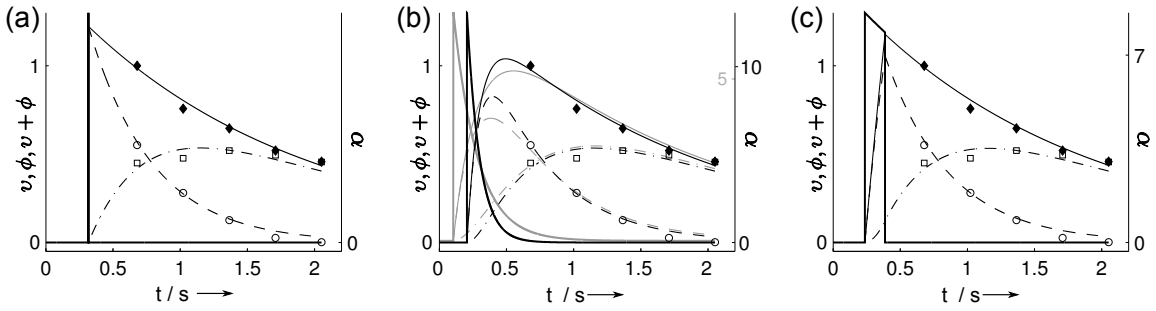


Figure 3.6: Comparison of results obtained by fitting the described models for stopped flow sample injection and folding kinetics to experimental data. a) Instantaneous injection, from Equations (3.16), (3.18) and (3.19). b) Exponentially subsiding injection, from Equations (3.21)–(3.23). Two traces are shown, for $r_i = 10\ s^{-1}$ (black lines) and $r_i = 5\ s^{-1}$ (gray lines). c) Constant rate injection, from Equations (3.24)–(3.26). On left ordinate: Signal from unfolded form, $\upsilon$ (○ and −−); signal from folded form, $\phi$ (□ and $\cdot-$); total signal, $\upsilon + \phi$ (◆ and —). The data points ○ and □ are from the spectral decomposition, whereas ◆ is from the integral of total signal intensity. On right ordinate:$\alpha$ (thick **—).**

mixing dead time. The results agree closely for the time points corresponding to measured values. From the fit parameters that are indicated in each figure, it is further apparent that, while model specific parameters differ, the folding rate $k_1$ obtained from each model is similar. The model specific parameters $r_i$ and $b$ in Figure 3.6b and c are less well defined due to the fitting problem being underdetermined. A change in these parameters can to some extent be compensated by a change in $t_0$. In Figure 3.6b, it can further be seen that if an injection rate $r_i \lesssim 5\ s^{-1}$ is assumed, the quality of the fit decreases. This observation appears to indicate that under the conditions chosen, injection was sufficiently rapid. The simplest model (Figure 3.6a) therefore appears adequate for interpretation of the data.

### *3.4.3 Signal Depletion Caused by RF Pulses*

The above equations describe the time course of longitudinal magnetization in the absence of radio frequency pulses. In reality, however, the measurement of each NMR transient entails the conversion of a part of longitudinal magnetization into transverse co-

Table 3.1: Parameters used in and derived from fit of experimental data to the three models for stopped flow sample injection. The fit equations or other source, from which each parameter was derived, is indicated in a separate column.

| Instantaneous injection | | Exponentially subsiding injection | | Constant rate injection | |
|---|---|---|---|---|---|
| Parameter | Source | Parameter | Source | Parameter | Source |
| $r = 0.59\ s^{-1}$ | eq. (3.20) | $r = 0.59\ s^{-1}$ | eq. (3.20) | $r = 0.59\ s^{-1}$ | eq. (3.20) |
| $k_1 = 1.52\ s^{-1}$ | eqs. (3.18), (3.19) | $k_1 = 1.51\ s^{-1}$, $k_1 = 1.53\ s^{-1}$ | eqs. (3.22), (3.23) | $k_1 = 1.49\ s^{-1}$ | eqs. (3.25), (3.26) |
| $t_0 = 0.32$ s | eqs. (3.18), (3.19) | $t_0 = 0.21$ s, $t_0 = 0.11$ s | eqs. (3.22), (3.23) | $t_0 = 0.24$ s | eqs. (3.25), (3.26) |
| $c = 1.22$ | eqs. (3.18), (3.19) | $c = 1.23$, $c = 1.25$ | eqs. (3.22), (3.23) | $c = 1.29$ | eqs. (3.25), (3.26) |
| | | $r_i = 10\ s^{-1}$, $r_i = 5\ s^{-1}$ | fixed [ref. 139] | $b = 0.15$ s | fixed [ref. 105] |

herence for observation. This magnetization is then no longer available for subsequent scans. Hence, the signal intensity obtained in the transient $j$ is equal to

$$I_j = I(t) \cdot \sin(\alpha_j) \prod_{k=1}^{j-1} \cos(\alpha_k) \tag{3.27}$$

where $\alpha_j$ is the flip angle of the radio frequency pulse used for excitation of scan $j$. However, if the flip angle is chosen as

$$\alpha_j = \arcsin \frac{1}{\sqrt{n - j + 1}} \tag{3.28}$$

the contributions of the product term in Equation (3.27) are equal in each scan, simply resulting in a constant scaling of intensity.[81] In this study, since rf excitation uses variable-flip-angle scheme, no further consideration of effect from rf pulses in the analysis of the data.

### *3.4.4 Influence from Variations of Relaxation Rates*

As a basis for quantification of the effect of spin relaxation on the observed spectra, $^{13}C$ $T_1$ was measured for the proteins used. At $B$=9.4 T, relaxation times of 1.6 s and 2.1 s were

obtained for the region containing predominantly backbone carbonyl chemical shifts (170–182) ppm in acid denatured and folded [U-$^{13}$C, 50%-$^{2}$H]-L23, respectively. The value for unfolded protein additionally agrees well with a value determined for unfolded L23 using DNP-NMR.[65] Additionally, differences in relaxation between backbone and side chain signals were assessed. In order to obtain high signal of side chain resonances, these measurements were carried out at $B$=11.4 T using a cryoprobe, and using urea denatured protein. Relaxation times of 1.5 s and 3.6 s were obtained for the predominantly backbone (170–179 ppm) and side chain (179–182 ppm) carbonyl regions, respectively.

Differences in relaxation rate of backbone and side chain carbonyl carbon spins explain the differences near 180 and 183 ppm between DNP-NMR and reconstituted spectra in Figure 3.3a. A higher relative carbonyl side chain intensity is present in the DNP-NMR experiment because of longer spin relaxation time. In addition, differences in relaxation rate between folded and unfolded protein can affect the calculation of folding rate from DNP-NMR data. In the simplest case, we assume that relaxation rates in the folded and unfolded forms of the protein are equal, *i.e.* $r_U = r_F = r$. If this assumption is true, data analysis is simplified, since $r$ can directly be found from the signal intensities in the same DNP-NMR data set that is used for determining the kinetic rates. Otherwise, it is necessary to measure relaxation rates in folded and unfolded protein either by DNP-NMR[65] or using a non-hyperpolarized inversion-recovery experiment.

Effects of differences in relaxation rates were determined by performing a simulation. Time dependent signals from unfolded and folded polypeptide ($\upsilon$ and $\phi$) were calculated using presumed individual relaxation rates and known folding rates, and subsequently analysed with the kinetic model that assumes instantaneous injection and equal relaxation rates (Equations 3.6 and 3.7). This analysis yields the apparent folding rate that would be obtained with the assumption that only one relaxation rate exists. The comparisons between apparent folding rates ($k_1^{app}$) and selected presumed folding rates ($k_1^{real}$) are shown

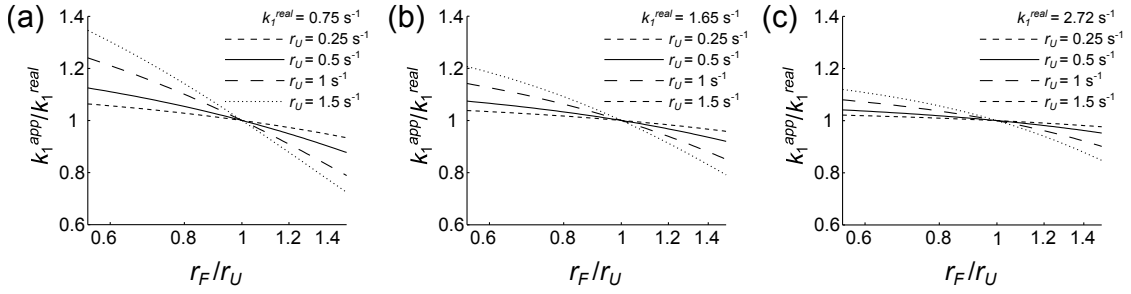


Figure 3.7: Simulation, shown in semi-log plot, illustrates the effect of differences in spin-lattice relaxation rates $r_F$ and $r_U$ of folded and unfolded protein on the kinetics analysis. $k_1^{app}$ is the apparent folding rate obtained from the model assuming a single relaxation rate $r$, whereas $k_1^{real}$ is the true folding rate. The curves were obtained by first calculating the time evolution of signal intensities from folded and unfolded protein using the parameters $r_F$, $r_U$ and $k_1^{real}$. For each $r_F/r_U$, $k_1^{app}$ was then detemined by fitting Equations (3.6) and (3.7) to the simulated data using the same procedure as for the analysis of the experimental data. The actual relaxation rate in unfolded L23 is $r_U = 0.6$ s$^{-1}$.

in the semi-log plot in Figure 3.7 for various ratios of the relaxation rates. It can be seen that, if $r_U$ is larger than $r_F$, the folding rates obtained when assuming a single relaxation rate will be overestimated, and vice versa. Under present experimental conditons, for $r_U$=0.63 s$^{-1}$ and $r_F/r_U$ = 0.76, the approximate error due to the assumption of a single relaxation rate is between 9% and 3% for $k_1$ between 0.75 s$^{-1}$ and 2.72 s$^{-1}$ (near the solid line in panels (a)–(c)). This error is similar to the experimental uncertainty (Figure 3.3c); therefore, the assumption of a single relaxation rate in the kinetic analysis appears valid in this case. It can also be noted that because of the magnetic field dependence of carbonyl chemical shift anisotropy relaxation, measurements at relatively low field, *e.g.* 9.4 T or 11.7 T, corresponding 400 MHz or 500 MHz $^1$H NMR frequency, may be preferred.

### *3.4.5 Influence of Phase Distortion Caused by Chemical Reaction*

It is known that in an NMR spectrum of the one-sided chemical reaction of first order, reactant resonances are broadened and product resonances show dispersive lineshape.[140] The line broadening of reactant resonances arises from the short lifetime of the reactant, while the dispersive feature originates from the delayed formation of product. Here, we have considered the potential influence of phase distortion on the kinetic analysis. This property of the signals is investigated by simulating lineshapes according to the Bloch-McConnell equations considering a one-sided chemical reaction.[140,141] The spectra at different time points for the largest folding rate observed in this work ($k_1$ = 2.38 $s^{-1}$) were simulated. Different changes in resonance frequency between denatured and folded forms ($\nu_U$ and $\nu_F$) upon reaction were considered. Figures S5a and b show the simulation at $\mid \nu_F - \nu_U \mid$= 50 Hz and $\mid \nu_F - \nu_U \mid$= 5 Hz, respectively. In both cases, the transverse relaxation rates were assumed to be 0.5 Hz and the ratio of initial magnetizations were calculated using Equations (3.6) and (3.7) with the fit results of $k_1$, $t_0$ and r. It is noted that the distortion of signals becomes prominent when $\mid \nu_F - \nu_U \mid$ is similar to the folding rate, such as in the spectrum at $t_0$ in Figure 3.8b. For large changes in frequency, for example, 100–300 Hz (corresponding to the difference between the center of the carbonyl chemical shift distribution and the growing shoulders), the distortion is nearly imperceptible. Once initial product has formed, the distortion is diminishing as demonstrated in time points $t_1$, $t_2$ and $t_3$ , where the reaction is completed to about 54%, 80% and 91%. Moreover, the effect of spectral distortion becomes less noticeable after applying exponential line broadening of 20 Hz, as was the case in the experimental measurements. Based on these evaluations, the influence of phase distortion in the kinetic analysis was not further considered.

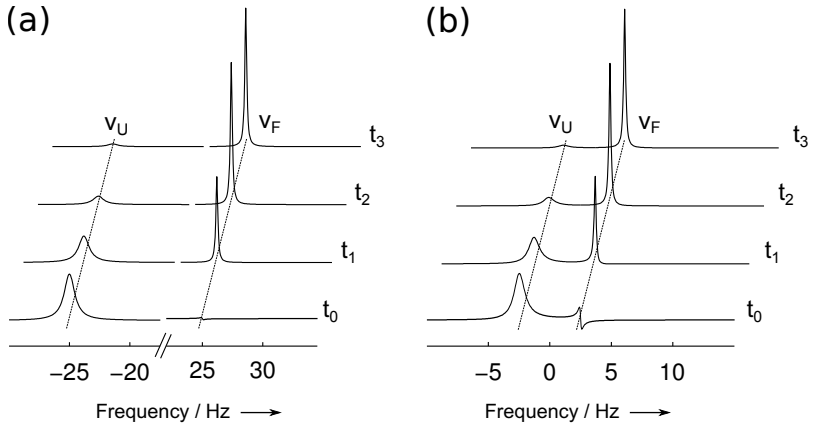


Figure 3.8: Simulation of lineshapes at different times in the two state protein folding process at the highest folding rate obtained in this study ($k_1 = 2.38\ s^{-1}$). Simulations assumed a difference of a) 50 Hz and b) 5 Hz between unfolded and folded resonances, $\nu_U$ and $\nu_F$. Simulations were carried out using the modified Bloch-McConnell equations considering non-equilibrium chemical reactions (*i.e.* no reverse reaction occurs). The spin-spin relaxation rate of each resonance was set as 0.5 Hz.

## 3.5 Conclusion

In proteins with more complicated folding pathway, this experiment could be useful for the identification of on-pathway intermediate states,[142] provided that their lifetime is at least on the order of ∼100 ms. Peaks of such intermediates can additionally be assigned by forward or backward correlation to the known chemical shifts in the folded or unfolded protein.[143] Additional site specific information can potentially be recovered using techniques aimed at reducing signal overlap, such as selective isotope enrichment[144] or multi dimensional spectroscopic techniques.[85] The length of the time interval accessible to the DNP-NMR method is governed by $T_1$ relaxation. Using deuteration, $^{13}C$ relaxation rates even in large polypeptides can be on the order of seconds.[145] In this time frame, the DNP-NMR measurement can provide a substantial amount of information on tertiary structure formation. Apart from the observation of global folding kinetics, DNP-NMR includes the capability to simultaneously resolve different sites on the macromolecule. These features

may enable the observation of differential kinetics in proteins that do not follow a two state folding mechanism, of contacts established during assembly of protein complexes, or even yield structural information on folding intermediates.

# 4. HYPERPOLARIZED HADAMARD SPECTROSCOPY USING FLOW NMR*

## 4.1 Introduction

Since the inception of dissolution dynamic nuclear polarization (D-DNP),[58] this technique for NMR sensitivity enhancement has gained attention in fields as diverse as biomedical imagaing[146] and high-resolution NMR spectroscopy.[80,147–149] D-DNP is by definition a technique for analysis of individual batches of sample that are first hyperpolarized as frozen aliquots, and subsequently injected into the NMR detector. Applications in high-resolution NMR spectroscopy that appear to most directly benefit from this mode of operation are those that require the rapid collection of data, for example for the study of a unidirectional chemical reactions.[105]

A key to these applications lies in the use of rapid sample injection technologies, such as the dissolution system incorporated in a purpose-built DNP-NMR spectrometer that has recently been described by Karabanov et al., which allows for sample injection into a standard or flow-NMR probe.[64] A sample injector developed in our own laboratory serves the same purpose when using two separate instruments for DNP polarization and NMR spectroscopy.[63]

The most direct implementation of NMR spectroscopy in combination with rapid sample injection consists of the acquisition of a single one-dimensional spectrum, or of a series of spectra acquired with small-flip angle excitation. One-dimensional spectroscopy however does not make full use of spin correlations that can be used to obtain structural information by NMR spectroscopy. Within the constraints of a single hyperpolarized sample, various approaches have been described to recover some of this information. These

*Reprinted from "Hyperpolarized Hadamard Spectroscopy Using Flow NMR" by H. Y. Chen and C. Hilty, *Anal. Chem.*, **2013**, Copyright 2013 American Chemical Society

include the acquisition of single-scan 2D spectra based on pulsed field gradients,[85] sequential acquisition of multiple scans for a 2D spectrum using small flip-angle excitation,[81] as well as indirect methods such as off-resonance decoupling.[83]

An alternative strategy for obtaining two-dimensional chemical shift correlations from dissolution DNP would be to physically split a hyperpolarized sample into multiple parts. If expected chemical shifts in one of the spectral dimensions are known, Hadamard spectroscopy presents an interesting alternative in obtaining correlation spectra even from a small number of scans.[150] In Hadamard spectroscopy, a series of one-dimensional scans is acquired. Each of these scans starts with the selective inversion of individual chemical shifts corresponding to a first spectral dimension using a Hadamard pattern, followed by the generation of coherences with coupled spins and acquisition of the NMR signal in the second spectral dimension. The correlation information is then reconstructed by applying a Hadamard transform, which consists of additions and subtractions of the originally acquired spectra.

The result of the Hadamard transform, if desired, can be represented in a form resembling a traditional 2D spectrum with peaks correlating two chemical shift axes. Hadamard spectroscopy requires fewer scans than traditional Fourier transform (FT)-2D spectroscopy, because no spectral information is acquired in the indirect dimension in regions, where no peaks are present. For this reason, Hadamard spectroscopy appears well suited for applications involving hyperpolarized NMR, where the number of samples is limited.

An advantage of Hadamard spectroscopy over pseudo-two dimensional (2D) methods such as off-resonance decoupling is the ability to resolve peaks even in the presence of chemical shift overlap. Additionally, each of the individual scans in a Hadamard spectrum contains signal intensity from each of the spins. As a result, the noise penalty in signal-to-noise ratio in the reconstructed spectrum is reduced compared to a series of one-dimensional spectra acquired with single selective excitations.

In the present work, we introduce an apparatus that allows for precise control of injection into a flow cell, which provides for the acquisition of a limited number of scans from different portions of a single hyperpolarized sample. We then demonstrate two-dimensional Hadamard spectroscopy using this technique. Finally, we discuss a strategy using the maximum entropy method for accounting for signal decay due to spin relaxation and concentration differences in the reconstruction of Hadamard spectra from multiple portions of the hyperpolarized sample.

## 4.2 Methods

### *4.2.1 Sample Injector for Flow NMR*

In order to overcome the limitation of using a sample from D-DNP for only a single scan, a setup for sample injection from a DNP polarizer into a flow-NMR probe was implemented (Figure 4.1a). The central part of the injector device consisted of two 10-port valves V1 and V2 (MODEL, VICI-Valco, Houston, TX) that were simultaneously switched between a loading position (solid black lines) and an injection position (dashed black lines). The port V1,1 was connected to a HyperSense DNP polarizer (Oxford Instruments, Tubney Woods, UK). Ports V1,5 and V2,2 were connected to a flow cell inserted into a 400 MHz NMR spectrometer (Bruker Biospin, Billerica, MA).

In the loading position, a stream of sample from the DNP polarizer fills a sample loop of 1.5 mL. An optical detector sensed the arrival of liquid at the end of the loop, defining the time point $t_0$ for injection (Figure 4.1b). A drive fluid was continuously pumped from the V2,3 input through the two valves, using a LC-20AD high performance liquid chromatography (HPLC) system (Shimadzu, Kyoto, Japan) set to a flow rate of 16 mL/min (pressure of 800–900 psi). In the loading position, the fluid simply flowed into a waste container (or could be re-circulated if desired). In the injection position, it flowed through

the sample loop, tubing T1 and 160 $\mu$L flow cell, thereby delivering the sample for NMR analysis. Ports marked with "×" in the figure were blocked. The initial delay of sample delivery was 3–4 s, which was adjusted for the first part of the sample to arrive in the flow cell. The tubing sizes (0.03" ID, ~ 10 feet long) were chosen so that the entire sample was transferred past the valve V2 into the tubing T1 during this initial time. The time interval ($\Delta t$) between each NMR scan included 700 ms acquisition time ($t_{acq}$), 1 s stabilization ($t_{stab}$) and 700 ms injection phase ($t_{fwd}$) for the subsequent scan. The flow of sample through the cell was stopped by switching the valves to the loading position. This procedure was repeated until the entire sample was transferred from the tubing T1 to the flow cell, for a typical yield of 8 scans.

Supporting electronics of the sample injecotr were identical to those already described,[63] allowing for the computer control of the injection valves using a LabView program (National Instruments, Austin, TX). The NMR spectrometer was equipped with a TXI probe that had been engineered for flow-through capability in conjunction with a modified CryoFIT flow conversion system (Bruker Biospin). Sample was delivered to the flow cell from the bottom of the magnet, and exited towards the top.

### *4.2.2 DNP Polarization*

The sample for DNP polarization consisted of 10 $\mu$L of self-glass-forming solvent, 1-butanol, containing 15 mM of the free radical $\alpha$,$\gamma$-bisdiphenylene-$\beta$-phenylallyl (BDPA; Sigma-Aldrich, St. Louis, MO). The frozen sample aliquot was hyperpolarized on $^{13}$C nuclei in the HyperSense DNP polarizer. The polarization temperature was 1.4 K, and microwave irradition was applied for 3–4 h at a power of 60 mW and a frequency of 93.965 GHz. After dissolution with $H_2O$ heated to ~180 °C, the sample was injected using the sample injector described above. The driving fluid, pure water, was pumped by

HPLC system at pressure ~800–900 psi.

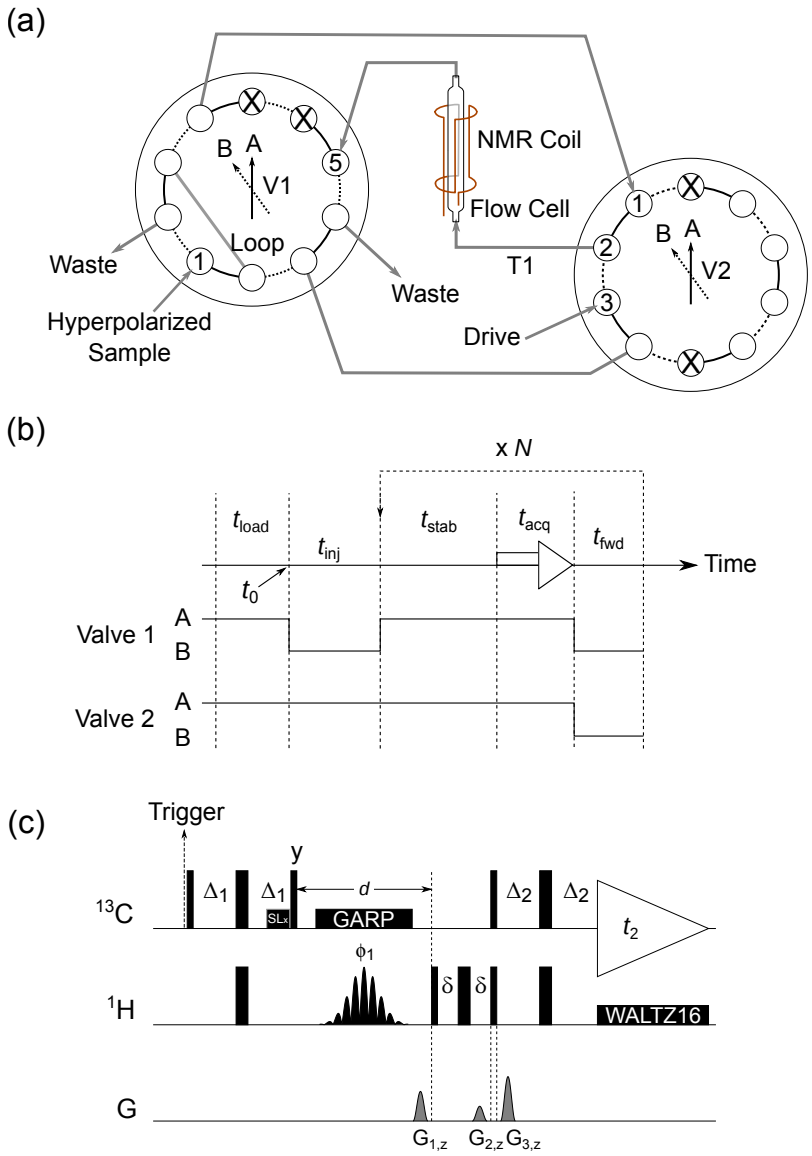


Figure 4.1: a) Diagram of the sample injection device for D-DNP spectroscopy using a flow NMR probe. b) Timing diagram of sample injection. c) NMR pulse sequence for [$^{13}$C,$^1$H]-HSQC Hadamard experiment utilizing $^{13}$C hyperpolarization.

### *4.2.3 NMR Spectroscopy*

Heteronuclear single quantum correlation spectroscopy between $^{13}$C and $^{1}$H was performed using Hadamard encoding. A pulse sequence modified from Steinbeck et al.[151] was used, with the high- and low frequency channels (proton and carbon) exchanged (Figure 4.1c). The start of the NMR experiment was triggered by a transistor-transistor logic (TTL) signal from the sample injection device. The first radio-frequency (RF) pulse was applied on $^{13}$C nuclei. Coherence was then transferred to $^{1}$H using a delay $\Delta_1$=1.19 ms optimized for CH, CH2 and CH3 groups. During the transfer, a trim pulse, SLx, was applied to maintain the desired coherence. A band-selective inversion pulse[152] (dual Gaussian shape, pulse length of 50.79 ms, maximum pulse amplitude $\gamma B_1$=47.8 Hz) was applied simultaneously to two $^{1}$H resonances. The resonances to be inverted were chosen differently in each scan, according to a Hadamard matrix. A purging gradient, $G_{1,z}$ of 35.5 G/cm was used to eliminate the effects from imperfect pulses. Finally, coherence was transferred back to $^{13}$C using a delay $\Delta_2$=1.19 ms, and the signal was detected. Hard radio-frequency pulses of flip angles $\pi/2$ (narrow black bars) and $\pi$ (wide black bars) were applied with strength $\gamma B_1$=18.2 kHz on $^{13}$C, and $\gamma B_1$=29.8 kHz on $^{1}$H. During the selective inversion pulse, GARP decoupling was applied on $^{13}$C using $\gamma B_1$=2.5 kHz, and WALTZ-16 decoupling with $\gamma B_1$=2.5 kHz was applied on $^{1}$H during acquisition.[153] The single quantum coherence transfer pathway was selected using pulsed field gradients $G_{2,z}$= 14.2 G/cm and $G_{3,z}$= 56.8 G/cm, of 1 ms length which were applied as close as possible in time to minimize signal losses due to the sample movement. The delay $\delta$=1.2 ms was included to allow application of $G_{2,z}$. The dual Gaussian shaped pulse and the integer number of GARP decoupling cycles are both centered in the delay ($d$).

### 4.2.4 Hadamard Reconstruction Using Entropy Maximization

The correlation information from a Hadamard spectrum can be retrieved by a Hadamard transform.[150] In the ideal case, such as in non-hyperpolarized Hadamard spectroscopy, the relative intensities of each scan are identical. The set of $n$ reconstructed spectra, each containing $m$ data points, $\mathbf{R} \in \mathbb{R}^{m\times n}$, are then obtained via decoding of the originally acquired $n$ Hadamard spectra $\mathbf{D} \in \mathbb{R}^{m\times n}$ with a Hadamard transformation defined by the same Hadamard matrix $\mathbf{H}_n$ as was used for encoding (Equation 4.1).

$$\mathbf{R} = \mathbf{D} \cdot \mathbf{H}_n \tag{4.1}$$

However, in the dissolution DNP-NMR measurement, the signal intensity varies among scans if unequal concentrations of analyte are present, and because of the $T_1$ relaxation. Under the assumption that the effect of relaxation is uniform for all spins, this variation can be accounted for by introducing a scaling factor for each spectrum, to be applied before Hadamard decoding. The scaling factors can be written as a row vector $\mathbf{C} \in \mathbb{R}^{1\times n}$. With $\mathbf{1} \in \mathbb{R}^{m\times 1}$ a column vector with all elements equal to one, the Hadamard transform can be replaced by

$$\mathbf{R} = (\mathbf{D} \circ \mathbf{1C}) \cdot \mathbf{H}_n \tag{4.2}$$

In Equation (4.2), $\circ$ denotes the element-wise multiplication of two matrices (incidentally also known as Hadamard product).

Since the assumption of equal spin relaxation for all of the peaks is necessarily an approximation, it is not always trivial to find optimal scaling factors $\mathbf{C}$. Here, we use a method based on maximum entropy for this purpose.[154] The entropy function is chosen as

$$S = -\sum_{i=1..m} h_i \ln h_i, \tag{4.3}$$

where

$$h_i = \sum_{j=1..n} P_{ij} \tag{4.4}$$

with

$$P_{ij} = \frac{\left|R_{ij}\right|}{\sum\limits_{k=1..m} \left|R_{kj}\right|}. \tag{4.5}$$

The matrix **P** in Equation (4.5) contains an absolute value representation of the result spectra **R**. The sum in the denominator is over all data points in the spectrum $j$, such that the columns of **P** are normalized. In Equation (4.4), a sum of each of the corresponding data points in the normalized absolute value spectra of **P** is calculated in order to obtain a measure of total intensity at each position in the spectra. The optimized scaling factors contained in **R** are then found by maximizing the entropy function $S$ in Equation (4.3).

The numerical optimization as described above was performed using Matlab (MathWorks, Natick, MA). The Nelder-Mead simplex algorithm (fminsearch) was used to find the minimum of the objective function, negative S (Equation 4.3). The unconstrained variables in the optimization were the scaling factors of each scan, except for that of the first scan, which was fixed as a reference.

## 4.3 Results and Discussion

In order to determine the amount of sample present in the flow cell at different times, a solution of red dye was injected in an otherwise similar manner as in the DNP experiment. Images taken at the time points that would correspond to each scan show that under these conditions, sample is available in the flow cell for a total of approximately 8 scans (Figure 4.2a). The gradual increase in dye concentration near $n = 1$, and gradual decrease near $n = 9$ is due to laminar flow in the inlet tubing. A similar result is obtained by acquiring a series of $^{13}$C spectra from a sample of hyperpolarizewd 1-butanol (Figure 4.2b). Each

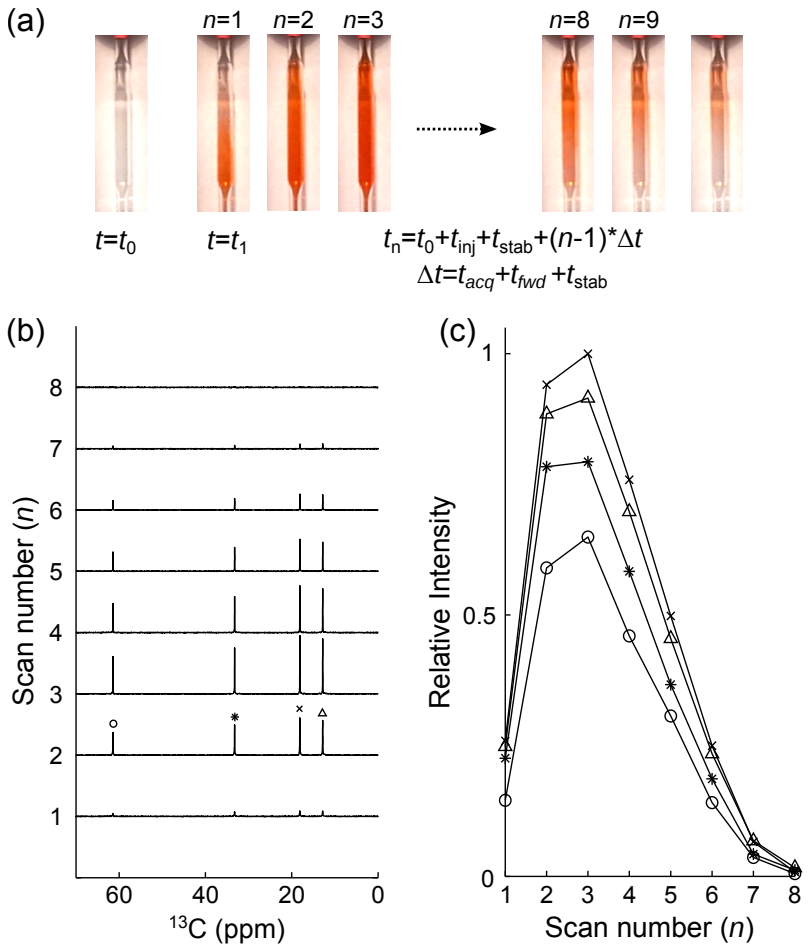


Figure 4.2: a) Images showing the injection of a red dye into the flow cell. Time points correspond to those indicated in Figure 4.1. b) Series of spectra acquired in the flow cell from a hyperpolarized sample of 1-butanol. The time of each scan corresponds approximately to the images in (a). c) Plot of total intensity from the spectra shown in (b).

of these spectra were acquired using a single $\pi/2$ pulse followed by acquisition with $^{1}$H decoupling, and therefore show the amount of signal available in each scan. The line width was approximately 1.5 Hz, which appears sufficient to resolve most peaks in typical spectra of small molecules. A plot of total signal intensity from these spectra is shown in Figure 4.2c. Similar to Figure 4.2a, it can be seen that the signal intensity at first increases, and then decreases for later scans. This effect is however due to the combination

of the concentration variation and spin-lattice relaxation. The four scans showing highest signal intensity are scans 2–5, and the time points corresponding to these were used in the following for the Hadamard experiment. In order to obatin a [$^{13}$C,$^{1}$H] heteronuclear correlation experiment, the $^{1}$H resonances of butanol were phase encoded according to a 4×4 Hadamard matrix (Figure 4.3a and b). No inversions were implemented in the first scan. In the following scans, two out of four peaks were selectively inverted by a dual-frequency $\pi$ pulse. For example, in the second scan, peaks a and d were encoded. Figure 4.3c shows the resulting $^{13}$C spectra. By comparing signal from the second scan in a separate DNP measurement to signal of a reference sample acquired by a single $\pi/2$ pulse, the average enhancement of ~500 is obtained.

Different options were explored for reconstructing the $^{13}$C–$^{1}$H correlation information from the Hadamard encoded data set. Because of variations in the signal intensity among different scans, which are due to both a concentration gradient and spin relaxation, a direct Hadamard transform would yield unsatisfactory results. The simplest method of reconstruction for such D-DNP Hadamard data sets appeared to be to scale each of the spectra with a global scaling factor before the Hadamard transform. As opposed to deducing these scaling factors based on characteristics of the instrument or the molecule under study, we propose the use an entropy maximization for this purpose. An advantage of this method is that reconstruction requires no information external to the data set.

The optimization applied to the data from Figure 4.3 resulted in an entropy function $S$ that rapidly converged to a maximum value of 34.7 (Figure 4.4a). The set of spectra in Figures 4.4b, d and e represent the reconstruction before, during and after optimization. It can be seen that the smaller residual peaks, which are due to unequal signal amplitude in the original spectra, are attenuated over the course of the optimization. The final spectra in Figure 4.4e contain to a large margin only the four expected correlation peaks. These peaks correspond to the cross-peaks that would be expected in a typical two-dimensional

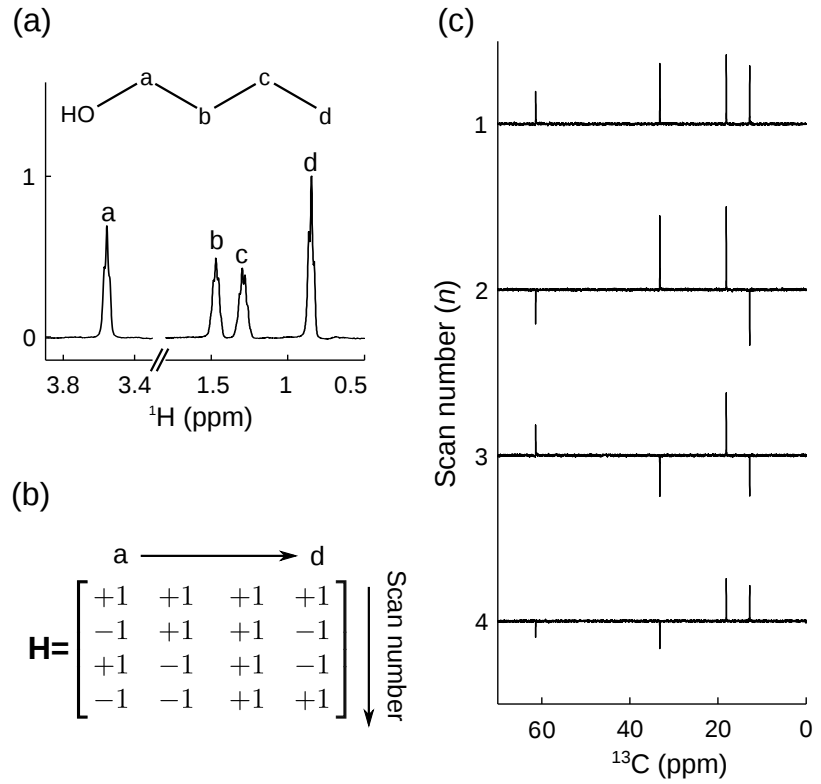


Figure 4.3: a) Non-hyperpolarized proton spectrum of 1-butanol, showing the chemical shifts a–d of selective inversion for the Hadamard experiment. b) Hadamard matrix used for $^1$H encoding. The numbers +/-1 indicate no inversion, or selective inversion using a pulse with $\pi$ flip angle, respectively. c) Hyperpolarized carbon spectra of the Hadamard encoded data set.

[$^{13}$C,$^1$H]-HSQC experiment. As an alternative representation, strips in pseudo-2D spectra in Figure 4.4c and f illustrated the decoded spectra without and with using MaxEnt rescaling, showing residual peaks became less noticeable.

To further validate the method of finding the global scaling parameters by maximizing entropy as described above, reconstructions of simulated data sets containing increased variations in spin-lattice relaxation time $T_1$, increased noise, signal overlap were performed (supporting information in appendix A). In the case of equal relaxation time constants (Figure A.1), the proposed decoding procedure allows obtaining four distinct peaks

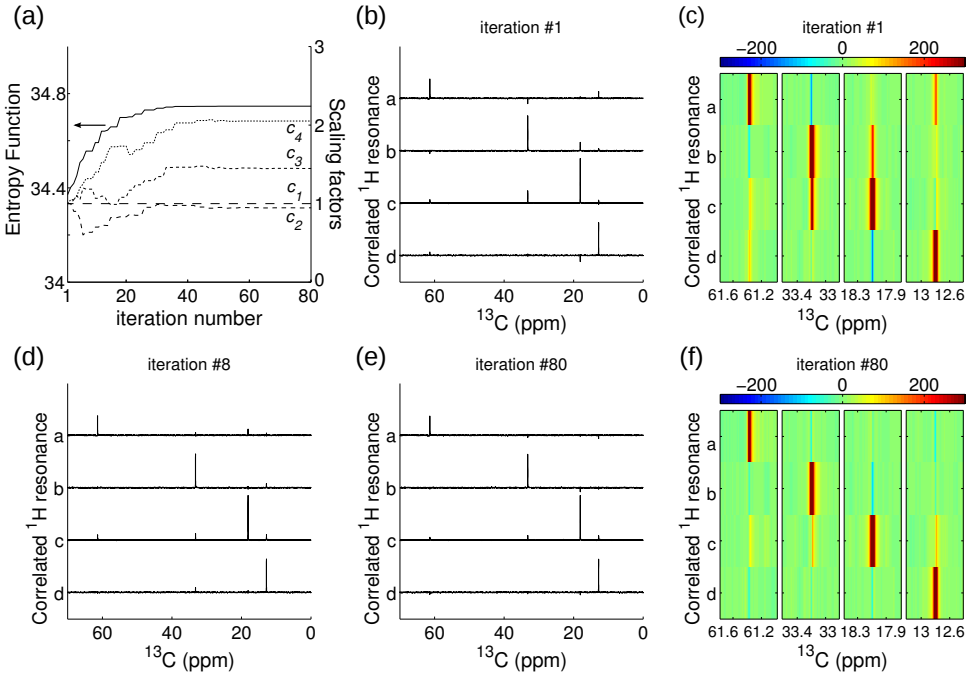


Figure 4.4: a) Evolution of the value of the entropy function $S$ from Equation 4.3 (solid line), and the four independent scaling factors $c_1..c_4$ (dashed lines, from longest to shortest) during the optimization procedure for the data set shown in Figure 4.3c. The parameter $c_1 = 1$ was fixed, and starting conditions were $c_1 = c_2 = c_3 = c_4$. b) Reconstructed spectra using identical scaling factors (iteration #1). c) Strips of the pseudo-2D spectrum of (b). d) Reconstructed spectra from an early iteration, #8. e) Final reconstructed spectra (iteration #80). f) Strips of the pseudo-2D spectrum of (e).

without knowing relaxation parameters in advance, as shown in Figures A.1e and f. A source of error, which is unavoidable when using global scaling parameters for each spectrum, is due to differences in spin-lattice relaxation rates. The test molecule used in the experiments, 1-butanol, contains the following $^{13}$C spin-relaxation times: 3.6 s, 4.1 s, 5.1 s and 5.6 s (higher to lower chemical shift). In simulations with different $T_1$ constants, as indicated in Figure A.2b, some residual peaks in the third and fourth scans of Figure A.2e appear, but under these conditions are sufficiently small to not significantly impact the determination of chemical shift correlations. In the case of larger $T_1$ variation, the four correlated resonances are still distinguishable, even through the number and amplitude of

residual peaks increases and peaks become more perceptible (Figures A.3e and f). Close inspection of the results from simulation (Figures A.3e and f) and experiment (Figure 4.4e and f) reveals that the entropy maximization procedure appears to find a "compromise" in the scaling factors, such that some of the residual peaks have positive intensity (*i.e.* too small subtraction), whereas others have negative intensity (*i.e.* too large subtraction).

It is further interesting to examine the capability of this analysis method in other limiting cases. Figure A.4a shows the simulated Hadamard spectra with the average SNR~10 in the first scan (5 times lower than the other simulations). As shown in Figure A.4e and f, the proposed method is still applicable. It is noted that the inherent advantage of improved SNR from multiplexed detection in the Hadamard spectroscopy is not necessarily fully realized in hyperpolarized Hadamard spectroscopy, since poor SNR is the last scan can deteriorate the SNR of Hadamard decoded spectra because of the larger scaling factor for the final scan. Finally, the situation of spectral overlap (peaks c and d in the inset of Figure A.5a) is investigated, showing that the overlapped resonances are well separated after decoding (Figure A.5e and f). Furthermore, in the case of complete overlapping such as two chemically-inequivalent protons bonded on the same carbon nucleus, the MaxEnt optimization still gives clearly resolved peaks. In all scenarios, signal variation due to $T_1$ relaxation is considered, while the experimentally observed concentration gradients are not taken into account. This appears reasonable, because only $T_1$ relaxation will give rise to non-uniform intensity variations across each spectrum, and hence imperfect cancellation. From the simulations performed, it appears that Hadamard reconstruction with MaxEnt rescaling is robust towards the parameters tested in minimizing imperfect cancellation in hyperpolarized Hadamard spectroscopy. On the basis of these results, it appears possible that similar optimization methods can also be applied other types of pulse sequences that require the addition of subtraction of signals from multiple scans, such as those involving phase cycles.

On a technical level, the setup with sample loop and injection valves serves the purpose of decoupling the stream of fluid from the DNP polarizer. This is important because typical D-DNP instruments drive the dissolution process by gas flow.[58] However, gas bubbles need to be avoided in the flow cell for reasons of magnetic field homogeneity. The inlet and outlet tubing should also be free of compressible gas, in order to allow rapid stopping of the fluid flow for each scan. Decoupling of the dissolution and injection processes also gives the necessary flexibility in timing the different parts of the injection process to allow the acquisition of sequential scans, each from a fresh sample. This allows for full utilization of the entire hyperpolarized sample, without otherwise possible losses of $> 50\%$. Splitting the sample into multiple parts also gives increased flexibility in the type of pulse sequences that can be applied, when compared to multi-scan acquisitions on the same sample using multiple small-flip angle excitations.[81] In small flip-angle schemes, the nucleus carrying the hyperpolarization can only be subjected to $\pi$ pulses after an initial excitation pulse in each scan; otherwise the polarized spin state would be lost. The Hadamard correlation experiment described here, which contains two $\pi/2$ pulses on the $^{13}$C channel, for example could not have been readily applied using small flip-angle excitation.

The multi-part acquisition could therefore be amenable to various other NMR experiments. By adjusting the volume ratio of flow cell and sample, as well as the acquisition times, it would be possible to use more than four scans, depending on the need of a specific experiment. A similar effect could also be achieved by replacing the fluid in the flow cell only partially for each scan, if necessary in combination with the use of pulsed field gradients to remove previously generated coherences.

Several aspects can be investigated to improve enhancement obtained here. For example, using mixed glassy matrix such as butanol/diethyl ether or different paramagnetic polarizing agents and adding lanthanide ions could potentially increase the solid-state polarization. Further improvements in the signal-to-noise ratio obtainable could possibly be

realized by increasing the flow-rate of the drive fluid. Given the same tubing size, the required pressure would however also increase. Spin-relaxation may further be counteracted by storing the hyperpolarized sample in a higher magnetic field than present in the inlet tubing (T1 in Figure 4.1a), prior to acquisition of the NMR scans. Finally, it may be possible to reduce dispersion of the sample during flow by using a drive fluid that is not miscible with the sample solution, provided that droplet formation can be effectively prevented.

## 4.4 Conclusions

In summary, a technique has been described for circumventing the single-scan limitation of traditional D-DNP experiments through multiple data acquisitions using an NMR flow cell. The technique was applied to the measurement of a four-scan Hadamard [$^{13}$C,$^{1}$H] correlation spectrum of the test molecule 1-butanol. Compared to some of the other indirect methods for obtaining chemical shift correlations from hyperpolarized samples, such as off-resonance decoupling, an advantage of Hadamard spectroscopy is the ability to resolve signal overlap. However, Hadamard spectroscopy requires subtractive reconstruction of the result spectra. This procedure is not trivial in the presence of variations in concentration and spin-lattice relaxation present in the D-DNP experiment. However, a method based on entropy maximization was found for this purpose, which requires only the measured data set as input and is robust against the effects of noise and signal overlap. Finally, additional strategies for further improvement of the method in terms of signal-to-noise ratio and obtainable number of scans have been discussed. Apart from the Hadamard [$^{13}$C,$^{1}$H]-HSQC experiment described, we anticipate that other types of correlation spectra can be quite flexibly implemented using similar multi-part acquisition schemes, enhancing the utility of the D-DNP technique for small-molecule characterization.

# 5. FLOW-INJECTION FOR DISSOLUTION DYNAMIC NUCLEAR POLARIZATION

## 5.1 Introduction

Hyperpolarization, the use of non-equilibrium spin populations for enhancement of NMR signals often by orders of magnitude, has led to advances across the field of NMR.[11,155] In liquid state NMR, dissolution dynamic nuclear polarization (D-DNP) is interesting for its versatility in polarizing various molecules and nuclei. A distinguishing feature of D-DNP is the separation of a location for hyperpolarization from a location for performing the NMR experiment. This paradigm enables the use of optimal conditions for DNP, such as a low temperature on the order of Kelvins. High polarization levels, on the order of tens of percent in the liquid state have been achieved using D-DNP.[156,157] Consequently, D-DNP shows promise for new applications in magnetic resonance imaging (MRI), as well as in high-resolution NMR.[59] Hyperpolarized compounds in the liquid state yield a sufficient signal-to-noise ratio to detect changes that occur during the progress of chemical reactions. In-vivo, direct detection of metabolic products enables the spatially localized detection of diseases.[90,158] In-vitro, catalyzed or spontaneous chemical reactions are detectable in real-time.[105,106]

The spatial separation of the polarization process from NMR measurement in D-DNP however also introduces an additional complexity to the experiment, as the hyperpolarized sample needs to be dissolved and injected into the NMR instrument. A limiting factor in all dissolution DNP experiments is the transfer time between the dissolution of the hyperpolarized aliquot, and the NMR measurement. During this time, spin relaxation in the liquid state is active, which leads to signal loss. Requirements for D-DNP experiments applied to high-resolution NMR are different than those for the magnetic resonance imaging

(MRI) technique. For MRI, samples are injected into living organisms. By nature of this experiment, the injection is comparably slow, but requires extensive precautions such as removing free radicals used for polarization, sterilizing the resulting solution, or ensuring a gas-free stream of liquid.[159–162] Compounds with long spin-lattice relaxation time are used, which prevents substantial loss of spin polarization prior to the compound reaching the site of interest. For the in-vitro study of chemical reactions or other processes using high-resolution NMR, a larger set of molecules is of potential interest. Many of these molecules exhibit shorter spin relaxation times on the order of seconds. Sample injector devices have been described to transfer the sample to the NMR instrument in as little as a second, using pressurized gases.[70,163] These devices also allow for mixing of the hyperpolarized sample with other components pre-loaded in the NMR tube.[71,164] For most applications satisfactory linewidths can be obtained despite the need for pre-shimming of the magnetic field using a different sample. One observation is that sample transfer using a gas pressure driven injector gives rise to residual fluid motion that may persist during the NMR measurement. Such sample motions have been characterized by Granwehr et al.,[70] where, as a quantitative measure, an apparent diffusion coefficient arising from residual fluid motion was determined from measurement of the attenuation of spin echo signals under application of pulsed field gradients. The effect of such fluid motions is of significance for NMR experiments making use of PFGs in general. These experiments include many modern techniques, such as those for acquiring multi-dimensional spectra.[165,166] In D-DNP, PFGs are the preferred choice for coherence selection, since spectra should be acquired in a single scan. Applications include the selection of specific signals in one-dimensional spectra, such as of spin systems containing specific $J$-coupled nuclei, as well as ultrafast multidimensional techniques.[167,168] In certain cases, it is possible to place PGFs in close temporal proximity, such that residual motion has only a small impact. However, with extensive use of PFGs throughout the pulse sequence, signal attenuation

or the occurrence of unexpected signals (”artifacts”) due to residual sample motion may become significant. It appears, therefore, interesting to explore options for high-speed sample injection that minimize sample motion during the NMR pulse sequence.

An alternative to the turbulent injection of a DNP polarized sample into an NMR tube is the injection into a flow cell. Flow cells have been used in conjunction with a magnet containing two homogeneous regions of magnetic field, where DNP polarization and NMR measurement can occur in close spatial proximity.[169] In the classical D-DNP setup composed of two separate magnets, a flow cell can also be used. In our own previous work, a flow cell enabled the separation of gases prior to a liquid driven injection.[170] Here, we describe an implementation of flow-NMR for D-DNP, where a rapid injection is driven by a high-pressure liquid, resulting in an injection time of less than 1.6 s. We then characterize the performance of this system, in particular in view of residual sample motions at the time of NMR measurement.

## 5.2 Methods

### *5.2.1 Sample Injector Setup*

For liquid driven sample injection, two high-pressure, high flow-rate pumps (1000D and 500D, Teledyne Isco, Lincoln, NE) are coupled to two high-pressure 2-position valves (8 port, 1/8” tubing diameter, 1.3 mm bore, titanium body, max. pressure 34.5 MPa, PN: DL8UWTI, VICI Valco Instruments, Houston, TX). In the configuration shown (Fig. 5.1a), the syringe pumps have two different volumes, but depending on injection volume and pressure requirements could be replaced with two identical pumps of either type. The 2-position valves are designated V1 and V2 in the figure. A Y-mixer is included, such that a non-hyperpolarized solution can be admixed to the DNP polarized sample before entering the flow cell for the NMR measurement. The routing of tubing between the DNP

polarizer, valves and the NMR instrument is designed for automatically loading HP sample from the polarizer into loop L1, and manually loading the second sample component into loop L2 using a syringe. All tubing in the setup is made of rigid materials in order to avoid expansion. An increase in the internal volume would lead to a pressure build-up rate insufficient for rapid sample injection. Copper tubing (1/8" OD) connects the syringe pumps to the 2-position valves. The two sample loops are made of polyether ether ketone (PEEK) tubing (1/8" OD, both with a total internal volume of 1 mL). The remaining connections, designated with p1-p5 in the figure, use PEEK tubing of different sizes (see figure caption for details). The high pressure that can be generated by the syringe pumps causes potential hazards. To partially alleviate such hazards, relief valves (SS-4R3A, Swagelok) are located at the exit of the pump heads.

LabView software (National Instruments, Austin, TX) controls the two syringe pumps and the switching of the 2-position valves. The timing of each event in the sample injection process is illustrated in Figure 5.1b. The two pumps are set to run before the start of dissolution of the HP samples. The pumps and outlet tubing are thus pre-pressurized to a constant pressure for rapid and consistent injections. In the setup as described, the syringe pump with larger volume (ISCO 1000D) is started earlier because of its slower build-up of pressure. Initially, V1 and V2 are in the loading position (L), indicated by a solid bar. Once the sample loop (L1) has been filled with HP sample, an optical detector (OPB350, OPTEK Technology, Carrollton, TX) triggers the switching of V1 to the injection position (I), indicated by a hollow bar. The fluid in pump 1 then drives the HP sample out of the loop and towards the mixer. V2 is switched to the I position slightly before the HP sample arrives in the mixer to prevent part of the HP sample from flowing into the tube p2. The fluid containing hyperpolarized sample then becomes mixed with the second sample component, which was pre-loaded in loop L2. As soon as the mixture arrives in the flow cell located inside of the NMR coil, the two pumps are stopped and both valves

are switched back to the L position. In this configuration, since port 2 in V2 is blocked, a closed loop comprising the flow cell and Y-mixer is formed, which causes the fluid flow to subside. After a short time delay ($t_{stab}$), the NMR measurement is performed. The start of $t_{mix}$ is the timing, when injection of the non-hyperpolarized reagent commences. For experiments that do not require admixing of a non-hyperpolarized sample component, the pump 2 and V2 can be simply disabled in the Labview program. The parameter, $t_{mix}$ is then discarded and total injection time is determined by $t_{inj}$.

The gas driven sample injector, which was used for comparison, is detailed in our previous publication.[163] Briefly, as shown in the Figure 5.1c, before the dissolution the NMR tube is pressurized by $N_2$ gas with pressure of $P_b$. For this purpose, the three-way valve (T) is set to connect ports b and c, and the on/off valve S1 is closed and S2 is opened. Once the sample loop L3 (TEFLON, 0.0625" ID, 1mL) is filled, the valve V3 (C22-6180, VICI Valco Instruments) is switched and $N_2$ gas with a pressure $P_f$ is supplied to drive the HP sample against a backward pressure ($P_b$) into an NMR tube. To rapidly equilibrate the pressure in the NMR tube, the ports f and c in T are connected at the end of injection. A delay $t_{stab}$ is allowed for sample motions to subside, and the NMR acquisition follows. Adjustable parameters include the forward/backward pressures ($P_f/P_b$) and distance ($h$) between the tip of the injection tube t1 and the bottom of NMR tube. For experiments that require mixing, other reagents with volume 25-50 $\mu$L can be pre-loaded in the NMR tube.

### *5.2.2 Experiments*

To determine the optimal transfer time for sample delivery with the liquid driven injector, a 10 $\mu$L aliquot containing dimethylsulfoxide (DMSO) and $D_2O$ (v/v 1:1) with 15 mM TEMPOL radicals (Sigma Aldrich, St. Louis, MO) was hyperpolarized in a Hyper-

Sense DNP polarizer (Oxford Instruments, Abingdon, UK) using microwaves of 94.001 GHz and 100 mW, at 1.4 K for 30 minutes. The frozen sample was dissolved using 4 mL

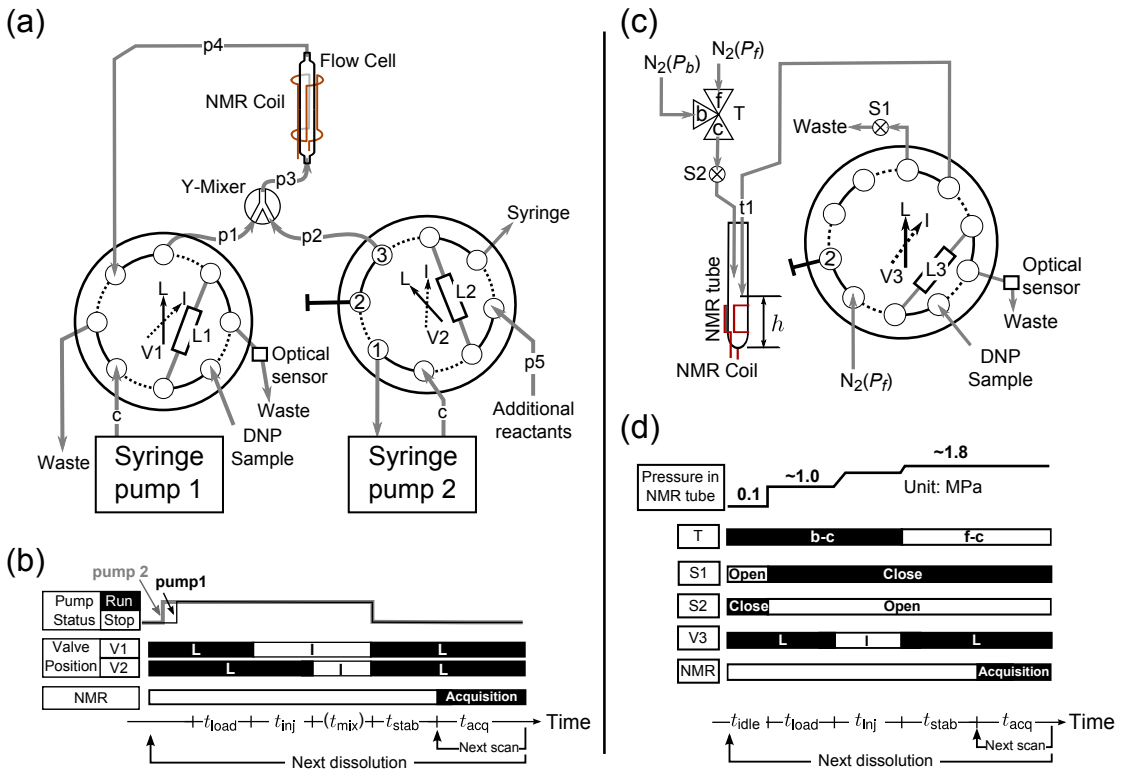


Figure 5.1: a) Schematic of the liquid driven injector for D-DNP. Hyperpolarized sample and non-hyperpolarized reactants can be loaded into two sample loops. During injection, they flow through the mixer, and then into a flow cell in the magnet for NMR detection. Different type and size of tubing is designated by c (copper, 1/8' OD), p1 & p2 (PEEK, 0.02" ID; 0.062" OD), p3 (PEEK, 0.02" ID; 0.03" OD), p4 & p5 (PEEK, 0.03" ID; 0.062" OD). b) Status of syringe pumps and 2-position valves during the experiment. A solid bar indicates that the valve is in the loading position (L), and a hollow bar indicates the injection position (I). Time intervals ($t_{\text{load}}$, $t_{\text{inj}}$, $t_{\text{mix}}$, $t_{\text{stab}}$) are on the order of hundred ms (see Methods section). c) Schematic of the gas driven injector. The $N_2$ gas with pressure of $P_f$ is used to inject the HP sample against a backward pressure of $P_b$ into a 5 mm NMR tube for NMR measurements. d) The status of valves at each timing in the injector, including two on/off valves (S1 & S2), a 2-position valve (V3) and a three-way valve (T). The functions of these valves and injection parameters (pressure, time intervals and etc.) are described in the text.

of $H_2O$, which had been heated until a pressure of 10 bar was reached. The sample was then injected into a 400 MHz NMR spectrometer fitted with a triple-resonance TXI probe (Bruker Biospin, Billerica, MA). Injection was performed as described in the previous section, using $H_2O$ as the driving fluid. For this experiment, no mixing was required, and only a single pump (pump 2) was used. An array of $^1$H NMR spectra was acquired by a series of radio-frequency (RF) pulses with a small tip angle of $\pi/20$. The NMR experiment, including pulses and data acquisition, was triggered at the beginning of $t_{inj}$. This point in time, which is earlier than for a typical experiment, was chosen in order to be able to observe the arrival of hyperpolarized sample that continuously flowed into the NMR coil. In this experiment, the time delay between excitation pulses should be long enough so that the fresh HP sample can refill the flow cell and the effect from the previous part of sample is minimized.

Once the arrival time was determined from the aforementioned experiment, the line shapes obtainable using this sample injector were characterized. A hyperpolarized aliquot containing 1.5 M benzamidine, 15 mM OX63 radicals (Oxford Instruments, Abingdon, UK) and mixture of ethylene glycol/$H_2O$ (v/v 6:4) was dissolved with phosphate buffer (50 mM, pH=7), and injected with $H_2O$ as described above, without admixing a non-hyperpolarized counterpart. After the stabilization time $t_{stab}$=200 ms, a total of 16 $^{13}$C NMR spectra were acquired by a set of RF pulses with a tip angle of $\pi/6$ and acquisition time of 648 ms. Data was Fourier transformed using TOPSPIN 3 software (Bruker), without apodization. The line shapes from each scan were fitted with a Lorentzian function.

Residual motions that persist in the sample after a rapid injection were assessed by monitoring a stimulated gradient echo train as function of time.[70,171] For this purpose, a 10 $\mu$L aliquot of d6-DMSO/$H_2O$ mixture (v/v 1:1) with 15 mM TEMPOL radicals was hyperpolarized on $^1$H nuclei. 1 mL of 200 mM citrate buffer was manually loaded in L2 in lieu of a second sample. HP samples were injected either by the liquid driven or the

gas driven injectors. In the measurements using the liquid driven injector, pumps 1 and 2 were set to nominal flow rates of 130 and 150 mL/min, respectively. Timing parameters were $t_{\text{inj}}$ = 330 ms and $t_{\text{mix}}$ = 420 ms. These parameters were determined by monitoring the color change of a pH indicator upon pH-jump (see supporting information), to ensure that mixing occurred. Under these conditions, the mixing ratio of HP sample and the non-HP sample was 4:1 v/v, which was determined by NMR. In the experiments using the gas driven injector, parameters were $P_f$ = 1.79 MPa, $P_b$ = 1.03 MPa, $t_{\text{inj}}$ = 310 ms and $h$ = 33 mm, respectively. A sample of 30 $\mu$L of 200 mM citrate buffer was pre-loaded in the NMR tube to mimic an experiment involving mixing. In both cases, the $t_{\text{load}}$ was measured to be ~930 ms.

The pulse sequence for generating and measuring the gradient echoes is shown in Figure B.2 (see supporting information). A superposition of magnetization helices was first created by applying N encoding pulses (with a tip angle $\alpha = \pi/113$ and pulse length=1 $\mu$s, N=16), separated by $\delta = 700\,\mu$s over a continuous field gradient $G_z$ = 0.035 T/m. After a delay $\delta_d$ = 10 $\mu$s, a $\pi/2$ pulse stored a projection of the resulting spatial encoding of magnetization longitudinally, in order to minimize signal loss through $T_2$ relaxation during the subsequent diffusion time. The time interval between each encoding pulse and the $\pi/2$ storage pulse ($t_n$) was $n\delta + \delta_d$. The index $n$ equals to N for the first pulse and 1 for the last pulse. Crushing gradients ($G_x$=0.056 T/m, $G_y$=0.053 T/m) were applied to remove the unwanted transverse magnetization. After a diffusion time $\tau_1$ = 5 ms, a series of RF pulses (with a flip angle $\beta = \pi/14$ and pulse length=2 $\mu$s) was used to create stimulated gradient echoes. The same readout procedure was repeated, until signal-to-noise ratio of echo signals deteriorated due to $T_1$ relaxation and the effect of pulses. The time points for each subsequent readout were $\tau_m = \tau_1 + (m-1)\cdot\Delta\tau$, for $m = 1, 2, .., M$, with $\Delta\tau$=50 ms and $M$ = 32. The $G_z$ gradient described above was enabled throughout the entire experiment.

The obtained stimulated echo signals were represented as a $M \times N$ matrix. The signal

intensity depends on the spatial displacement of the sample during the diffusion time, the effect of applying RF pulses, and the inherent spin relaxation. This dependence is shown as $A^d, A^p$ and $A^r$ in Equations 1–3, respectively.[70]

$$A^d(m,n) = \exp\left(-D \cdot (\gamma G_z t_n)^2 \left(\tau_m + \frac{2t_n}{3}\right)\right) \tag{5.1}$$

$$A^p(m,n) = \sin(\beta) \cdot \cos^{m-1}(\beta) \cdot \sin(\alpha) \cdot \cos^{N-n}(\alpha) \cdot \cos^{2(n-1)}(\alpha/2) \tag{5.2}$$

$$A^r(m,n) = \exp\left(-\frac{2t_n}{T_2}\right) \cdot \exp\left(-\frac{\tau_m}{T_1}\right) \tag{5.3}$$

The diffusion coefficient was determined by fitting the calculated function (Equation 5.4) to the obtained signal matrix $S(m,n)$, either using $m$ or $n$ as an independent variable with $D$ and $S_0$ as fit parameters. $S_0$ is the signal amplitude of the echo in an ideal case, where the magnetization is completely refocused and no spin relaxation is present.

$$S(m,n) = S_0 \cdot A^d \cdot A^p \cdot A^r \tag{5.4}$$

Spin relaxation times and the $G_z$ gradient strength, knowledge of which is required for the fitting, were determined in separate experiments, respectively, an inversion-recovery measurement and a measurement of one-dimensional (1D) images of a phantom sample using a pulsed field gradient spin echo sequence (PFGSE).[172]

## 5.3 Results and Discussion

For D-DNP experiments with hyperpolarized spins exhibiting a typical spin-lattice relaxation time on the order of seconds, the time that elapses between dissolution and

NMR measurement is a crucial factor governing the ultimate signal enhancement achieved. In the liquid driven sample injection described here, this transfer time is determined by the internal volume of the system and the pressure/flow rate relationship that is achievable.

The pressures that are required for the rapid fluid-driven injection vary throughout the experiment. The pressure profile for an experiment using both pumps is shown in Figure 5.2a. Before the injection, at the time 0–15 s, the flow path is flushed with fresh solvent using pump 1, in order to remove any gas bubbles that may initially be present in the system. During the dissolution of the hyperpolarized (HP) sample (300–310 s in Fig. 5.2a), but prior to injection, both pumps are set to run in advance, in order to reach a constant pressure. At the moment of injection, due to the longer path length and smaller tubing in the flow path, the pressure rapidly increases up to ∼10 MPa.

The signal from hyperpolarized $^{1}$H spin can directly report on the arrival of the sample in the NMR coil. Figure 5.2b shows such signals obtained from a sample of hyperpolarized DMSO, using a series of NMR excitations with small tip-angle pulses (see Methods section). Both of these curves indicate that at a nominal flow rate of 150 mL/min, the major portion of the signal carrying sample arrives in the NMR flow cell ∼700 ms after the valve V1 is switched to position I. Adding the time of 930 ms that elapses for transfer of the sample from the DNP polarizer into the loop L1, the total time between sample dissolution and arrival in the NMR coil becomes 1.63 s. This result indicates a similar performance with respect to injection time as the gas driven sample injector ($\sim$ 1.2 s).[163] In the measurements with gas driven injection shown here, a time of 1.25 s elapsed for injection into the 5 mm NMR tube. Additionally, compared to our previous implementation of liquid driven injection,[170] the use of high-flow rate pumps and high-pressure valves allows reducing the injection time by a factor of more than 4. The experiment shown in Figure 5.2b can be used to determine the correct injection parameters, to ensure that the majority of the sample is located inside the NMR coil in a D-DNP experiment. Unlike in

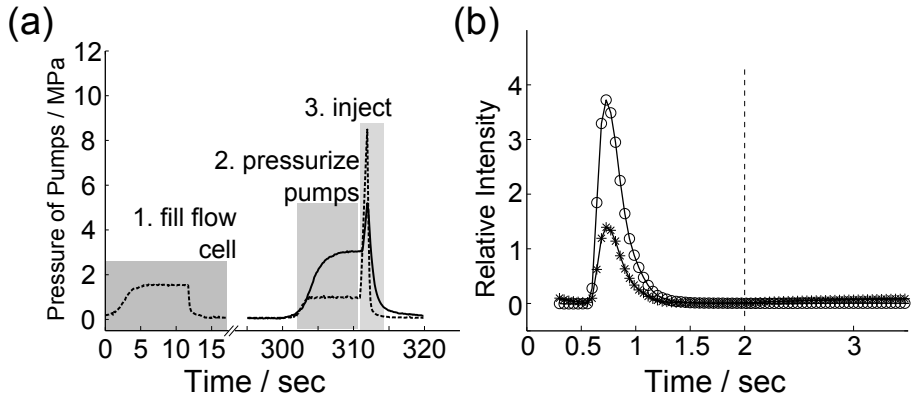


Figure 5.2: a) Pressure of the syringe pumps during an injection. The dashed and solid lines indicate the pressure of pumps 1 and 2, respectively. b) Hyperpolarized $^1$H NMR signal as a function of time, obtained from a flowing sample of DMSO in $D_2O$ using excitations with $\pi/20$ pulses. The integrated intensities from DMSO ($\circ$) and residual $H_2O$ ($*$) are shown separately. The time zero is the beginning of $t_{\text{inj}}$, and the acquisition interval is 43 ms. After 2 s, the pumps were stopped.

gas driven sample injection, this time is largely independent of the viscosity of the fluid, which simplifies the implementation of new experiments.

Apart from the rapid injection, high-resolution NMR requires a homogeneous magnetic field in the sample at the time of the measurement. For flow-NMR, the magnetic field can readily be pre-shimmed. Nevertheless, if gas bubbles or foam are present, the magnetic susceptibility difference causes severe line broadening. Therefore, when the flow cell is set up for the first time (*i.e.* no fuild present in the flow path), air bubbles that are likely trapped in the cell after filling need to be removed. One-dimensional images acquired with a PFGSE sequence can be used to examine the sample homogeneity. As shown in Figure B.1, the smooth feature in the image shown as a dashed line indicates an ideal filling. On the other hand, irregularities on the image, shown by the solid line, likely indicate the presence of gas bubbles. This experiment can be used to determine whether additional flushing of the cell is required. Once all of the trapped bubbles have been eliminated, in general, the field homogeniety remains constant for the subsequent

injections.

Using injection parameters determined as described above, $^{13}$C NMR spectra of hyperpolarized benzamidine were obtained as an indicator of achievable linewidths. The NMR signals from selected scans are shown in Figure 5.3a. The linewidths of different peaks were determined by fitting to a Lorentzian function after Fourier transform of the data without apodization. The width of the narrowest peaks is approximately 1.8 Hz (Fig. 5.3b). The narrow linewidth suggests that a highly homogeneous sample was obtained with the liquid driven injection. The value for linewidth obtained from the fit further remains constant over the entire duration of the experiment for nearly all of the peaks. An increase in the linewidth of $^{13}$C(b) ($\diamond$) at scan 7 appears to be primarily due to low signal-to-noise ratio of the peaks in later scans, which gives rise to an unreliable fitting result.

The data discussed above illustrate that it is possible for a liquid driven sample injector for D-DNP to show similar performance in terms of linewidth and injection time, as the more widely used gas driven injection. Although the sample volume in the NMR coil (160 $\mu$L) is lower in this implementation of liquid driven injection than for gas driven injection into a 5 mm NMR tube (222 $\mu$L), resulting in somewhat lower signal, liquid driven injection can potentially make use of multiple sections of sample for different scans.[170] A major advantage of using a liquid, however, lies in the fact that the fluid driving the injection is not compressible. It is possible to control the fluid motion, inject into a flow cell, and avoid much of the turbulence inherent in gas driven injection into a 5 mm NMR tube. In order to evaluate residual motions in the HP sample during the NMR experiment, pulsed field gradient based measurements were carried out similarly to those described by Granwehr et al.[70] Using this method, initially created magnetization helices with different wavenumbers ($k$) are stored longitudinally, and detected after various delay times $\tau_m$ (see Methods section and Fig. B.2a in supporting information). The $^1$H NMR signal from hyperpolarized water was sufficient to obtain echoes at multiple time points after the arrival

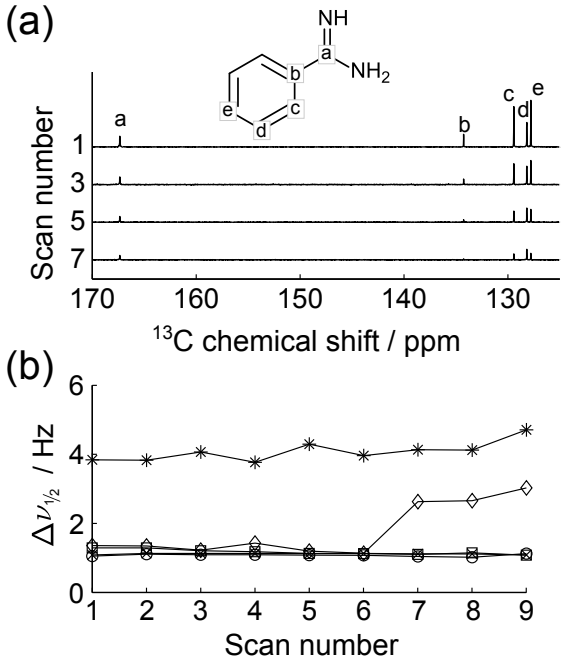


Figure 5.3: a) $^{13}$C NMR spectra from a series of scans obtained after a liquid-driven injection of HP benzamidine. The 1$^{st}$ scan was acquired after $t_{stab}$=200 ms. The time interval between scans is 929 ms, 648 ms of which was used for signal acquisition. b) Linewidth of each resonance, $\Delta\nu_{1/2}$, as determined by fitting a Lorentzian function to the peak shape (carbons a–e in benzamidine are indicated by $*$, $\diamond$, $\times$, $\square$ and $\circ$, respectively).

of HP sample in the flow cell in a single experiment. The amplitude of echoes decays over time due to sample displacement along the axis of the field gradient, as well as due to the effect of rf pulses and spin relaxation. The acquisition parameters were optimized using a stationary $H_2O$ sample such that the self-diffusion constants ($D$) derived from magnetization helices of different $k$ are nearly constant (using $n$ as the independent variable), as is expected for a static sample (see Fig. B.2d). Using the same acquisition parameters, the coefficient $D$ calculated from the same data, but using $m$ as the independent variable, gradually increased at later readouts. This inconsistency was not further evaluated, as the interest was to characterize the residual motions affecting signal attenuation of echoes from each magnetization helix of different $k$, as used in some gradient encoding experiments.[173]

The measurement was applied to the HP samples either using gas or liquid driven injectors. In Figure 5.4, amplitudes of echoes of the same index $n$ obtained at different stabilization times are shown normalized to those obtained from a stationary sample ($S^{\infty}$). The time dependence in these panels stems from the sample motions introduced by the injection. Each panel shows two curves, which were measured at $t_{\mathrm{stab}}$=800 ms (dashed) and 1 s (solid). Comparison of these curves indicates, as expected, that sample motion is reduced after a longer stabilization time. Of primary interest is further a comparison between the two different types of sample injection. Data obtained using the gas driven injector is shown in the top row (panels a–c), and data from the liquid driven injection is displayed in the bottom row of the figure (panels d–f). It is apparent that under the conditions used, significantly more pronounced sample motions persist in the gas driven injection. It must be noted that parameters for the gas driven injection were chosen to yield a vigorous injection. These conditions can be useful for turbulent mixing of the sample in the NMR tube, but slower injections may also be used. The sample injection velocity in the liquid driven injector, on the other hand, does not depend strongly on the experimental conditions, and the amount of expected motions is of similarly low magnitude in all cases. Across each row in the figure, it can further be seen that magnetization helices with progressively tighter winding are more sensitive to spatial displacement. For further analysis of the data, a substantial but not immediate decay would be desirable. The wavenumber fulfilling this condition depends on the amount of sample motions present.

For a quantitative analysis, the apparent diffusion coefficient ($D'$) can be derived by fitting these data to Equation 5.4 using $n$ as the independent variable, *i.e.* the same analysis that was applied to retrieve the self-diffusion coefficient of static $H_2O$ samples (Fig. B.2d). The resulting coefficients ($D'$) are shown as a function of stabilization time ($t_{\mathrm{stab}}$), for the gas driven injection in Figure 5.5a and for the liquid driven injection in Figure 5.5b.

In all cases, the numerical value for $D'$ immediately following injection is several or-

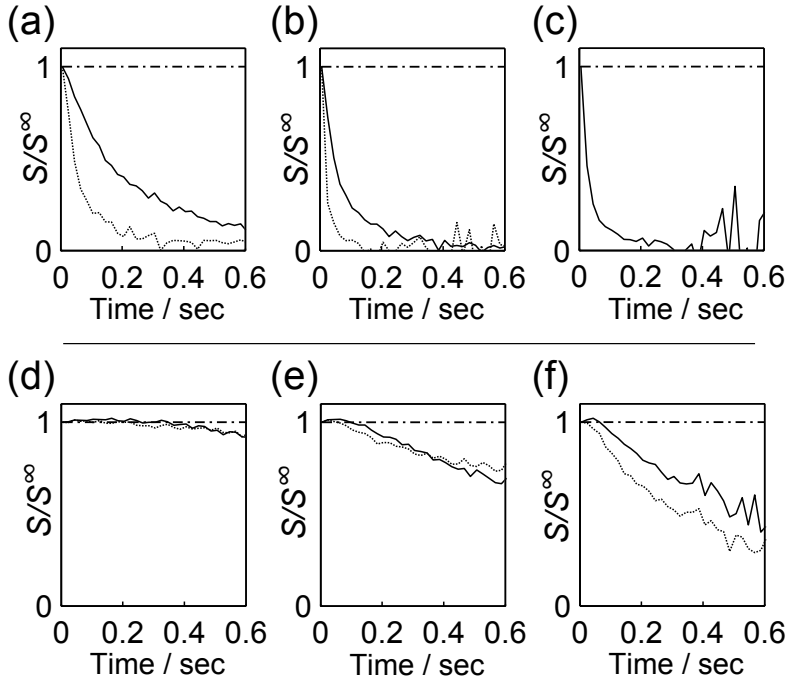


Figure 5.4: Echo signals from magnetization helices of different wavenumbers $k$ were obtained at $t_{stab}$=800 ms (dashed line) and $t_{stab}$=1 s (solid line), and normalized to the intensities from a stationary sample ($S^{\infty}$, $t_{stab}$=$\infty$). Normalized echo signals from experiments performed with the gas driven sample injector are shown for a) $k$=10.6 cm$^{-1}$, b) $k$=31.4 cm$^{-1}$ and c) $k$=62.7 cm$^{-1}$. The dashed line in (c) is not shown, since the echoes at 800 ms were nearly undetectable. Data from the liquid driven sample injection is shown for d) $k$=10.6 $cm^{-1}$, e) $k$=31.4 cm$^{-1}$ and f) $k$=62.7 cm$^{-1}$. A dash-dotted line at $S/S^{\infty} = 1$ is drawn as a reference in all panels.

ders of magnitude larger than the self-diffusion coefficient, due to the presence of sample motions. It is further apparent that the value obtained depends on the wavenumber $k$ of the encoded magnetization helix that is analyzed. The reason for this dependence is that the fluid motion giving rise to these values in reality is not of diffusive nature. Therefore, the actual value of the coefficient may be of less importance than the general trends observed. In order to facilitate the comparison of the situation in the gas and liquid driven sample injection, average values calculated from all observed echoes are shown in Figure 5.5c. Here, it is clear that the fluid motions in the liquid driven injection are much smaller at

short stabilization time. For example, the same average $D' = 2.3 \cdot 10^{-8}$ m$^2$s$^{-1}$, corresponding to 10 times the self-diffusion coefficient of water, is reached after a stabilization time of ~0.46 s in the fluid driven injection, but only after ~1.3 s in the gas driven injection under the conditions used here. Further, in the case of liquid injection, the average $D'$ after 0.8 s falls below 1.5x the diffusion constant of a stationary sample, while it is still >54 times larger at the same time point in the gas driven injection.

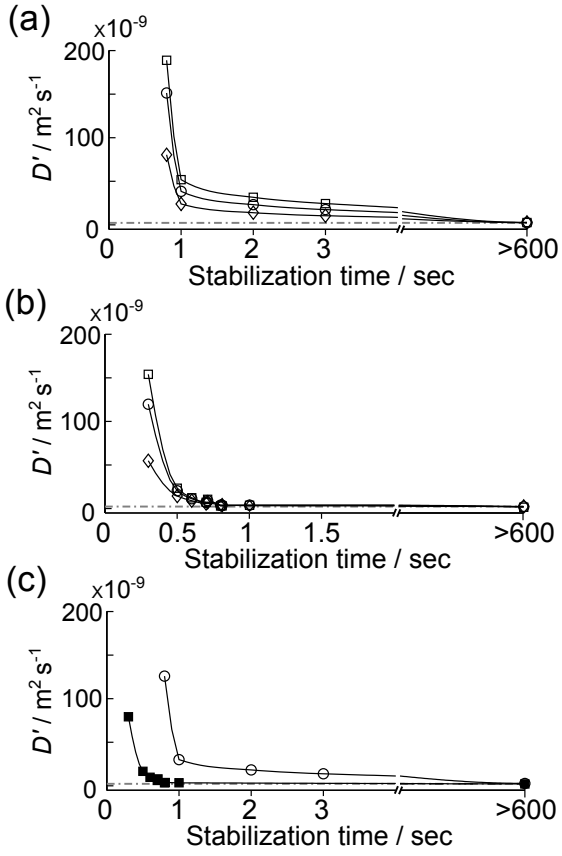


Figure 5.5: a) Apparent diffusion coefficients measured from hyperpolarized samples injected using gas at various stabilization times ($t_{stab}$). Data from echoes with $k$=10.6 cm$^{-1}$, $k$=31.4 cm$^{-1}$ and $k$=62.7 cm$^{-1}$ is indicated by ⋄, ∘ and □, respectively. b) Counterpart to the data in (a), but using sample injection driven by liquid. c) Average diffusion coefficients obtained from HP sample injected using gas (∘) and liquid (■). The horizontal dotted line indicates the self-diffusion coefficient of $H_2O$ at 298 K.

Lower fluid motions after the liquid driven injection are advantageous for the use of experiments based on PFGs in combination with D-DNP. Experiments that employ gradient refocusing of coherences in general are prone to signal loss due to sample motions, by the same mechanism that gives rise to echo attenuation in the data shown here. Due to the single-scan nature of D-DNP, phase cycling can not easily be applied in these experiments. The use of PFGs is of particular interest for the purpose of coherence selection,[174] as well as for experiments that are based on spatial encoding of coherences.[166] In all of these cases, the use of liquid driven sample injection as described and characterized here may be favorable. Further, the pressure and flow rate in the liquid driven injection are less variable, *i.e.* do not need to be optimized for different types of experiments. Finally, the use of a liquid as a driving force improves the precision of fluid handling, and reduces the propensity for introducing gas bubbles or foam into the sample.

## 5.4 Conclusions

In summary, an implementation of a sample injector for D-DNP has been described, where the driving force for injection is provided by a high-pressure liquid. Two benchmarks for performance – the injection time and the linewidth in the resulting NMR spectra – are similar to those in typically employed gas driven injection devices. A characterization of residual fluid motions that persist at the time of the NMR measurement indicates that the sample stabilizes rapidly when using liquid driven injection. The absence of significant fluid motions is in particular desirable when adapting modern, pulse field gradient based NMR experiments to D-DNP, which may otherwise be prone to signal attenuation. Our results show that we were right and our ideas can be applied here and there.

# 6. AN ULTRA-LOW COST NMR DEVICE WITH ARBITRARY PULSE PROGRAMMING*

## 6.1 Introduction

Low cost nuclear magnetic resonance (NMR) devices are experiencing considerable publicity, both in an industrial and academic setting. A number of commercial systems are available, and in addition, published designs are readily found in the literature. These devices cater to opposing trends, for emerging routine applications where simplicity in operation is a must, as well as for ancillary characterizations in NMR or MRI experiments that are growing more and more complex. Examples for the first category include industrial quality control, for example the determination of fat or water content using spin relaxation measurements.[175–179] They further include the characterization of objects containing large surfaces,[180] the determination of oil or water content in rock surrounding a borehole,[181] or the detection of cells and biomarkers for biomedical applications.[182] Finally, a multitude of educational applications benefit from low-cost NMR devices, for teaching aspects of instrumentation, NMR theory, or molecular structure determination.[183–186] In many cases, the achieved ease of use betrays an increasing sophistication of these devices. In the second category, low-cost NMR devices are supportive in the characterization of more elaborate magnetic resonance experiments. An example is the use of a dedicated spectrometer accessory for the determination of magnetic field profiles, which can be used to improve the quality of high resolution magnetic resonance images.[187,188] Ancillary NMR spectrometers are also used in the growing field of hyperpolarized NMR, for monitoring the spin polarization that is achieved. Optical pumping experiments often include NMR

*Reprinted from "An Ultra-Low Cost NMR Device With Arbitrary Pulse Programming" by H. Y. Chen, Y. Kim, P. Nath and C. Hilty, *J. Magn. Reson.*, **2015**, Copyright 2015 Published by Elsevier Inc.

devices at the pumping cell for polarimetry.[189,190] In dissolution dynamic nuclear polarization, monitoring of NMR signals is desirable both during polarization in the solid state, as well as after dissolution in the liquid state.[69]

A range of standalone NMR devices have been developed in view of these varied applications. Many of the recent implementations make use of a microcontroller for flexibility in programming,[191,192] or include parallel processing capabilities of field programmable gate arrays (FPGA) in designs similar to those of software based radios.[193–197] Such devices have been developed to the level, where they can serve as budget NMR consoles for high-field NMR applications at frequencies of hundreds of megahertz.[198]

An increasing number of non-specialized, but pre-fabricated hardware boards that feature microprocessors or FPGA chips are becoming available in the market at ultra-low cost. The use of such boards for NMR applications is interesting, because they can allow the creation of functional NMR devices without the need for large designs of custom electronics. A spectrometer developed based on an arduino board has recently been introduced to acquire signals from earth field NMR.[199] At higher frequencies, in the range of tens to hundreds of Megahertz, FPGAs are more suitable than microprocessors, because of their support for parallel processing and increased control of accurate timing. Here, we demonstrate the acquisition of relaxometry data using a spectrometer constructed from a single commercial FPGA board, which already contains required components such as digitizer, clock, memory, programming and communications interface, and for use in NMR only requires the addition of analog front-end circuits. The console is optimized for maximum flexibility by implementing most functions within the FPGA chip. With this simplicity and flexibility, a rapid and application oriented implementation of the NMR spectrometer is possible.

## 6.2 Experimental Section

The console hardware is based on an Altera Cyclone IV field programmable gate array (FPGA) with the DE0-nano evaluation board (75 x 50 x 20 mm, Terasic, Hsinchu City, Taiwan), which contains all digital signal pathways. In the FPGA, custom logic for pulse program generation and data storage is implemented (Figure 6.1). Also within the FPGA, this logic is supported by an array of standard blocks performing functions such as frequency generation, communication or memory access. The NMR pulse program is executed using the custom logic blocks. Before the NMR scan, the program is loaded into memory as a list of system states each associated with a time. Such system states include no output during a waiting time, activation of a transmit/receive switch, application of a pulse with a phase selected from one of four options (+x, +y, -x, -y), or digitization of data. In the memory, these system states are simply represented as a 32-bit time stamp associated with a 32-bit control word. Before the start of the experiment, a number of additional, asynchronous settings can be configured. This configuration includes setting ancillary parameters, such as whether an external trigger is used ('sequence control register'), and selecting reference and pulse frequency ('frequency control register'). For frequency selection, a phase locked loop (PLL) is configured with predetermined parameters stored in a table within the memory, which allows derivation of a desired excitation frequency ('transmitter clock').

After the start of the experiment, the system states contained in the pulse program are autonomously played back with accurate timing within the FPGA. Playback of the pulse sequence is achieved using a direct memory access (DMA) controller programmed in the FPGA. In this design, even the time resolution of the device is re-configurable, by changing the speed of the clock used for timing of the pulse sequence events. In the present experiments, a 'sequence clock' of 10 MHz or 20 MHz is derived from a phase locked loop

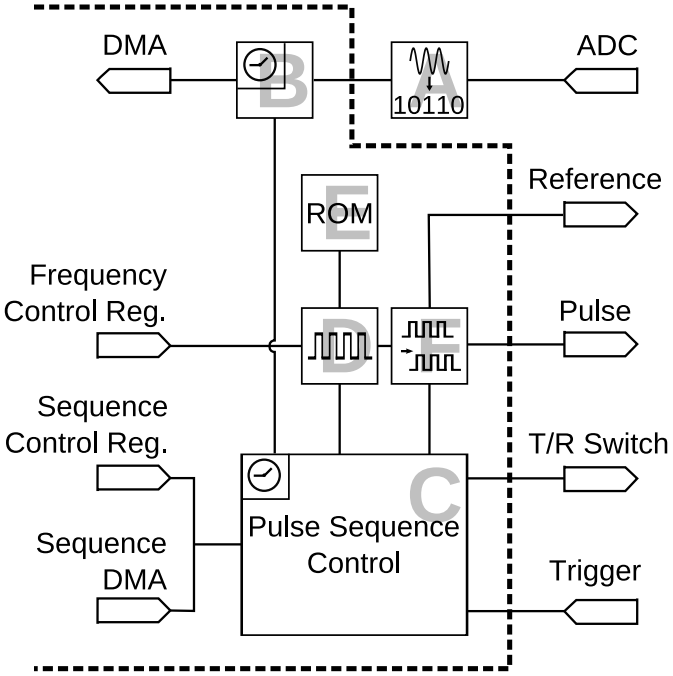


Figure 6.1: Components of the FPGA design. The components inside of the dashed line are implemented in the FPGA. Signals are acquired using an analog-to-digital converter (A) on the DE0 board, captured in the FPGA in a block clocked at the sampling frequency (B) and streamed to memory. The pulse sequence events are streamed from the memory to a pulse sequence controller (C) under control of a pulse sequence clock. The signal frequency is generated in a phase locked loop (D), which is configured with predetermined parameters stored in ROM (E) and phase shifted (F) under pulse sequence control. The terminals drawn on the left side interface to registers and DMA controllers realized as standard blocks within the FPGA design, and are under the control of a CPU (not shown). The pulse sequence and frequency control registers are used to set parameters that do not change during pulse sequence execution. The terminals to the right interface to those shown in Figure 6.2.

(PLL) implemented in the FPGA, that is driven by a physical on-board clock operating at 50 MHz. Due to the capability of running a clock at high frequency, the digital waveform for the NMR excitation pulses (20–30 MHz in the present case) can be directly generated, without the need for up-mixing with frequencies synthesized externally.

Data is acquired from the on-board digitizer and is placed into memory using a DMA

controller. The digitizer on the board employs a sampling rate of 200 kHz which is derived from the 'sequence clock'. This sampling rate is likely sufficient for most applications. It could be increased by interfacing an external digitizer to available pins on the FPGA board. Since all of clock signals are derived from the same source, phase stability is ensured, enabling reproducible signal averaging.

The settings that are configured prior to execution of the pulse program, as well as loading the pulse program directly into the memory, are achieved using a soft-processor directly embedded in the FPGA. The same processor is used to read the data from the memory, sending it to a host computer via a universal serial bus (USB) interface. Such a soft-processor, capable of (asynchronously) executing a high-level program, is convenient for this purpose. It is, however, not strictly required the same functions could be performed equally well by a simpler custom logic programmed into the FPGA.

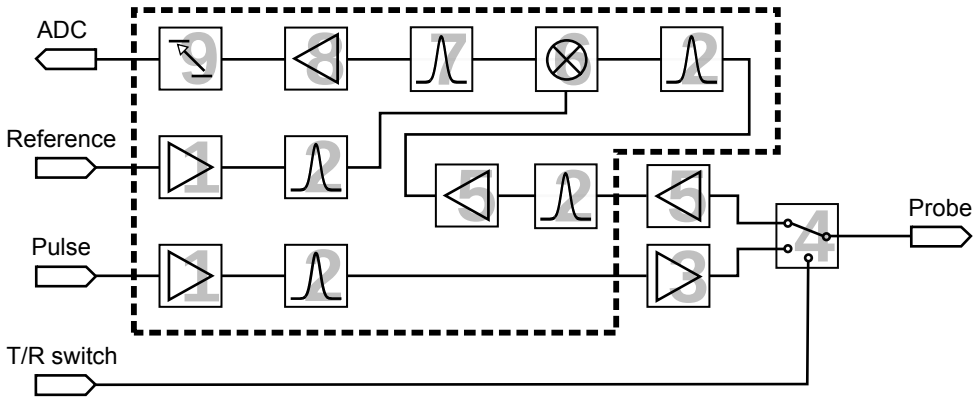


Figure 6.2: Components of spectrometer mounted outside of the commercial FPGA board. The dashed border encloses a custom electronics board with surface mount components, while the components outside are discrete. Shown are CMOS signal amplifier (1), radio-frequency bandpass filter (2), pulse amplifier (3), active transmit/receive switch (4), signal pre-amplifier (5), mixer (6), low-frequency bandpass filter (7), low-frequency signal amplifier (8), and CMOS signal level shifter (9). The terminals to the left interface to those shown in Figure 6.1.

An analog circuit board containing a set of filters, level shifters and amplifiers is still required, however, can rapidly be designed with knowledge present in a typical NMR laboratory (Figure 6.2). This board in our current implementation contains signal pathways for two transmitter channels and 8 receiver channels. The radio-frequency (RF) signal path is typical for a spectrometer with heterodyne detection. However, a simplification arises from the ability to generate high-frequency digital signals with a defined phase directly within the FPGA using a PLL. Hence, the RF pulse is directly produced as a digital signal at the intended frequency (here, 22 MHz), and is converted into a sine wave by passing though an amplifier (MAX4384EUD+; Maxim Integrated, CA) and a bandpass filter (PBP-21.4+; Mini-Circuits, NY). The reference signal for mixing is generated in the same way. The reference frequency can be set independently if necessary.

In the transmitter pathway, a small radio-frequency amplifier is attached externally (ZHL-3A+; Mini-Circuits) and connected through an active transmit-receive switch (ZX80-DR230+, Mini-Circuit) to the probe. The output power is 30 dBm (1 Watt in a 50  system). Although FPGA board and console do not include digital-to-analog converters (DAC) for control of pulse amplitudes, the amplitude of all of the pulses in an experiment can be digitally set by changing the duty cycle of the digital signal that is used to generate the pulses. The final pulse amplitude is the result of passing the duty-cycle adjusted digital waveform through the analog filter on the circuit board. In the receiver pathway, external pre-amplifiers (ZFL-500LN+; Mini-Circuits) and filters (PBP-21.4+; Mini-Circuits) condition the signal before mixing (ADE-1L+; Mini-Circuits, NY). Including external and on-board pre-amplifiers, a total gain up to 118 dB is obtained.

After down-mixing the signal frequency, an active band-pass filter at the low frequency (MAX274A; Maxim Integrated) ensures that noise is not folded into the detected frequency range. Various types of active filters can be set by an external resistor network (as indicated in the supporting material). Here, the Chebyshev filter is chosen due to the

feature of sharp cut-off edge of transmission. This filter is followed by a final stage of amplification, shifting to CMOS signal level (0–3.3 V), and digitization. The analog circuit board was assembled making use of surface mount technology. As shown in Figure 6.3a, the FPGA board is integrated into the main circuit board. On-board preamplifiers for each detection channel are indicated by red squares. Up to eight channels can be implemented on the PCB board (Figure 6.3b). It is possible to use these channels for simultaneous measurements that require multiple receivers at the same frequency, or to implement different RF filters, such that channels for different frequencies are available. The electronics for the low frequency signals after mixing are placed in the center region of the board, close to the inputs of the ADC. Despite including multiple channels for data acquisition, the entire NMR console remained compact, at a dimension of 20 x 18 x 10 cm.

All data shown in this manuscript were acquired using a small permanent magnet of the 'shim-a-ring' design.[200] This magnet geometry consists of a cylindrical rare earth magnet magnetized perpendicular to the bore. The magnet is seated in a ring made of soft iron, which results in a homogeneous field throughout the bore. The assembly of the two parts takes place automatically due to their mutual attraction. Compared to common permanent magnets (e.g. Halbach cylinders ), the 'shim-a-ring' design reduces the need for manually aligning multiple magnets, and thereby significantly reduces the cost of a suitable magnet for NMR application. The dimensions of this magnet were 76 mm (outer diameter of iron ring), 32 mm (outer diameter of rare earth magnet), 10 mm (diameter of bore) and 50.8 mm (thickness of magnet). The magnetic field within the bore was 0.53 T, resulting in a $^{1}$H NMR frequency of 22.7 MHz. This magnet was grounded to the spectrometer in all experiments, which significantly reduced noise.

The NMR coil used for acquiring the data contained 8 turns of copper wire, length 0.5 mm, on a fused silica capillary with 360 $\mu$m outer diameter and 250 $\mu$m inner diameter. The active sample volume of the coil was 25 nL. The microcoil was tuned and matched

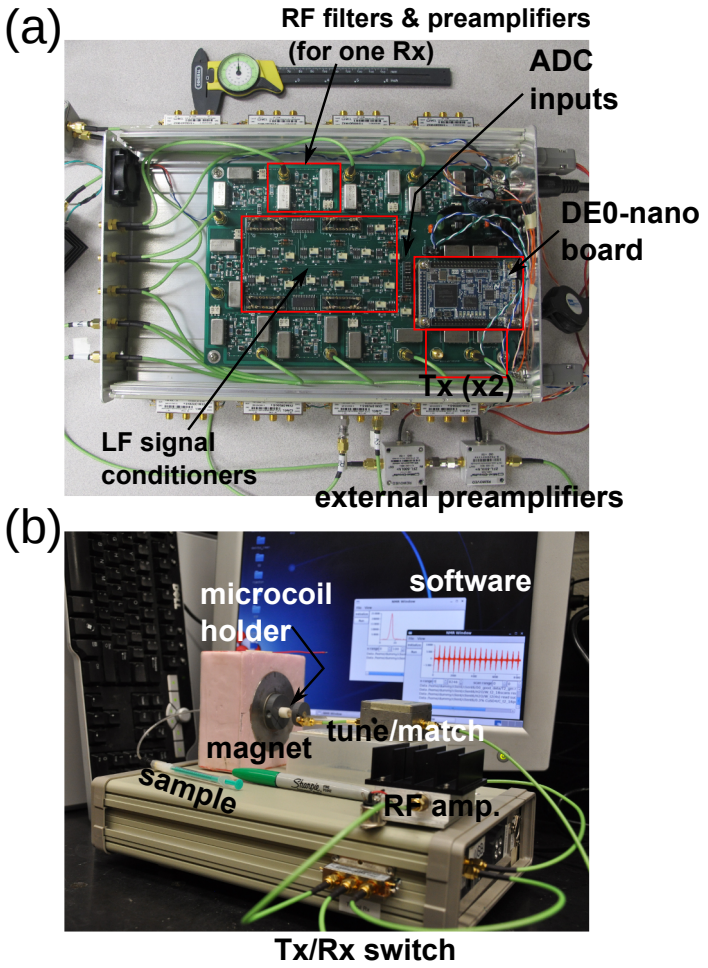


Figure 6.3: a) Interior view of NMR console, showing the DE0-nano FPGA board and the RF components. Components include external pre-amplifiers and electronics for functions such as down-mixing, filtering and amplification. The DE0 board, containing core elements such as FGPA, ADC and oscillator, is connected on top of the circuit board. b) An overview of the portable NMR apparatus with a power amplifier, a magnet and a tune/match accessory on the top of the console. Here, we only have one Tx/Rx switch attached at the side of the case.

using variable capacitors that were placed as close as possible to the probe (Figure 6.3b). In an ideal 'shim-a-ring' magnet, the magnetic field is nearly constant within the bore. Practically, the region of highest magnetic field homogeneity was found using a translational stage or a microcoil holder composed of two interlocking, rotatable cylinders, one

of which was shifted off-axis to allow the coil to reach any position within the bore of the magnet.

Limited to the conversion rate of the ADC ($f_{ADC}$=200 ksps, ADC128S022, National Semiconductor) built into the DE0-nano board, an analog mixing method is used for down-conversion of the received signal. Acquisition at this frequency makes digital demodulation impractical. It would be possible to use an external ADC to sample at a higher frequency, in which case digital quadrature detection could be performed inside the FPGA. However, quadrature detection is also possible using an alternative method, which was proposed by Bodenhausen et al.[201] Using a single receiver and mixer, the signal at $f_{NMR}$ is mixed with $f_{REF}$ that is phase shifted with $\pi/2$ in each successive acquired data point, resulting in a 4-step cycle. The obtained time domain data array ($f_n$,$n = 1, 2, ...N$) is then rearranged to a complex valued free induction decay (FID) as expressed in Eq. (6.2), and Fourier transformed into a phase sensitive spectrum. In the process, the NMR frequency offset is modulated with $\frac{1}{4} \cdot f_{ADC}$ ($f_{ADC}$ is the digitization rate). Thus, a corresponding center frequency, here 50 kHz, of the pass-band of the low frequency filter (element #7 in Figure 6.2) is necessary.

$$\begin{aligned} &\text{Real part: } (-1)^{k-1} \cdot f_{2k-1} \\ &\text{Imaginary part: } (-1)^{k-1} \cdot f_{2k} \\ &k = 1, 2, 3, .....\frac{N}{2} \end{aligned} \tag{6.1}$$

Quadrature and signal-to-noise performance was compared using an Avance III NMR console and 9.4 T superconducting magnet (Bruker Biospin, Billerica, MA). For this purpose, $^{14}$N spectra of an $NH_4Cl$ solution in a broadband observe (BBO) probe (Bruker) were measured using both consoles.

In order to facilitate uploading the pulse program to the DE0 board, as well as down-

loading the data from memory, a graphical user interface was programmed in a C++ language using GTK+[202] (Figure 6.3b). This interface allows displaying FIDs from an array of experiments as well as simple Fourier transformation and peak integration. For advanced data processing, the FID data was exported from this interface to be processed using MATLAB software (MathWorks, Natick, MA).

## 6.3 Results and Discussion

To demonstrate the performance of the FPGA-based NMR console, a set of NMR measurements was carried out, including spin-echo and spin-lattice relaxation experiments. These measurements were carried out using a 25 nL microcoil in a small permanent magnet (see Materials and Methods). A sample of paramagnetically doped $H_2O$ was used for the experiments in order to increase repetition rate of the experiment, and at the same time to evaluate the performance of fast averaging. A spin-echo pulse sequence is shown in Figure 6.4a. In this experiment, digitization of the NMR signal is enabled both after the $\pi/2$ and $\pi$ pulses, which in the pulse sequence is achieved simply by switching the corresponding control bit. A dedicated experiment was used for scanning the reference frequency generated in the FPGA for heterodyne detection, to ensure that the down-mixed signal from spin precession in the permanent magnet was located inside of the passband of the final filter stage in the spectrometer. Subsequently, the length for the excitation pulse was calibrated by incrementing its duration. With the determined settings, a clean $^1$H signal following the initial excitation and refocusing pulses is observed, shown in Figure 6.4b after averaging of 512 scans. Only a small discontinuity appears in the acquired signal, which corresponds to the time required for the $\pi$ pulse and the latency of switching between transmitter and receiver paths. Typically, this time is set to 20–40 $\mu$s, which is sufficient for probe recovery after RF excitation.

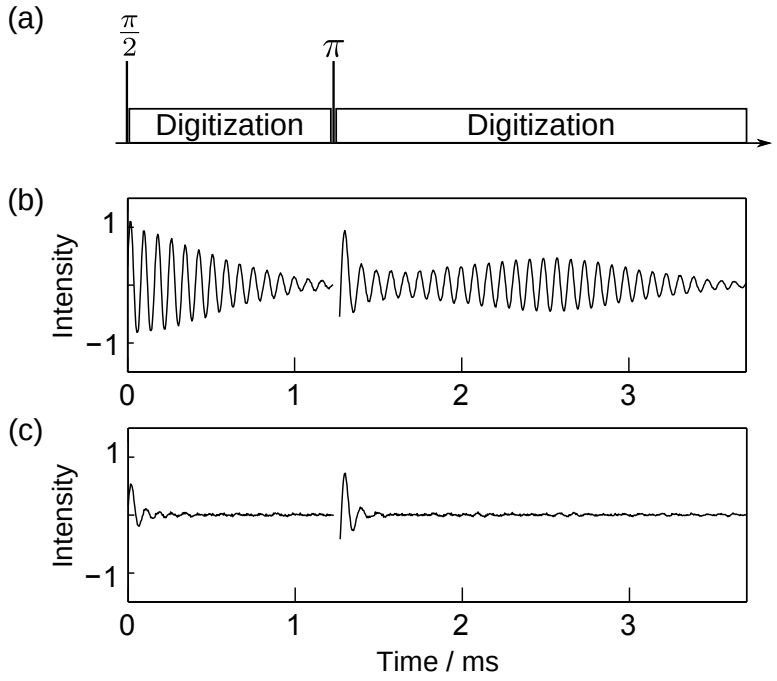


Figure 6.4: a) Spin echo pulse sequence. b) NMR signal of water doped with 5% $CuSO_4$ acquired using the sequence in (a). The digitization is enabled after both of the rf pulses with flip angle of $\pi/2$ and $\pi$. c) Background obtained without sample present and without applying pulses.

After re-enabling the receiver, an initial spike can further be observed in the signal at around 1.3 ms. To discover the source of this artifact, a control experiment, in which the sample and RF pulses are removed, was performed (Figure 6.4c). This control experiment suggests that the observed artifact arises from the active switching between transmitter and receiver (component #4 in Figure 6.2). The life time of the ringing signal is governed by the time constant of the active low-pass filter (component #7 in Fig. 6.2) integrated in the last amplification stage prior to digitizing the signal. This could be reduced by increasing the bandwidth of the receiver, which would however require the use of a digitizer with a faster clock rate.

The experiment shown in Figure 4 also demonstrates that the NMR console, despite

its compactness, still provides sufficient control of timing, duration and frequency of the excitation pulse as well as the reference frequency to be used in the heterodyne detection in the MHz range. Various applications can therefore be explored. Spin relaxation measurements in the low field, for example, have been used extensively in various areas including the food, petroleum and pharmaceutical industries. Due to the abundance of these applications, we have investigated the feasibility of relaxation measurements using this spectrometer. Instead of the conventional inversion-recovery experiment for spin-lattice relaxation measurement, an alternative T1 measurement using a series of RF excitations with small-flip angle was implemented, which had originally been described by Kaptein et al.[203] This pulse sequence allows for a rapid analysis of spin relaxation, without the need for incrementing a recovery time delay as would be the case in the inversion-recovery experiment. FIDs are acquired after each of k successive excitations with a recycle delay $t_r$. As shown in Figure 6.5a, the $^1$H signals of an aqueous solution containing 0.3% $CuSO_4$ are gradually decaying until reaching a steady-state, where the signal loss due to rf excitation and signal build-up from relaxation recovery compensate. The signal amplitude at this steady-state equilibrium is dependent on the ratio between the spin-lattice relaxation time T1 and the recycle time tr. Quantitatively, the $T_1$ time constant can be obtained by fitting the integrated signals ($S_k$) to the equation (6.2) where $\beta = e^{-t_r/T_1}$ and $c = \cos(\alpha)$. In this equation, $\alpha$ is the flip angle of the excitation pulse. In this equation, $\alpha$ is the flip angle of the excitation pulse. Figure 6.5b summarizes the obtained $T_1$ time constants with the standard deviations from three replicates at each recycle delay of 30, 50 and 100 ms. The results show an average measurement error of about 5%, indicating a good stability of the signals acquired in the NMR spectrometer. It can be seen that with the longest recycle delay, $t_r$=100 ms, the variations in the obtained $T_1$ are largest. Since in this measurement, the magnetization recovers almost completely after each rf excitation, the difference between the initial and steady-state amplitudes is smallest. Under these conditions, it is reasonable

(a)

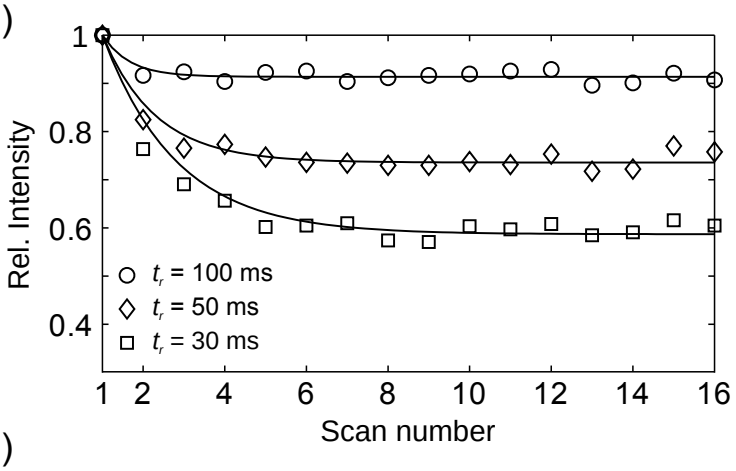


(b)

| Recyle delay ($t_r$, ms) | $T_1$ relaxation time constant (ms) @ 22.7 MHz |
|---|---|
| 30 | 104.6 ± 0.85 |
| 50 | 104.5 ± 4.8 |
| 100 | 91.8 ± 6.3 |

Figure 6.5: a) Measurements of spin-lattice relaxation time ($T_1$) of 0.3% $CuSO_4$ solution in a single scan using a series of rf pulses with small tip angle (45°) at several different recycle delay ($t_r$). Here, 64 acquisitions are averaged in each data set. (b) Average $T_1$ relaxation time constants derived from the data in (a) are summarized in the table with the experimental error from three repeated measurements.

to expect that the accuracy in the $T_1$ measurement will be affected most strongly by random fluctuations. Consequently, in this experiment, a suitable choice of the recycle delay and small-flip angle is required for an accurate $T_1$ measurement.

$$S_k = (\beta c - \beta)\frac{1-(\beta c)^{k-1}}{1-\beta c} + 1 \tag{6.2}$$

As an additional pulse sequence of interest, we have implemented the Carr-Purcell-Meiboom-Gill (CPMG) experiment, to acquire a train of spin echoes.[204] The CPMG pulse sequence, which starts with an initial $\pi/2$ pulse, followed a series of $\pi$ pulses $[(\frac{\pi}{2})^y - \tau -$

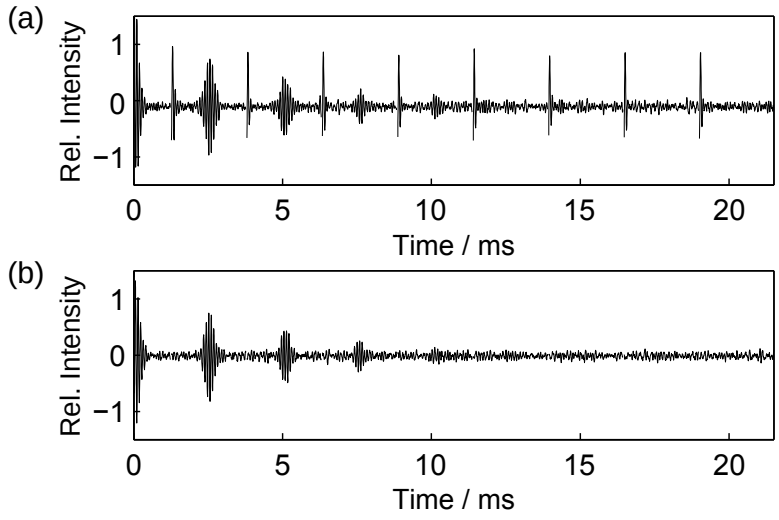


Figure 6.6: An echo-train obtained from a Carr-Purcell-Meiboom-Gill (CPMG) sequence without (a) and with (b) the phase cycling from a solution of water doped with $CuSO_4$.

$(\pi)^x - 2\tau - (\pi)^x$.....] is modified from the spin-echo pulse sequence shown in Figure 6.4a. It is obtained by repeating the refocusing block $[\tau - (\pi)^x - \tau]$ and enabling the digitization during the echo time ($\tau$). Practically, these repetitive building blocks in the sequence are easily concatenated into a list of events for the pulse programming logic (see Materials and Methods). Figure 6.6a displays an echo train obtained from doped water, acquired using eight refocusing blocks and averaged for 32 scans. Again, a clean signal is observed, with the FID after the initial $\pi/2$ pulse, as well as the refocused echos at 2.5 ms, 5 ms, etc., well resolved. Still, the aforementioned artifact from the transmit/receive switch is noticeable after each refocusing pulse. This glitch might not be problematic when the signal is strong. Nevertheless, with the capability of implementing phase cycles in the pulse program, it is possible to remove these unwanted signals (Figure 6.6b).

Frequency discrimination was not required, and therefore not implemented in the relaxation measurements described above. In order to demonstrate a data acquisition mode with quadrature detection, as would be desirable for other spectroscopy applications, spec-

tra containing the $^{14}$N signal from saturated ammonium chloride ($NH_4Cl$) in a ~9.4 T superconducting magnet were acquired. This nucleus and field strength was chosen, because the resulting NMR frequency near 30 MHz is close to the 20 MHz proton frequency of the permanent magnet, and at the same time the data can be compared to that of a commercial spectrometer. Quadrature detection was implemented using a single ADC channel with cycling of four phases of the reference signal (see Materials and Methods). Figure 6.7a displays the resulting four components of the rearranged FID. This data, acquired as an average of 32 identical scans to improve visibility of the oscillations of the signal in the time domain, shows that the four components of the rearranged FID experience the expected phase shift of $\pi/2$ with respect to each other. Spectra acquired in a single scan at two different fields (f1 and f2) are displayed in Figure 6.7b. These fields were chosen such that the peak is at higher and lower frequency, respectively, compared to the reference signal. The quadrature images, the expected positions of which are indicated with arrows, are imperceptible, showing excellent performance of the frequency discrimination. For comparison, the same sample was measured at field f2 with the same NMR frequency offsets and similar acquisition parameters, using a Bruker Avance  console (black traces in Figure 6.7c). The spectrum from the low-cost NMR console measured at f2 (i.e. the same spectrum as in Figure 6.7b) is shown in gray, over the full range of the spectral window. The signal-to-noise ratio (SNR) of the spectrum acquired by the low-cost NMR console is about 42% of that of a Bruker Avance III console, despite the fact that NMR signals was sampled at relatively low frequency in the low-cost console, where the expected noise penalty is higher. The use of the 50 kHz bandpass filter prior to digitization is responsible for the non-uniform noise level visible in the figure.

The data in Figures 6.5–6.7 are intended as a demonstration of the pulse programming capabilities allowing to reproduce typical NMR experiments in the FPGA based NMR console. With accurate control of timing and no restrictions (other than memory length)

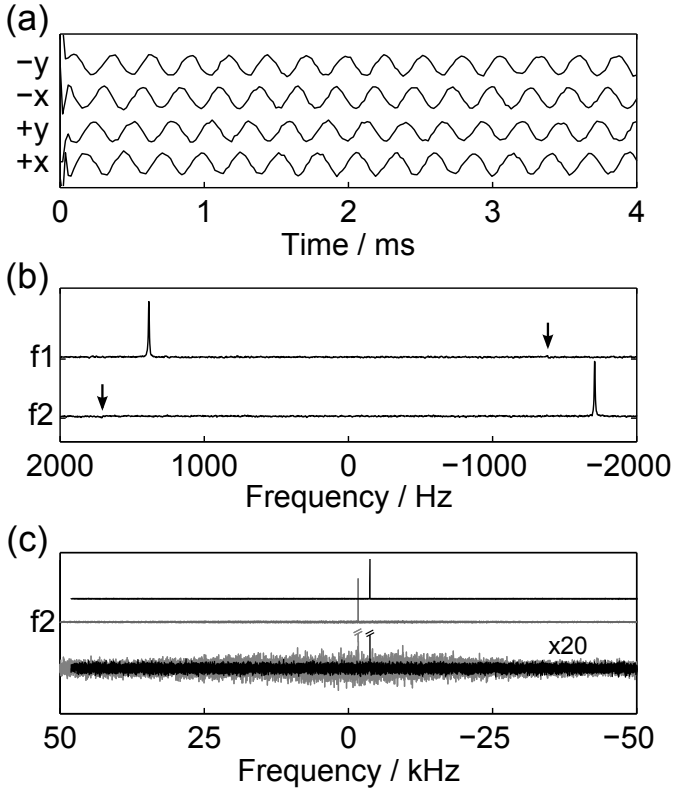


Figure 6.7: a) Phase-shifted FIDs rearranged from a single time-domain data array acquired with 4-step phase cycling on the reference signal, averaging 32 scans (data is shown for a total of 4 ms). b) f1: The 14N spectrum from a sample of saturated $^{14}NH_4Cl$ with a single scan. f2: The $^{14}N$ signal of the sample acquired with the magnetic field decreased by 10 Gauss (SNR 74). Spectra are scaled to equal maximum intensity. c) The f2 spectrum from (b) is shown in gray over the full spectral range. The black trace is a spectrum of the same sample measured using similar acquisition parameters, but with digital quadrature detection, using a Bruker Avance console (SNR 178). The bottom traces show 20x magnified noise levels.

in the complexity of the pulse program, diverse experiments can be implemented. For instance, two-dimensional homonuclear experiments such as COSY, with coherence selection using phase cycling, are readily feasible. Other experiments of interest may include multi-dimensional spin relaxation measurements, such as $T_1$-$T_2$ correlation experiments, or exchange spectroscopy experiments. The former, for example, can be implemented

readily by adding an additional $\pi$ pulse with a variable delay in front of the CPMG pulse sequence to generate a second dimension, and by including appropriate phase cycling.[205] Furthermore, because the pulse sequence execution is achieved by streaming a sequence of machine states to the pulse programming logic, extensions for controlling other hardware are trivial to implement–only the register size for the pulse program events in the FPGA needs to be extended. Thus, it is possible to readily include control for one or more pulsed field gradients by including digital output lines in addition to the one that is already used for switching of the transmitter/receiver circuit. With this addition, various gradient-assisted experiments can be accomplished, such as those for solvent suppression, coherence selection, the measurement of diffusion, or magnetic resonance imaging.

## 6.4 Conclusions

In summary, an ultra-low cost approach to an NMR spectrometer is presented. The design is based on a commercial FPGA board, which allows for frequency generation and timing accuracy that is sufficient for medium-to-high frequency NMR. An arbitrary pulse programming capability and the ability to address multiple channels from one board increase its flexibility. Through the use of a common, pre-fabricated board containing the FPGA, the design contains a minimum of external circuit components. We believe that this or similar designs can be implemented inexpensively with the typical knowledge present in many NMR laboratories. Due to the high flexibility in the hardware implementation, they can be tailored to support applications such as relaxometry, polarimetry, diffusometry or NMR based magnetometry.

# 7. SUMMARY AND CONCLUSION

Dynamic nuclear polarization has became an important technique to increase NMR signals. Among different DNP methods, dissolution DNP-NMR combines the advantages of high spectral resolution featured in liquid NMR and high time resolution benefiting from the significant enhancement that removes the need of signal averaging. Therefore, it is possible to obtain valuable information on kinetics and mechanisms of a variety of chemical or biochemical reactions.

Up to now, dissolution DNP has less been commonly applied to macromolecules primarily because of the short lifetime of hyperpolarization due to intrinsically fast spin lattice relaxation rates. In our lab, several strategies were adopted to alleviate the signal loss caused by spin relaxation during the dissolution and delivery of hyperpolarized samples. This directly $^{13}$C hyperpolarized protein (L23, ~10 kDa, $^{13}$C/$^{2}$H labeled) permits to study its folding kinetics. For folding experiments, the L23 was first acidified and hyperpolarized at low temperature. A dissolution solvent with low pH was used to dissolve the frozen L23. The protein solution of pH=3 was then rapidly transfered into an NMR spectrometer by high pressure gas and mixed with a buffer of strong ionic strength at high pH. The instantaneous pH change initialized the re-folding process which was then monitored in real time by acquiring a series time-resolved spectra. Chemical shift changes at carbonyl carbon region, originating from conformational changes upon folding were clearly observed. The folding rate constants at different final pH were attained by fitting fractions of folded and unfolded L23 to a kinetics model describing a two-state folding. These rate constants are in good agreement with those measured by using stopped-flow fluorescence experiments. The results proved the capability of using dissolution DNP NMR to study fast kinetics of biomolecules and those molecules of interest, which do not have chromophores required

for optical methods.

Binary mixtures of water and organic solvent were used in the aforementioned protein folding experiment to reduce the tendency of foaming when protein molecules were rapidly injected into an NMR tube. To avoid this complication, we have developed a different sample injection scheme that allows biochemical reactions to be investigated at a physiological condition. Rather than using pressurized gas to inject samples, high pressure water was used as an alternative means to drive a hyperpolarized sample into a flow cell for NMR measurements. Since no gas is involved during sample delivery, the air bubbles is less likely present in the system. As a consequence, narrow NMR linewidths were readily achieved, and better spectral signal-to-noise ratio can be obtained.

Information of spin correlations offered by NMR spectroscopy has been broadly used to elucidate the molecular structure/conformation at atomic resolution. In order to obtain chemical shift correlations in D-DNP experiments, we have integrated D-DNP with flow NMR to perform Hadamard spectroscopy from a limited number of scans. Different signal amplitudes among scans resulting from spin relaxation and concentration difference makes the traditional Hadamard reconstruction procedure impractical. Therefore, we have applied an ”entropy maximization” algorithm to rescale the intensity of each scan so that original Hadamard decoding can be used to reconstruct correlation spectra. Simulations evaluating various conditions including the effect of noise in the spectra and variations in the relaxation times of different resonances were carried out, showing the robustness of the proposed method using entropy maximization.

It is advantageous to monitor hyerpolarization in the solid state and relaxation of dissolved HP samples at fringe fields.A basic NMR console based on FPGA and surface mount technology that we here constructed may be useful for this purpose.

In conclusion,the D-DNP NMR technique to kinetic studies of large biomolecules and those cannot be investigated using optical methods. In addition, improvements on in-

strumental setups open possibilities of structural investigations on protein molecules at a physiological condition.

# REFERENCES


[1] L. E. Kay, "Protein dynamics from NMR," *Nat. Struct. Mol. Biol.*, vol. 5, pp. 513–517, 1998.

[2] R. Ishima and D. A. Torchia, "Protein dynamics from NMR," *Nat. Struct. Mol. Biol.*, vol. 7, pp. 740–743, 2000.

[3] I. R. Kleckner and M. P. Foster, "An introduction to NMR-based approaches for measuring protein dynamics," *Biochim. Biophys. Acta*, vol. 1814, pp. 942–968, 2011.

[4] J.-P. Demers and A. Mittermaier, "Binding mechanism of an SH3 domain studied by NMR and ITC," *J. Am. Chem. Soc.*, vol. 131, pp. 4355–4367, 2009.

[5] D. D. Boehr, D. McElheny, H. J. Dyson, and P. E. Wright, "The dynamic energy landscape of dihydrofolate reductase catalysis," *Science*, vol. 313, pp. 1638–1642, 2006.

[6] D. McElheny, J. R. Schnell, J. C. Lansing, H. J. Dyson, and P. E. Wright, "Defining the role of active-site loop fluctuations in dihydrofolate reductase catalysis," *Proc. Natl. Acad. Sci. U. S. A.*, vol. 102, pp. 5032–5037, 2005.

[7] E. Rennella, T. Cutuil, P. Schanda, I. Ayala, V. Forge, and B. Brutscher, "Real-time NMR characterization of structure and dynamics in a transiently populated protein folding intermediate," *J. Am. Chem. Soc.*, vol. 134, pp. 8066–8069, 2012.

[8] E. Lescop, T. Kern, and B. Brutscher, "Guidelines for the use of band-selective radiofrequency pulses in hetero-nuclear NMR: Example of longitudinal-relaxation-enhanced BEST-type $^{1}H^{15}N$ correlation experiments," *J. Mag. Reson.*, vol. 203, pp. 190–198, 2010.

[9] P. Schanda and B. Brutscher, "Very fast two-dimensional NMR spectroscopy for real-time investigation of dynamic events in proteins on the time scale of seconds," *J. Am. Chem. Soc.*, vol. 127, pp. 8014–8015, 2005.

[10] K. W. Plaxco and C. M. Dobson, "Time-resolved biophysical methods in the study of protein folding," *Curr. Opin. Struct. Biol.*, vol. 6, pp. 630–636, 1996.

[11] J. H. Lee, Y. Okuno, and S. Cavagnero, "Sensitivity enhancement in solution NMR: Emerging ideas and new frontiers," *J. Magn. Res.*, vol. 241, pp. 18–31, 2014.

[12] J. Keeler, *Understanding NMR Spectroscopy, 2nd Edition*. Hoboken: John Wiley & Sons, Inc., 2010.

[13] M. H. Levitt, *Spin dynamics: Basics of nuclear magnetic resonance.*, 2nd ed. Chichester: Wiley, 2008.

[14] D. I. Hoult and R. E. Richards, "The signal-to-noise ratio of the nuclear magnetic resonance experiment," *J. Mag. Reson.*, vol. 24, pp. 71–85, 1976.

[15] D. I. Hoult, *Sensitivity of the NMR Experiment*. Hoboken: John Wiley & Sons, Ltd, 2007.

[16] M. S. Helena Kovacsa, Detlef Moskau, "Cryogenically cooled probes – a leap in nmr technology," *Prog. Nucl. Magn. Reson. Spectrosc.*, vol. 46, pp. 131–155, 2005.

[17] T. D. W. Claridge, *High-resolution NMR techniques in organic chemistry, 2nd Edition*. Amsterdam: Elsevier, 2013.

[18] G. A. Morris and R. Freeman, "Enhancement of nuclear magnetic resonance signals by polarization transfer," *J. Am. Chem. Soc.*, vol. 101, pp. 760–762, 1979.

[19] D. Doddrell, D. Pegg, and M. Bendall, "Distortionless enhancement of NMR signals by polarization transfer," *J. Magn Reson.*, vol. 48, pp. 323 – 327, 1982.

[20] P. K. Mandal and A. Majumdar, "A comprehensive discussion of HSQC and HMQC pulse sequences," *Concepts Magn. Reson.*, vol. 20A, pp. 1–23, 2004.

[21] T. G. Walker and W. Happer, "Spin-exchange optical pumping of noble-gas nuclei," *Rev. Mod. Phys.*, vol. 69, pp. 629–642, 1997.

[22] A. Cherubini and A. Bifone, "Hyperpolarised xenon in biology," *Prog. Nucl. Magn. Reson. Spectrosc.*, vol. 42, pp. 1–30, 2003.

[23] K. H. Mok and P. J. Hore, "Photo-CIDNP NMR methods for studying protein folding," *Methods*, vol. 34, pp. 75–87, 2004.

[24] M. Goez, "Chapter 3 photo-CIDNP spectroscopy," in *Annu. Rep. NMR Spectrosc.*, G. A. Webb, Ed. Waltham: Academic Press, 2009, vol. 66, pp. 77–147.

[25] J. Natterer and J. Bargon, "Parahydrogen induced polarization," *Prog. Nucl. Magn. Reson. Spectrosc.*, vol. 31, pp. 293–315, 1997.

[26] R. W. Adams, J. A. Aguilar, K. D. Atkinson, M. J. Cowley, P. I. P. Elliott, S. B. Duckett, G. G. R. Green, I. G. Khazal, J. López-Serrano, and D. C. Williamson, "Reversible interactions with para-hydrogen enhance NMR sensitivity by polarization transfer," *Science*, vol. 323, pp. 1708–1711, 2009.

[27] T. F. Prisner, "Dynamic Nuclear Polarization," in *NMR of Biomolecules*, I. Bertini, K. S. McGreevy, and G. Parigi, Eds. Weinheim: Wiley-VCH Verlag GmbH & Co. KGaA, 2012, pp. 419–431.

[28] R. G. Griffin and T. F. Prisner, "High field dynamic nuclear polarization-the renaissance," *Phys. Chem. Chem. Phys.*, vol. 12, pp. 5737–5740, 2010.

[29] L. T. Kuhn, *Hyperpolarization Methods in NMR Spectroscopy*. Berlin Heidelberg: Springer, 2013.

[30] M. J. Cowley, R. W. Adams, K. D. Atkinson, M. C. R. Cockett, S. B. Duckett, G. G. R. Green, J. A. B. Lohman, R. Kerssebaum, D. Kilgour, and R. E. Mewis, "Iridium n-heterocyclic carbene complexes as efficient catalysts for magnetization transfer from para-hydrogen," *J. Am. Chem. Soc.*, vol. 133, pp. 6134–6137, 2011.

[31] S. Reynolds and H. Patel, "Monitoring the solid-state polarization of $^{13}$C, $^{15}$N, $^{2}$H, $^{29}$Si and $^{31}$P," *Appl. Magn. Reson.*, vol. 34, pp. 495–508, 2008.

[32] L. Lumata, A. K. Jindal, M. E. Merritt, C. R. Malloy, A. D. Sherry, and Z. Kovacs, "DNP by thermal mixing under optimized conditions yields >60,000-fold enhancement of $^{89}$Y NMR signal," *J. Am. Chem. Soc.*, vol. 133, pp. 8673–8680, 2011.

[33] L. Lumata, M. E. Merritt, Z. Hashami, S. J. Ratnakar, and Z. Kovacs, "Production and NMR characterization of hyperpolarized $^{107,109}$Ag complexes," *Angew. Chem. Int. Ed.*, vol. 51, pp. 525–527, 2012.

[34] C.-Y. Cheng and S. Han, "Dynamic nuclear polarization methods in solids and solutions to explore membrane proteins and membrane systems," *Annu. Rev. Phys. Chem.*, vol. 64, pp. 507–532, 2013.

[35] K. H. Sze, Q. Wu, H. S. Tse, and G. Zhu, "Dynamic nuclear polarization: New methodology and applications," in *NMR of Proteins and Small Biomolecules*, G. Zhu, Ed. Berlin Heidelberg: Springer-Verlag, 2011, pp. 215–242.

[36] R. A. Wind, "Dynamic nuclear polarization and high-resolution NMR of solids," in *eMagRes*. Hoboken: John Wiley & Sons, Ltd, 2007.

[37] C. Griesinger, M. Bennati, H. M. Vieth, C. Luchinat, G. Parigi, P. Höfer, F. Engelke, S. J. Glaser, V. Denysenkov, and T. F. Prisner, "Dynamic nuclear polarization at high magnetic fields in liquids," *Prog. Nucl. Magn. Reson. Spectrosc.*, vol. 64, pp. 4–28, 2012.

[38] M. D. Lingwood and S. Han, "Solution-state dynamic nuclear polarization," *Annu. Rep. NMR Spectrosc.*, vol. 73, pp. 83–126, 2011.

[39] U. L. Günther, "Dynamic nuclear hyperpolarization in liquids," *Top. Curr. Chem.*, vol. 335, pp. 23–69, 2013.

[40] M. D. Lingwood and S. Han, "Dynamic nuclear polarization of $^{13}$C in aqueous solutions under ambient conditions," *J. Magn. Reson.*, vol. 201, pp. 137–145, 2009.

[41] A. Abrgam and M. Goldman, "Principles of dynamic nuclear polarisation," *Rep. Prog. Phys.*, vol. 41, pp. 395–467, 1978.

[42] J. R. B. John A. Weil, *Electron Paramagnetic Resonance: Elementary Theory and Practical Applications*, 2nd ed. Hoboken: Wiley, 2006.

[43] K.-N. Hu, H.-h. Yu, T. M. Swager, and R. G. Griffin, "Dynamic nuclear polarization with biradicals," *J. Am. Chem. Soc.*, vol. 126, pp. 10 844–10 845, 2004.

[44] T. Maly, G. T. Debelouchina, V. S. Bajaj, K.-N. Hu, C.-G. Joo, M. L. MakJurkauskas, J. R. Sirigiri, P. C. A. v. d. Wel, J. Herzfeld, R. J. Temkin, and R. G. Griffin, "Dynamic nuclear polarization at high magnetic fields," *J. Chem. Phys.*, vol. 128, p. 052211, 2008.

[45] L. Lumata, S. J. Ratnakar, A. Jindal, M. Merritt, A. Comment, C. Malloy, A. D. Sherry, and Z. Kovacs, "BDPA: An efficient polarizing agent for fast dissolution dynamic nuclear polarization NMR spectroscopy," *Chem. Eur. J.*, vol. 17, pp. 10 825–10 827, 2011.

[46] C. Ludwig, I. Marin-Montesinos, M. G. Saunders, and U. L. Günther, "Optimizing the polarization matrix for ex situ dynamic nuclear polarization," *J. Am. Chem. Soc.*, vol. 132, pp. 2508–2509, 2010.

[47] L. Lumata, M. E. Merritt, C. R. Malloy, A. D. Sherry, and Z. Kovacs, "The impact of $Gd^{3+}$ on DNP of [1-$^{13}$C]pyruvate doped with trityl OX63, BDPA, or 4-Oxo-TEMPO," *J. Phys. Chem. A*, vol. 116, pp. 5129–5138, 2012.

[48] L. Lumata, M. E. Merritt, and Z. Kovacs, "Influence of deuteration in the glassing matrix on $^{13}$C dynamic nuclear polarization," *Phys. Chem. Chem. Phys.*, vol. 15, pp. 7032–7035, 2013.

[49] C. Song, K.-N. Hu, C.-G. Joo, T. M. Swager, and R. G. Griffin, "Totapol: A biradical polarizing agent for dynamic nuclear polarization experiments in aqueous media," *J. Am. Chem. Soc.*, vol. 128, no. 35, pp. 11 385–11 390, 2006.

[50] M. Rosay, J. C. Lansing, K. C. Haddad, W. W. Bachovchin, J. Herzfeld, R. J. Temkin, and R. G. Griffin, "High-frequency dynamic nuclear polarization in MAS spectra of membrane and soluble proteins," *J. Am. Chem. Soc.*, vol. 125, pp. 13 626–13 627, 2003.

[51] D. A. Hall, D. C. Maus, G. J. Gerfen, S. J. Inati, L. R. Becerra, F. W. Dahlquist, and R. G. Griffin, "Polarization-enhanced nmr spectroscopy of biomolecules in frozen solution," *Science*, vol. 276, pp. 930–932, 1997.

[52] P. C. A. van der Wel, K.-N. Hu, J. Lewandowski, and R. G. Griffin, "Dynamic nuclear polarization of amyloidogenic peptide nanocrystals: GNNQQNY, a core segment of the yeast prion protein Sup35p," *J. Am. Chem. Soc.*, vol. 128, pp. 10 840–10 846, 2006.

[53] A. Barnes, G. D. Paepe, P. van der Wel, K.-N. Hu, C.-G. Joo, V. Bajaj, M. Mak-Jurkauskas, J. Sirigiri, J. Herzfeld, R. Temkin, and R. Griffin, "High-field dynamic nuclear polarization for solid and solution biological NMR," *Appl. Magn. Reson.*, vol. 34, pp. 237–263, 2008.

[54] M. D. Lingwood, T. A. Siaw, N. Sailasuta, O. A. Abulseoud, H. R. Chan, B. D. Ross, P. Bhattacharya, and S. Han, "Hyperpolarized water as an MR imaging contrast agent: Feasibility of in vivo imaging in a rat model," *Radiology*, vol. 265, pp. 418–425, 2012.

[55] B. D. Armstrong, J. Choi, C. López, D. A. Wesener, W. Hubbell, S. Cavagnero, and S. Han, "Site-specific hydration dynamics in the nonpolar core of a molten globule by dynamic nuclear polarization of water," *J. Am. Chem. Soc.*, vol. 133, pp. 5987–5995, 2011.

[56] V. Weis, M. Bennati, M. Rosay, J. A. Bryant, and R. G. Griffin, "High-field DNP and ENDOR with a novel multiple-frequency resonance structure," *J. Magn. Reson.*, vol. 140, pp. 293–299, 1999.

[57] V. Denysenkov and T. Prisner, "Liquid state dynamic nuclear polarization probe with Fabry-Perot resonator at 9.2 T," *J. Magn. Reson.*, vol. 217, pp. 1–5, 2012.

[58] J. H. Ardenkjær-Larsen, B. Fridlund, A. Gram, G. Hansson, L. Hansson, M. H. Lerche, R. Servin, M. Thaning, and K. Golman, "Increase in signal-to-noise ratio of >10,000 times in liquid-state NMR," *Proc. Natl. Acad. Sci. U. S. A.*, vol. 100, pp. 10 158–10 163, 2003.

[59] W. Köckenberger, "Dissolution dynamic nuclear polarization," in *eMagRes*. Hoboken: John Wiley & Sons, 2014, vol. 3, pp. 161–170.

[60] J. W. Gordon, S. B. Fain, and I. J. Rowland, "Effect of lanthanide ions on dynamic nuclear polarization enhancement and liquid-state T1 relaxation," *Magn. Reson. Med.*, vol. 68, pp. 1949–1954, 2012.

[61] S. Jannin, A. Bornet, S. Colombo, and G. Bodenhausen, "Low-temperature cross polarization in view of enhancing dissolution dynamic nuclear polarization in

NMR," *Chem. Phys. Lett.*, vol. 517, pp. 234–236, 2011.

[62] M. Batel, A. Däpp, A. Hunkeler, B. H. Meier, S. Kozerke, and M. Ernst, "Cross-polarization for dissolution dynamic nuclear polarization," *Phys. Chem. Chem. Phys.*, vol. 16, pp. 21 407–21 416, 2014.

[63] S. Bowen and C. Hilty, "Rapid sample injection for hyperpolarized NMR spectroscopy," *Phys. Chem. Chem. Phys.*, vol. 12, pp. 5766–5770, 2010.

[64] J. Leggett, R. Hunter, J. Granwehr, R. Panek, A. J. Perez-Linde, A. J. Horsewill, J. McMaster, G. Smith, and W. Köckenberger, "A dedicated spectrometer for dissolution DNP NMR spectroscopy," *Phys. Chem. Chem. Phys.*, vol. 12, pp. 5883–5892, 2010.

[65] M. Ragavan, H.-Y. Chen, G. Sekar, and C. Hilty, "Solution NMR of polypeptides hyperpolarized by dynamic nuclear polarization," *Anal. Chem.*, vol. 83, pp. 6054–6059, 2011.

[66] J. Svensson, S. Månsson, E. Johansson, J. S. Petersson, and L. E. Olsson, "Hyperpolarized $^{13}$C MR angiography using trueFISP," *Magn. Reson. Med.*, vol. 50, pp. 256–262, 2003.

[67] T. Harris, O. Szekely, and L. Frydman, "On the potential of hyperpolarized water in biomolecular NMR studies," *J. Phys. Chem. B*, vol. 118, pp. 3281–3290, 2014.

[68] K. Jozef and M. Lena, *Nuclear spin relaxation in liquids: Theory, Experiments, and Applications, 1st edition*. Boca Raton: CRC Press, 2006.

[69] P. Miéville, S. Jannin, and G. Bodenhausen, "Relaxometry of insensitive nuclei: Optimizing dissolution dynamic nuclear polarization," *J. Magn. Reson.*, vol. 210, pp. 137–140, 2011.

[70] J. Granwehr, R. Panek, J. Leggett, and W. Köckenberger, "Quantifying the transfer and settling in NMR experiments with sample shuttling," *J. Chem. Phys.*, vol. 132, pp. 244 507–244 513, 2010.

[71] H.-Y. Chen, M. Ragavan, and C. Hilty, "Protein folding studied by dissolution dynamic nuclear polarization," *Angew. Chem. Int. Ed*, vol. 52, pp. 9192–9195, 2013.

[72] H.-Y. Chen and C. Hilty, "Hyperpolarized Hadamard spectroscopy using Flow NMR," *Anal. Chem.*, vol. 85, pp. 7385–7390, 2013.

[73] C. G. Joo, A. Casey, C. J. Turner, and R. G. Griffin, "In situ temperature-jump dynamic nuclear polarization: Enhanced sensitivity in two dimensional $^{13}$C-$^{13}$C correlation spectroscopy in solution," *J. Am. Chem. Soc.*, vol. 131, pp. 12–13, 2009.

[74] P. Miéville, P. Ahuja, R. Sarkar, S. Jannin, P. Vasos, S. Gerber-Lemaire, M. Mishkovsky, A. Comment, R. Gruetter, O. Ouari, P. Tordo, and G. Bodenhausen, "Scavenging free radicals to preserve enhancement and extend relaxation times in NMR using dynamic nuclear polarization," *Angew. Chem. Int. Ed.*, vol. 49, pp. 6182–6185, 2010.

[75] V. Krishnan and N. Murali, "Radiation damping in modern NMR experiments: Progress and challenges," *Prog. Nucl. Magn. Reson. Spectrosc.*, vol. 68, pp. 41 – 57, 2013.

[76] D. J.-Y. Marion, G. Huber, P. Berthault, and H. Desvaux, "Observation of noise-triggered chaotic emissions in an NMR-Maser," *ChemPhysChem*, pp. 1395–1401, 2008.

[77] H. Y. Chen, Y. Lee, S. Bowen, and C. Hilty, "Spontaneous emission of NMR signals in hyperpolarized proton spin systems," *J. Magn. Reson.*, vol. 208, pp. 204–209, 2011.

[78] C. Xiao-Hong, P. Ling, Z. Zhen-Min, C. Shu-Hui, and C. Zhong, "A new solvent suppression method via radiation damping effect," *Chin. Phys. Lett.*, vol. 20, p. 118201, 2011.

[79] M. Goldman, "Overview of spin temperature, themmal mixing and dynamic nuclear polarization," *Appl. Magn. Reson.*, vol. 34, pp. 219–226, 2008.

[80] Y. Lee, G. Heo, H. Zeng, K. Wooley, and C. Hilty, "Detection of living anionic species in polymerization reaction using hyperpolarized NMR," *J. Am. Chem. Soc.*, vol. 135, pp. 4636–4639, 2013.

[81] H. Zeng, S. Bowen, and C. Hilty, "Sequentially acquired two-dimensional NMR spectra from hyperpolarized sample," *J. Magn. Reson.*, vol. 199, pp. 159–165, 2009.

[82] G. S. Rule and T. K. Hitchens, *Fundamentals of Protein NMR Spectroscopy*. New York City: Springer, 2006.

[83] S. Bowen, H. Zeng, and C. Hilty, "Chemical shift correlations from hyperpolarized NMR by off-resonance decoupling," *Anal. Chem.*, vol. 80, pp. 5794–5798, 2008.

[84] G. Zhang, F. Schilling, S. J. Glaser, and C. Hilty, "Chemical shift correlations from hyperpolarized NMR using a single SHOT," *Anal. Chem.*, vol. 85, pp. 2875–2881, 2013.

[85] L. Frydman and D. Blazina, "Ultrafast two-dimensional nuclear magnetic resonance spectroscopy of hyperpolarized solutions," *Nat. Phys.*, vol. 3, pp. 415–419, 2007.

[86] P. Pelupessy, "Adiabatic single-scan two-dimensional NMR spectroscopy," *J. Am. Chem. Soc.*, vol. 125, pp. 12 345–12 350, 2003.

[87] A. Tal and L. Frydman, "Single-scan multidimensional magnetic resonance," *Prog. Nucl. Magn. Reson. Spectrosc.*, vol. 57, pp. 241–292, 2010.

[88] Ēriks Kupče and R. Freeman, "Two-dimensional Hadamard spectroscopy," *J. Magn. Reson.*, vol. 162, pp. 300 – 310, 2003.

[89] A. Tal, B. Shapira, and L. Frydman, "Single-scan 2D Hadamard NMR spectroscopy," *Angew. Chem. Int. Ed.*, vol. 48, pp. 2732–2736, 2009.

[90] K. R. Keshari and D. M. Wilson, "Chemistry and biochemistry of $^{13}$C hyperpolarized magnetic resonance using dynamic nuclear polarization," *Chem. Soc. Rev.*, vol. 43, pp. 1627–1659, 2014.

[91] K. Golman, J. H. Ardenkjær-Larsen, J. S. Petersson, S. Månsson, and I. Leunbach, "Molecular imaging with endogenous substances," *Proc. Natl. Acad. Sci. U. S. A.*, vol. 100, pp. 10 435–10 439, 2003.

[92] Y.-F. Yen, K. Nagasawa, and T. Nakada, "Promising application of dynamic nuclear polarization for *in vivo* $^{13}$C MR imaging," *Magn. Reson. Med. Sci.*, vol. 10, pp. 211–217, 2011.

[93] K. R. Keshari, D. M. Wilson, A. P. Chen, R. Bok, P. E. Z. Larson, S. Hu, M. V. Criekinge, J. M. Macdonald, D. B. Vigneron, and J. Kurhanewicz, "Hyperpolarized [2-$^{13}$C]-fructose: A hemiketal DNP substrate for *in vivo* metabolic imaging," *J. Am. Chem. Soc.*, vol. 131, pp. 17 591–17 596, 2009.

[94] D. R. Ball, B. Rowlands, M. S. Dodd, L. Le Page, V. Ball, C. A. Carr, K. Clarke, and D. J. Tyler, "Hyperpolarized butyrate: A metabolic probe of short chain fatty acid metabolism in the heart," *Magn. Reson. Med.*, vol. 71, pp. 1663–1669, 2014.

[95] K. R. Keshari, J. Kurhanewicz, R. E. Jeffries, D. M. Wilson, B. J. Dewar, M. Van Criekinge, M. Zierhut, D. B. Vigneron, and J. M. Macdonald, "Hyperpolarized $^{13}$C spectroscopy and an NMR-compatible bioreactor system for the investi-

gation of real-time cellular metabolism," *Magn. Reson. Med.*, vol. 63, pp. 322–329, 2010.

[96] R. E. Hurd, Y.-F. Yen, J. Tropp, A. Pfefferbaum, D. M. Spielman, and D. Mayer, "Cerebral dynamics and metabolism of hyperpolarized [1-$^{13}$C]pyruvate using time-resolved MR spectroscopic imaging," *J. Cereb. Blood Flow Metab.*, vol. 30, pp. 1734–1741, 2010.

[97] S. J. Nelson, D. Vigneron, J. Kurhanewicz, A. Chen, R. Bok, and R. Hurd, "DNP-hyperpolarized $^{13}$C magnetic resonance metabolic imaging for cancer applications," *Appl. Magn. Reson.*, vol. 34, pp. 533–544, 2008.

[98] K. Brindle, "New approaches for imaging tumour responses to treatment," *Nat. Rev. Cancer*, vol. 8, pp. 94–107, 2008.

[99] I. Park, P. E. Z. Larson, M. L. Zierhut, S. Hu, R. Bok, T. Ozawa, J. Kurhanewicz, D. B. Vigneron, S. R. Vandenberg, C. D. James, and S. J. Nelson, "Hyperpolarized $^{13}$C magnetic resonance metabolic imaging: Application to brain tumors," *Neuro-Oncology*, vol. 12, pp. 133–144, 2010.

[100] J. H. Ardenkjær-Larsen, A. M. Leach, N. Clarke, J. Urbahn, D. Anderson, and T. W. Skloss, "Dynamic nuclear polarization polarizer for sterile use intent," *NMR Biomed.*, vol. 24, pp. 927–932, 2011.

[101] F. A. Gallagher, M. I. Kettunen, S. E. Day, D.-E. Hu, J. H. Ardenkjær-Larsen, R. i. t. Zandt, P. R. Jensen, M. Karlsson, K. Golman, M. H. Lerche, and K. M. Brindle, "Magnetic resonance imaging of pH *in vivo* using hyperpolarized $^{13}$c-labelled bicarbonate," *Nature*, vol. 453, pp. 940–943, 2008.

[102] T. Harris, H. Degani, and L. Frydman, "Hyperpolarized 13c NMR studies of glucose metabolism in living breast cancer cell cultures," *NMR in biomedicine*, vol. 26, pp.

1831–1843, 2013.

[103] S. J. Nelson, J. Kurhanewicz, D. B. Vigneron, P. E. Z. Larson, A. L. Harzstark, M. Ferrone, M. v. Criekinge, J. W. Chang, R. Bok, I. Park, G. Reed, L. Carvajal, E. J. Small, P. Munster, V. K. Weinberg, J. H. Ardenkjaer-Larsen, A. P. Chen, R. E. Hurd, L.-I. Odegardstuen, F. J. Robb, J. Tropp, and J. A. Murray, "Metabolic imaging of patients with prostate cancer using hyperpolarized [1-$^{13}$C]pyruvate," *Sci. Transl. Med.*, vol. 5, pp. 198ra108(1–11), 2013.

[104] K. R. Keshari, J. Kurhanewicz, R. Bok, P. E. Z. Larson, D. B. Vigneron, and D. M. Wilson, "Hyperpolarized $^{13}$C dehydroascorbate as an endogenous redox sensor for in vivo metabolic imaging," *Proc. Natl. Acad. Sci. USA*, vol. 108, pp. 18 606–18 611, 2011.

[105] S. Bowen and C. Hilty, "Time-resolved dynamic nuclear polarization enhanced NMR spectroscopy," *Angew. Chem. Int. Ed.*, vol. 47, pp. 5235–5237, 2008.

[106] E. Miclet, D. Abergel, A. Bornet, J. Milani, S. Jannin, and G. Bodenhausen, "Toward quantitative measurements of enzyme kinetics by dissolution dynamic nuclear polarization," *J. Phys. Chem. Lett.*, vol. 5, pp. 3290–3295, 2014.

[107] C. Gabellieri, S. Reynolds, A. Lavie, G. S. Payne, M. O. Leach, and T. R. Eykyn, "Therapeutic target metabolism observed using hyperpolarized $^{15}$N choline," *J. Am. Chem. Soc.*, vol. 130, pp. 4598–4599, 2008.

[108] K. R. Keshari, J. Kurhanewicz, J. M. Macdonald, and D. M. Wilson, "Generating contrast in hyperpolarized $^{13}$ C MRI using ligand–receptor interactions," *Analyst*, vol. 137, pp. 3427–3429, 2012.

[109] Y. Lee, H. Zeng, S. Ruedisser, A. D. Gossert, and C. Hilty, "Nuclear magnetic resonance of hyperpolarized fluorine for characterization of protein–ligand interac-

tions," *J. Am. Chem. Soc.*, vol. 134, pp. 17 448–17 451, 2012.

[110] Y. Kim and C. Hilty, "Affinity screening using competitive binding with fluorine-19 hyperpolarized ligands," *Angew. Chem. Int. Ed*, pp. 4941–4944, 2015.

[111] V. M. Sánchez-Pedregal, M. Reese, J. Meiler, M. J. J. Blommers, C. Griesinger, and T. Carlomagno, "The INPHARMA method: protein-mediated interligand NOEs for pharmacophore mapping," *Angew. Chem. Int. Ed*, vol. 44, pp. 4172–4175, 2005.

[112] Y. Lee, H. Zeng, A. Mazur, M. Wegstroth, T. Carlomagno, M. Reese, D. Lee, S. Becker, C. Griesinger, and C. Hilty, "Hyperpolarized binding pocket nuclear overhauser effect for determination of competitive ligand binding," *Angew. Chem. Int. Ed.*, vol. 51, pp. 5179–82, 2012.

[113] T. Sleator, E. L. Hahn, C. Hilbert, and J. Clarke, "Nuclear-spin noise," *Phys. Rev. Lett.*, vol. 55, pp. 1742–1745, 1985.

[114] T. Sleator, C. Hilbert, E. L. Hahn, and J. Clarke, "Nuclear-spin noise and spontaneous emission," *Phys. Rev. B*, vol. 36, pp. 1969–1980, 1987.

[115] M. A. McCoy and R. R. Ernst, "Nuclear spin noise at room temperature," *Chem. Phys. Lett.*, vol. 159, pp. 587–593, 1989.

[116] H. Desvaux, D. J. Y. Marion, G. Huber, and P. Berthault, "Nuclear spin-noise spectra of hyperpolarized systems," *Angew. Chem. Int. Ed.*, vol. 121, pp. 4405–4407, 2009.

[117] P. Giraudeau, N. Müller, A. Jerschow, and L. Frydman, "$^{1}$H NMR noise measurements in hyperpolarized liquid samples," *Chem. Phys. Lett.*, vol. 489, pp. 107–112, 2010.

[118] D. J. Y. Marion, G. Huber, P. Berthault, and H. Desvaux, "Observation of noise-triggered chaotic emissions in an nmr-maser," *ChemPhysChem*, vol. 9, pp. 1395–1401, 2008.

[119] I. J. Day, J. C. Mitchell, M. J. Snowden, and A. L. Davis, "Applications of DNP-NMR for the measurement of heteronuclear $T_1$ relaxation times," *J. Magn. Reson.*, vol. 187, pp. 216–224, 2007.

[120] J. H. Chen, B. Cutting, and G. Bodenhausen, "Measurement of radiation damping rate constants in nuclear magnetic resonance by inversion recovery and automated compensation of selective pulses," *J. Chem. Phys.*, vol. 112, pp. 6511–6514, 2000.

[121] R. A. Wind, M. J. Duijvestijn, C. van der Lugt, A. Manenschijn, and J. Vriend, "Applications of dynamic nuclear-polarization in $^{13}$C NMR in solids," *Prog. Nucl. Magn. Reson. Spectrosc.*, vol. 17, pp. 33–67, 1985.

[122] X. A. Mao, D. H. Wu, and C. H. Ye, "Radiation damping effects on NMR signal intensities," *Chem. Phys. Lett.*, vol. 204, pp. 123–127, 1993.

[123] W. S. Warren, S. L. Hammes, and J. L. Bates, "Dynamics of radiation damping in nuclear magnetic resonance," *J. Chem. Phys.*, vol. 91, pp. 5895–5904, 1989.

[124] D. J. Y. Marion, P. Berthault, and H. Desvaux, "Spectral and temporal features of multiple spontaneous NMR-Maser emissions," *Eur. Phys. J. D*, vol. 51, pp. 357–367, 2009.

[125] M. G. Richards, B. P. Cowan, M. F. Secca, and K. Machin, "The $^3$He nuclear Zeeman maser," *J. Phys. B: At., Mol. Opt. Phys.*, vol. 21, pp. 665–681, 1988.

[126] M. G. Saunders, C. Ludwig, and U. L. Günther, "Optimizing the signal enhancement in cryogenic *ex-situ* DNP-NMR spectroscopy," *J. Am. Chem. Soc.*, vol. 130, pp. 6914–6915, 2008.

[127] K. W. Plaxco and C. M. Dobson, "Time-resolved biophysical methods in the study of protein folding," *Curr. Opin. Struct. Biol.*, vol. 6, pp. 630–636, 1996.

[128] J. Balbach, C. Steegborn, T. Schindler, and F. X. Schmid, "A protein folding intermediate of ribonuclease T1 characterized at high resolution by 1D and 2D real-time NMR spectroscopy," *J. Mol. Biol.*, vol. 285, pp. 829–842, 1999.

[129] C. Frieden, S. D. Hoeltzli, and I. J. Ropson, "NMR and protein folding: Equilibrium and stopped-flow studies," *Protein Sci.*, vol. 2, pp. 2007–2014, 1993.

[130] S. D. Hoeltzli and C. Frieden, "Real-time refolding studies of 6-$^{19}$F-tryptophan labeled *Escherichia coli* dihydrofolate reductase using stopped-flow NMR spectroscopy," *Biochemistry*, vol. 35, pp. 16 843–16 851, 1996.

[131] P. Schanda, V. Forge, and B. Brutscher, "Protein folding and unfolding studied at atomic resolution by fast two-dimensional NMR spectroscopy," *Proc. Natl. Acad. Sci. U. S. A.*, vol. 104, pp. 11 257–11 262, 2007.

[132] H. Zeng, Y. Lee, and C. Hilty, "Quantitative rate determination by dynamic nuclear polarization enhanced NMR of a Diels-Alder reaction," *Anal. Chem.*, vol. 82, pp. 8897–8902, 2010.

[133] C. M. Dobson and P. J. Hore, "Kinetic studies of protein folding using NMR spectroscopy," *Nat. Struct. Biol.*, vol. 5, pp. 504–507, 1998.

[134] A. Öhman, A. Rak, M. Dontsova, M. B. Garber, and T. Härd, "NMR structure of the ribosomal protein L23 from *Thermus thermophilus*," *J. Biomol. NMR*, vol. 26, pp. 131–137, 2003.

[135] K. L. Maxwell, D. Wildes, A. Zarrine-Afsar, M. A. De Los Rios, A. G. Brown, C. T. Friel, L. Hedberg, J.-C. Horng, D. Bona, E. J. Miller, A. Vallée-Blisle, E. R. Main, F. Bemporad, L. Qiu, K. Teilum, N.-D. Vu, A. M. Edwards, I. Ruczinski, F. M.

Poulsen, B. B. Kragelund, S. W. Michnick, F. Chiti, Y. Bai, S. J. Hagen, L. Serrano, M. Oliveberg, D. P. Raleigh, P. Wittung-Stafshede, S. E. Radford, S. E. Jackson, T. R. Sosnick, S. Marqusee, A. R. Davidson, and K. W. Plaxco, "Protein folding: Defining a standard set of experimental conditions and a preliminary kinetic data set of two-state proteins," *Protein Sci.*, vol. 14, pp. 602–616, 2005.

[136] H. Zhang, S. Neal, and D. S. Wishart, "RefDB: a database of uniformly referenced protein chemical shifts," *J. Biomol. NMR*, vol. 25, pp. 173–195, 2003.

[137] R. J. Robbins, G. R. Fleming, G. S. Beddard, G. W. Robinson, P. J. Thistlethwaite, and G. J. Woolfe, "Photophysics of aqueous tryptophan: pH and temperature effects," *J. Am. Chem. Soc.*, vol. 102, pp. 6271–6279, 1980.

[138] B. A. Krantz, L. B. Moran, A. Kentsis, and T. R. Sosnick, "D/H amide kinetic isotope effects reveal when hydrogen bonds form during protein folding," *Nat. Struct. Biol.*, vol. 7, pp. 62–71, 2000.

[139] H.-Y. Chen, Y. Lee, S. Bowen, and C. Hilty, "Spontaneous emission of NMR signals in hyperpolarized proton spin systems," *J. Magn. Reson.*, vol. 208, pp. 204 – 209, 2011.

[140] R. Kühne, T. Schaffhauser, A. Wokaun, and R. Ernst, "Study of transient chemical reactions by NMR. fast stopped-flow Fourier transform experiments," *J. Magn. Reson.*, vol. 35, pp. 39 – 67, 1979.

[141] J. Cavanagh, W. J. Fairbrother, A. G. Palmer, M. Rance, and N. J. Skelton, *Protein NMR Spectroscopy: Principles and Practice, 2$^{nd}$ Ed.* Waltham: Elsevier Academic Press, 2007.

[142] K. Maki, K. Kamagata, and K. Kuwajima, *Equilibrium and Kinetically Observed Molten Globule States*, J. Buchner and T. Kiefhaber, Eds. Weinheim: Wiley-VCH

Verlag GmbH, 2008.

[143] S. Bowen and C. Hilty, "Temporal chemical shift correlations in reactions studied by hyperpolarized nuclear magnetic resonance," *Anal. Chem.*, vol. 81, pp. 4543–4547, 2009.

[144] V. Tugarinov, V. Kanelis, and L. E. Kay, "Isotope labeling strategies for the study of high-molecular-weight proteins by solution NMR spectroscopy," *Nat. Protoc.*, vol. 1, pp. 749–754, 2006.

[145] A. Eletsky, O. Moreira, H. Kovacs, and K. Pervushin, "A novel strategy for the assignment of side-chain resonances in completely deuterated large proteins using $^{13}$C spectroscopy," *J. Biomol. NMR*, vol. 26, pp. 167–179, 2003.

[146] K. Golman, J. H. Ardenkjær-Larsen, J. S. Petersson, S. Månsson, and I. Leunbach, "Molecular imaging with endogenous substances," *Proc. Natl. Acad. Sci. U. S. A.*, vol. 100, pp. 10 435–10 439, 2003.

[147] R. Sarkar, A. Comment, P. R. Vasos, S. Jannin, R. Gruetter, G. Bodenhausen, H. Hall, D. Kirik, and V. P. Denisov, "Proton NMR of $^{15}$N-choline metabolites enhanced by dynamic nuclear polarization," *J. Am. Chem. Soc.*, vol. 131, pp. 16 014–16 015, 2009.

[148] P. Giraudeau, Y. Shrot, and L. Frydman, "Multiple ultrafast, broadband 2D NMR spectra of hyperpolarized natural products," *J. Am. Chem. Soc.*, vol. 131, pp. 13 902–13 903, 2009.

[149] S. E. Bohndiek, M. I. Kettunen, D. en Hu, B. W. C. Kennedy, J. Boren, F. A. Gallagher, and K. M. Brindle, "Hyperpolarized [1-$^{13}$C]-ascorbic and dehydroascorbic acid: Vitamin C as a probe for imaging redox status in vivo," *J. Am. Chem. Soc.*, vol. 133, pp. 11 795–11 801, 2011.

[150] Ēriks Kupče, T. Nishida, and R. Freeman, "Hadamard NMR spectroscopy," *Prog. Nucl. Mag. Res. Sp.*, vol. 42, pp. 95–122, 2003.

[151] C. A. Steinbeck and B. F. Chmelka, "Rapid $^{1}$H-$^{13}$C-resolved diffusion and spin-relaxation measurements by NMR spectroscopy," *J. Am. Chem. Soc.*, vol. 127, pp. 11 624–11 635, 2005.

[152] S. L. Patt, "Single- and multiple- frequency-shifted Laminar pulses," *J. Magn. Reson.*, vol. 96, pp. 94–102, 1992.

[153] A. J. Shaka and J. Keeler, "Broadband spin decoupling in isotropic-liquids," *Prog. Nucl. Mag. Res. Sp.*, vol. 19, pp. 47–129, 1987.

[154] L. Chen, Z. Weng, L. Goh, and M. Garland, "An efficient algorithm for automatic phase correction of NMR spectra based on entropy minimization," *J. Magn. Reson.*, vol. 158, pp. 164–168, 2002.

[155] S. Meier, P. R. Jensen, M. Karlsson, and M. H. Lerche, "Hyperpolarized NMR probes for biological assays," *Sensors*, vol. 14, pp. 1576–1597, 2014.

[156] J. H. Ardenkjær-Larsen, B. Fridlund, A. Gram, G. Hansson, L. Hansson, M. H. Lerche, R. Servin, M. Thaning, and K. Golman, "Increase in signal-to-noise ratio of > 10,000 times in liquid-state NMR," *Proc. Natl. Acad. Sci. U. S. A.*, vol. 100, pp. 10 158–10 163, 2003.

[157] A. Bornet, R. Melzi, A. J. Perez Linde, P. Hautle, B. van den Brandt, S. Jannin, and G. Bodenhausen, "Boosting dissolution dynamic nuclear polarization by cross polarization," *J. Phys. Chem. Lett.*, vol. 4, pp. 111–114, 2012.

[158] I. V. Koptyug, "Spin hyperpolarization in NMR to address enzymatic processes *in vivo*," *Mendeleev Commun.*, vol. 23, pp. 299–312, 2013.

[159] T. Cheng, M. Mishkovsky, J. A. M. Bastiaansen, O. Ouari, P. Hautle, P. Tordo, B. van den Brandt, and A. Comment, "Automated transfer and injection of hyperpolarized molecules with polarization measurement prior to *in vivo* NMR," *NMR Biomed.*, pp. 1582–1588, 2013.

[160] S. Reynolds, A. Bucur, M. Port, T. Alizadeh, S. M. Kazan, G. M. Tozer, and M. N. J. Paley, "A system for accurate and automated injection of hyperpolarized substrate with minimal dead time and scalable volumes over a large range," *J. Magn. Reson.*, vol. 239, pp. 1–8, 2014.

[161] S. Hu, P. E. Z. Larson, M. Vancriekinge, A. M. Leach, I. Park, C. Leon, J. Zhou, P. J. Shin, G. Reed, P. Keselman, and e. al, "Rapid sequential injections of hyperpolarized [1-$^{13}$C] pyruvate in vivo using a sub-kelvin, multi-sample DNP polarizer," *Magn. Reson. Imaging.*, vol. 31, pp. 490–496, 2013.

[162] J. H. Ardenkjær-Larsen, A. M. Leach, N. Clarke, J. Urbahn, D. Anderson, and T. W. Skloss, "Dynamic nuclear polarization polarizer for sterile use intent," *NMR Biomed.*, vol. 24, pp. 927–932, 2011.

[163] S. Bowen and C. Hilty, "Rapid sample injection for hyperpolarized NMR spectroscopy," *Phys. Chem. Chem. Phys.*, vol. 12, pp. 5766–5770, 2010.

[164] Y. Lee, H. Zeng, S. Ruedisser, A. D. Gossert, and C. Hilty, "Nuclear magnetic resonance of hyperpolarized fluorine for characterization of proteinligand interactions," *J. Am. Chem. Soc.*, vol. 134, pp. 17 448–17 451, 2012.

[165] C. Ludwig, I. Marin-Montesinos, M. G. Saunders, A.-H. Emwas, Z. Pikramenou, S. P. Hammond, and U. L. Günther, "Application of *ex situ* dynamic nuclear polarization in studying small molecules," *Phys. Chem. Chem. Phys.*, vol. 12, pp. 5868–5871, 2010.

[166] K. J. Donovan and L. Frydman, "HyperSPASM NMR: A new approach to single-shot 2D correlations on DNP enhanced samples," *J. Magn. Reson.*, vol. 225, pp. 115 – 119, 2012.

[167] S. Bowen, H. Zeng, and C. Hilty, "Chemical shift correlations from hyperpolarized NMR by off-resonance decoupling," *Anal. Chem.*, vol. 80, pp. 5794–5798, 2008.

[168] L. Frydman and D. Blazina, "Ultrafast two-dimensional nuclear magnetic resonance spectroscopy of hyperpolarized solutions," *Nat. Phys.*, vol. 3, pp. 415–419, 2007.

[169] J. Leggett, R. Hunter, J. Granwehr, R. Panek, A. J. Perez-Linde, A. J. Horsewill, J. McMaster, G. Smith, and W. Köckenberge, "A dedicated spectrometer for dissolution DNP NMR spectroscopy," *Phys. Chem. Chem. Phys.*, vol. 12, pp. 5883–5892, 2010.

[170] H.-Y. Chen and C. Hilty, "Hyperpolarized Hadamard spectroscopy using flow NMR," *Anal. Chem.*, vol. 85, pp. 7385–7390, 2013.

[171] S. Peled, C.-H. Tseng, A. A. Sodickson, R. W. Mair, R. L. Walsworth, and D. G. Cory, "Single-shot diffusion measurement in laser-polarized gas," *J. Magn. Reson.*, vol. 140, pp. 320–324, 1999.

[172] P. Callaghan, *Translational Dynamics and Magnetic Resonance: Principles of Pulsed Gradient Spin Echo NMR*. Oxford: Oxford University Press, 2011.

[173] Y. Shrot and L. Frydman, "The effects of molecular diffusion in ultrafast two-dimensional nuclear magnetic resonance," *J. Chem. Phys.*, vol. 128, pp. 164 513(1)–164 513(15), 2008.

[174] G. Zhang, F. Schilling, S. J. Glaser, and C. Hilty, "Chemical shift correlations from hyperpolarized NMR using a single SHOT," *Anal. Chem.*, vol. 85, pp. 2875–2881, 2013.

[175] P. S. Belton, A. M. Gil, G. A. Webb, and D. Rutledge, Eds., *Magnetic Resonance in Food Science*. Cambridge: Royal Society of Chemistry, 2003.

[176] E. Veliyulin, C. van der Zwaag, W. Burk, and U. Erikson, "*In vivo* determination of fat content in Atlantic salmon (Salmo salar) with a mobile NMR spectrometer," *J. Sci. Food Agric.*, vol. 85, pp. 1299–1304, 2005.

[177] H. T. Pedersen, S. Ablett, D. R. Martin, M. J. D. Mallett, and S. B. Engelsen, "Application of the NMR-MOUSE to food emulsions," *J. Magn. Reson.*, vol. 165, pp. 49–58, 2003.

[178] A. Guthausen, G. Guthausen, A. Kamlowski, H. Todt, W. Burk, and D. Schmalbein, "Measurement of fat content of food with single-sided NMR," *J. Am. Oil Chem. Soc.*, vol. 81, pp. 727–731, 2004.

[179] R. Lu, X. Zhou, W. Wu, Y. Zhang, and Z. Ni, "Development of the miniature NMR apparatus for edible oil quality control," *Appl. Magn. Reson.*, vol. 45, pp. 461–469, 2014.

[180] G. Eidmann, R. Savelsberg, P. Blmler, and B. Blmich, "The NMR MOUSE, a mobile universal surface explorer," *J. Magn. Reson., Ser. A*, vol. 122, pp. 104–109, 1996.

[181] A. Legchenko, J.-M. Baltassat, A. Beauce, and J. Bernard, "Nuclear magnetic resonance as a geophysical tool for hydrogeologists," *J. Appl. Geophys.*, vol. 50, pp. 21–46, 2002.

[182] H. Lee, E. Sun, D. Ham, and R. Weissleder, "ChipNMR biosensor for detection and molecular analysis of cells," *Nature Med.*, vol. 14, pp. 869–874, 2008.

[183] P. T. Callaghan, A. Coy, R. Dykstra, C. D. Eccles, M. E. Halse, M. W. Hunter, O. R. Mercier, and J. N. Robinson, "New zealand developments in earths field NMR,"

*Appl. Magn. Reson.*, vol. 32, pp. 63–74, 2007.

[184] C. Hilty and S. Bowen, "An NMR experiment based on off-the-shelf digital data-acquisition equipment," *J. Chem. Educ.*, vol. 87, pp. 747–749, 2010.

[185] M. F. Isaac-Lam, "Analysis of bromination of ethylbenzene using a 45 MHz NMR spectrometer: An undergraduate organic chemistry laboratory experiment," *J. Chem. Educ.*, vol. 91, pp. 1264–1266, 2014.

[186] G. A. Lorigan, R. E. Minto, and W. Zhang, "Teaching the fundamentals of pulsed NMR spectroscopy in an undergraduate physical chemistry laboratory," *J. Chem. Educ.*, vol. 78, p. 956, 2001.

[187] C. Barmet, N. D. Zanche, and K. P. Pruessmann, "Spatiotemporal magnetic field monitoring for MR," *Magn. Reson. Med.*, vol. 60, pp. 187–197, 2008.

[188] C. Barmet, N. De Zanche, B. J. Wilm, and K. P. Pruessmann, "A transmit/receive system for magnetic field monitoring of *in vivo* MRI," *Magn. Reson. Med.*, vol. 62, pp. 269–276, 2009.

[189] B. T. Saam and M. S. Conradi, "Low frequency NMR polarimeter for hyperpolarized gases," *J. Magn. Reson.*, vol. 134, pp. 67–71, 1998.

[190] S. R. Parnell, E. B. Woolley, S. Boag, and C. D. Frost, "Digital pulsed NMR spectrometer for nuclear spin-polarized $^3$He and other hyperpolarized gases," *Meas. Sci. Technol.*, vol. 19, p. 045601, 2008.

[191] J. Yun, J. Yu, T. Hongyan, and L. Gengying, "A complete digital radio-frequency source for nuclear magnetic resonance spectroscopy," *Rev. Sci. Instrum.*, vol. 73, pp. 3329–3331, 2002.

[192] S. Handa, T. Domalain, and K. Kose, "Single-chip pulse programmer for magnetic resonance imaging using a 32-bit microcontroller," *Rev. Sci. Instrum.*, vol. 78, p. 084705, 2007.

[193] K. Takeda, "A highly integrated FPGA-based nuclear magnetic resonance spectrometer," *Rev. Sci. Instrum.*, vol. 78, p. 033103, 2007.

[194] L. Gengying, J. Yu, Y. Xiaolong, and J. Yun, "Digital nuclear magnetic resonance spectrometer," *Rev. Sci. Instrum.*, vol. 72, pp. 4460–4463, 2001.

[195] S. Jie, X. Qin, L. Ying, and L. Gengying, "Home-built magnetic resonance imaging system (0.3 T) with a complete digital spectrometer," *Rev. Sci. Instrum.*, vol. 76, p. 105101, 2005.

[196] W. Tang and W. Wang, "A single-board NMR spectrometer based on a software defined radio architecture," *Meas. Sci. Technol.*, vol. 22, p. 015902, 2011.

[197] W. K. Peng, L. Chen, and J. Han, "Development of miniaturized, portable magnetic resonance relaxometry system for point-of-care medical diagnosis," *Rev. Sci. Instrum.*, vol. 83, p. 095115, 2012.

[198] K. Takeda, "OPENCORE NMR: Open-source core modules for implementing an integrated FPGA-based NMR spectrometer," *J. Magn. Reson.*, vol. 192, pp. 218–229, 2008.

[199] C. A. Michal, "A low-cost spectrometer for NMR measurements in the earths magnetic field," *Meas. Sci. Technol.*, vol. 21, p. 105902, 2010.

[200] P. Nath, C. K. Chandrana, D. Dunkerley, J. A. Neal, and D. Platts, "The shim-a-ring magnet: Configurable static magnetic fields using a ring magnet with a concentric ferromagnetic shim," *Appl. Phys. Lett.*, vol. 102, p. 202409, 2013.

[201] G. Bodenhausen, R. Freeman, G. A. Morris, R. Niedermeyer, and D. L. Turner, "A simple approach to single-channel quadrature detection," *J. Magn. Reson.*, vol. 25, pp. 559–562, 1977.

[202] The GTK+ project, http://www.gtk.org.

[203] R. Kaptein, K. Dijkstra, and C. E. Tarr, "A single-scan fourier transform method for measuring spin-lattice relaxation times," *J. Magn. Reson.*, vol. 24, pp. 295–300, 1976.

[204] S. Meiboom and D. Gill, "Modified spin–echo method for measuring nuclear relaxation times," *Rev. Sci. Instrum.*, vol. 29, pp. 688–691, 1958.

[205] A. E. English, K. P. Whittall, M. L. G. Joy, and R. M. Henkelman, "Quantitative two-dimensional time correlation relaxometry," *Magn. Reson. Med.*, vol. 22, pp. 425–434, 1991.

# APPENDIX A

# SUPPORTING INFORMATION FOR "HYPERPOLARIZED HADAMARD SPECTROSCOPY USING FLOW NMR"*

## A.1 Hadamard Decoding Using Entropy Maximization

In conventional Hadamard spectroscopy, spectra are reconstructed using the Hadamard transform, which consists of recombining the acquired spectra by addition or subtraction. This process relies on having observed equal intensities in the different scans. In the hyperpolarized Hadamard spectroscopy as used here here, unequal intensity due to spin relaxation and concentration gradient prevents direct reconstruction. We propose to solve this issue by re-scaling each of the acquired scans prior to applying the Hadamard transform. If all observed spins exhibit the same $T_1$ relaxation, and therefore the intensity in the spectra varies uniformly, reconstruction would be perfect. In the case of unequal spin-relaxation, signal cancellation by subtraction cannot be complete in all locations in the spectra. Therefore, it is necessary to find optimal scaling parameters that minimize unwanted signals. This task can be achieved using entropy maximization (MaxEnt), as described in the main text. To verify the proposed method, simulations were carried out, using parameters modified from those in the experiments. Several scenarios are considered and examined, including the presence of spectral overlap, different variability of $T_1$ time constants, and signal-to-noise (SNR) ratio (Figures A.1 – A.5).

*Reprinted from "Hyperpolarized Hadamard Spectroscopy Using Flow NMR" by H. Y. Chen and C. Hilty, *Anal. Chem.*, **2013**, Copyright 2013 American Chemical Society

## A.2 Simulated Hadamard Spectra and Decoding Processing Using Entropy Maximization

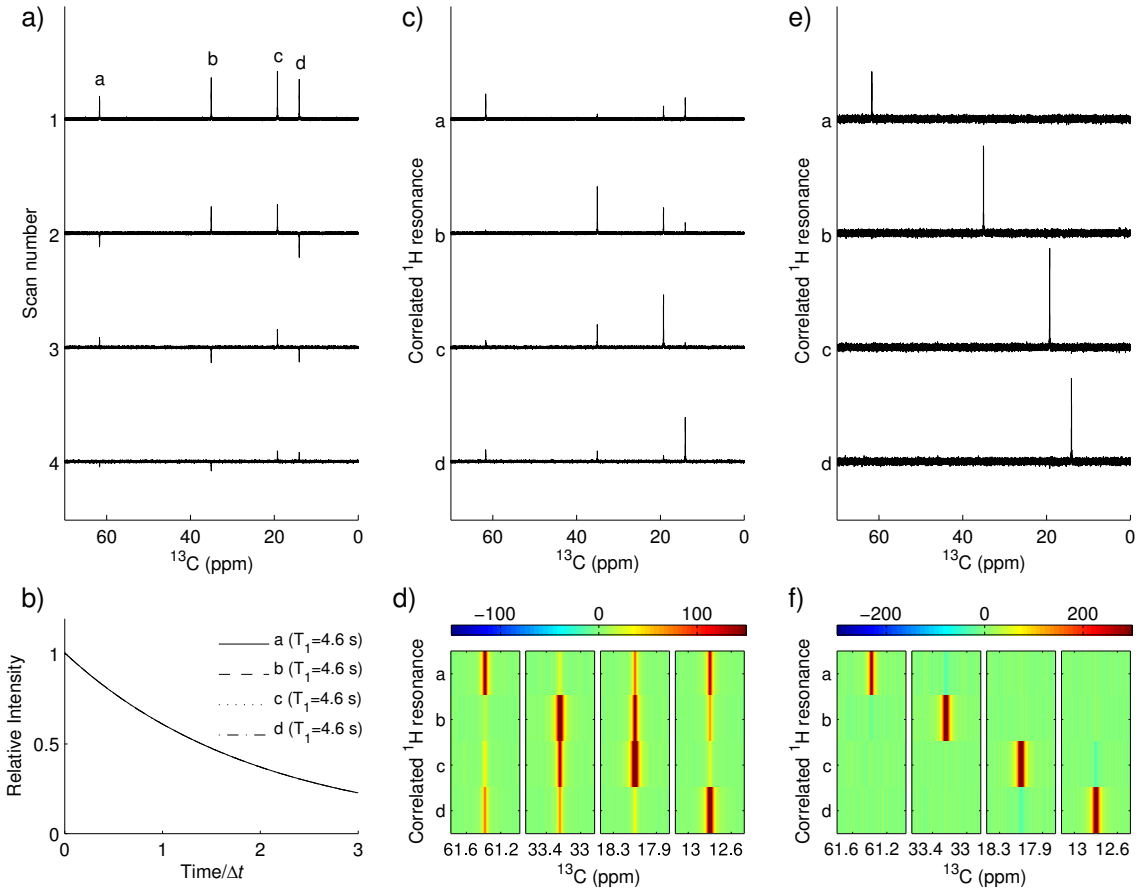


Figure A.1: Simulated Hadamard data assuming equal $T_1$ relaxation for each resonance. a) Simulated Hadamard encoded spectra. The average SNR in the first scan is chosen to be ~40. b) Decay of signal intensity due to $T_1$ relaxation. The relaxation rate chosen for each spin is indicated in the figure. c) The corresponding Hadamard decoded spectra without using MaxEnt rescaling. d) Strips of the pseudo-2D spectrum of (c). e) The decoded spectra using MaxEnt rescaling. f) Strips of the pseudo-2D spectrum of (e).

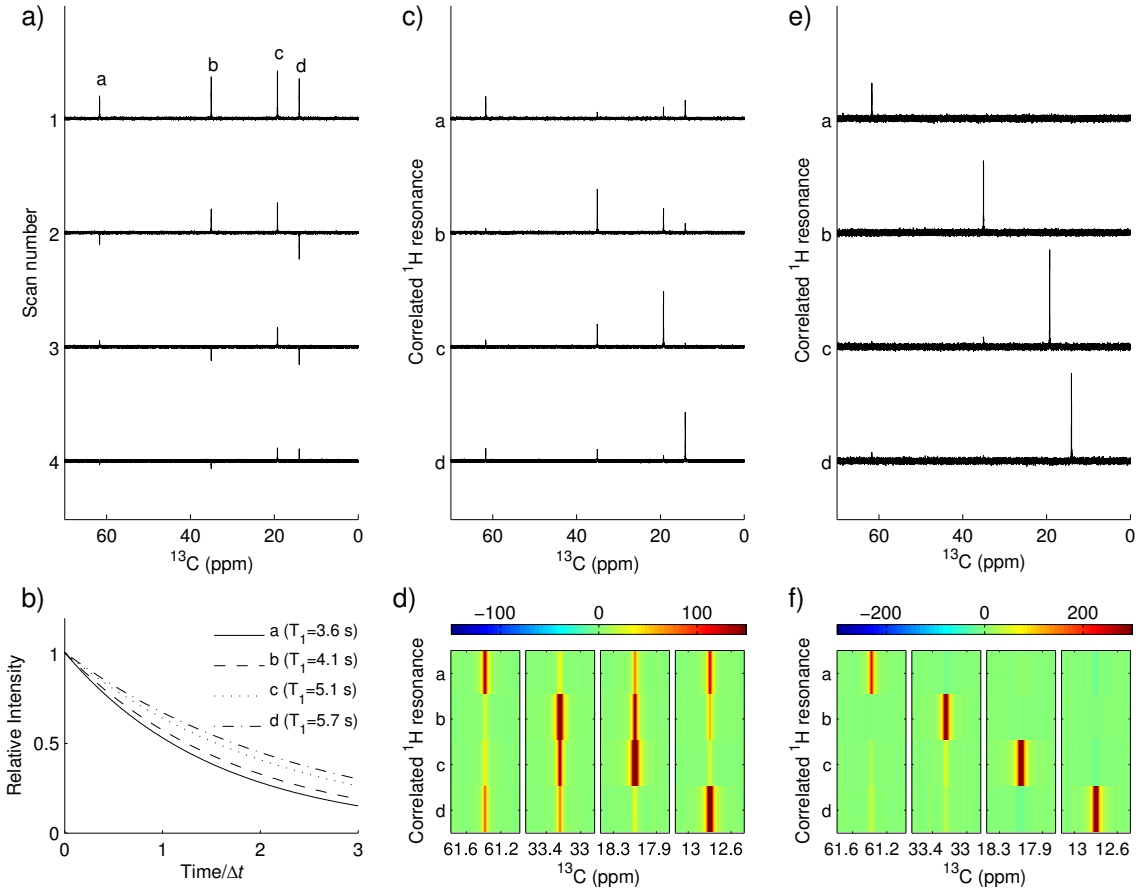


Figure A.2: Simulated Hadamard data for $T_1$ relaxation rates similar to those in the experiment. a) Simulated Hadamard encoded spectra. b) Decay of signal intensity due to $T_1$ relaxation. The relaxation rate chosen for each spin is indicated in the figure. c) The corresponding Hadamard decoded spectra without using MaxEnt rescaling. d) Strips of the pseudo-2D spectrum of (c). e) The decoded spectra using MaxEnt rescaling. f) Strips of the pseudo-2D spectrum of (e).

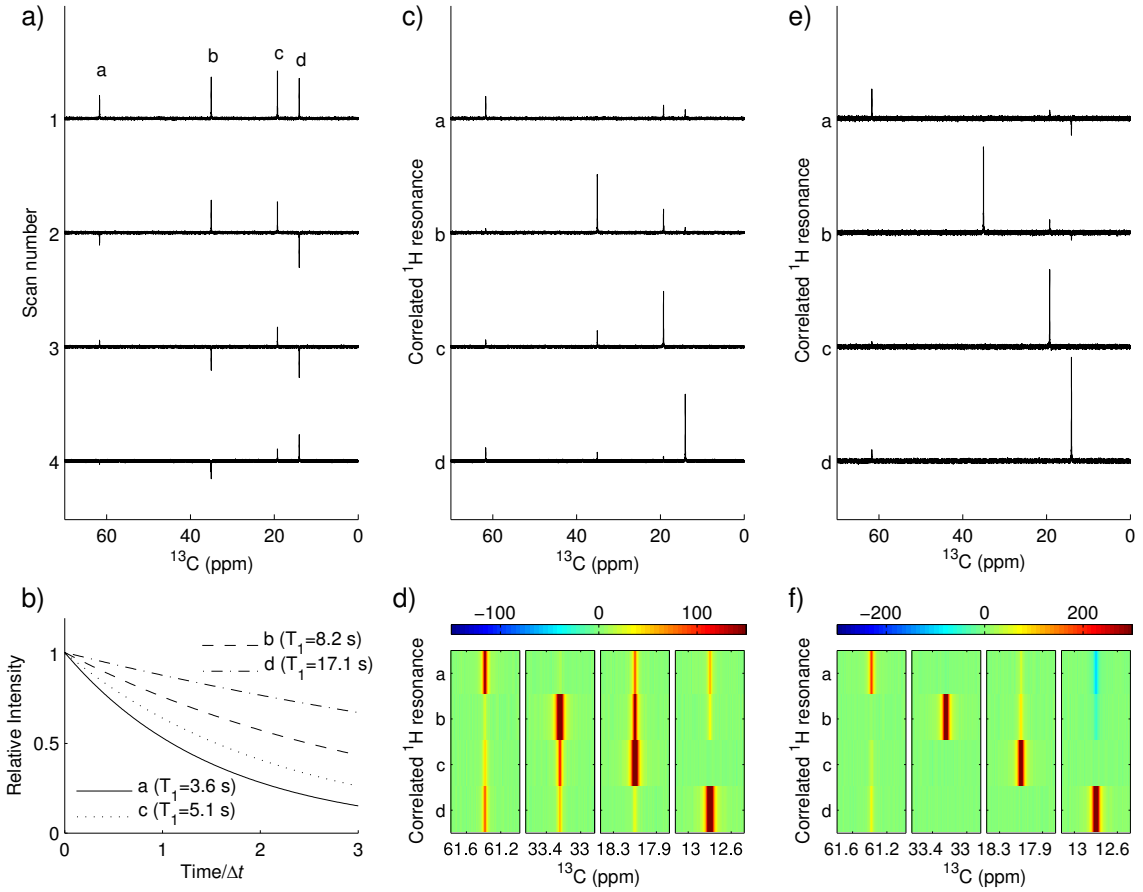


Figure A.3: Simulated Hadamard spectra with larger distribution of $T_1$ relaxation rates than in the experiment. a) Simulated Hadamard encoded spectra. b) Decay of signal intensity due to $T_1$ relaxation. The relaxation rate chosen for each spin is indicated in the figure. c) The corresponding Hadamard decoded spectra without using MaxEnt rescaling. d) Strips of the pseudo-2D spectrum of (c). e) The decoded spectra using MaxEnt rescaling. f) Strips of the pseudo-2D spectrum of (e).

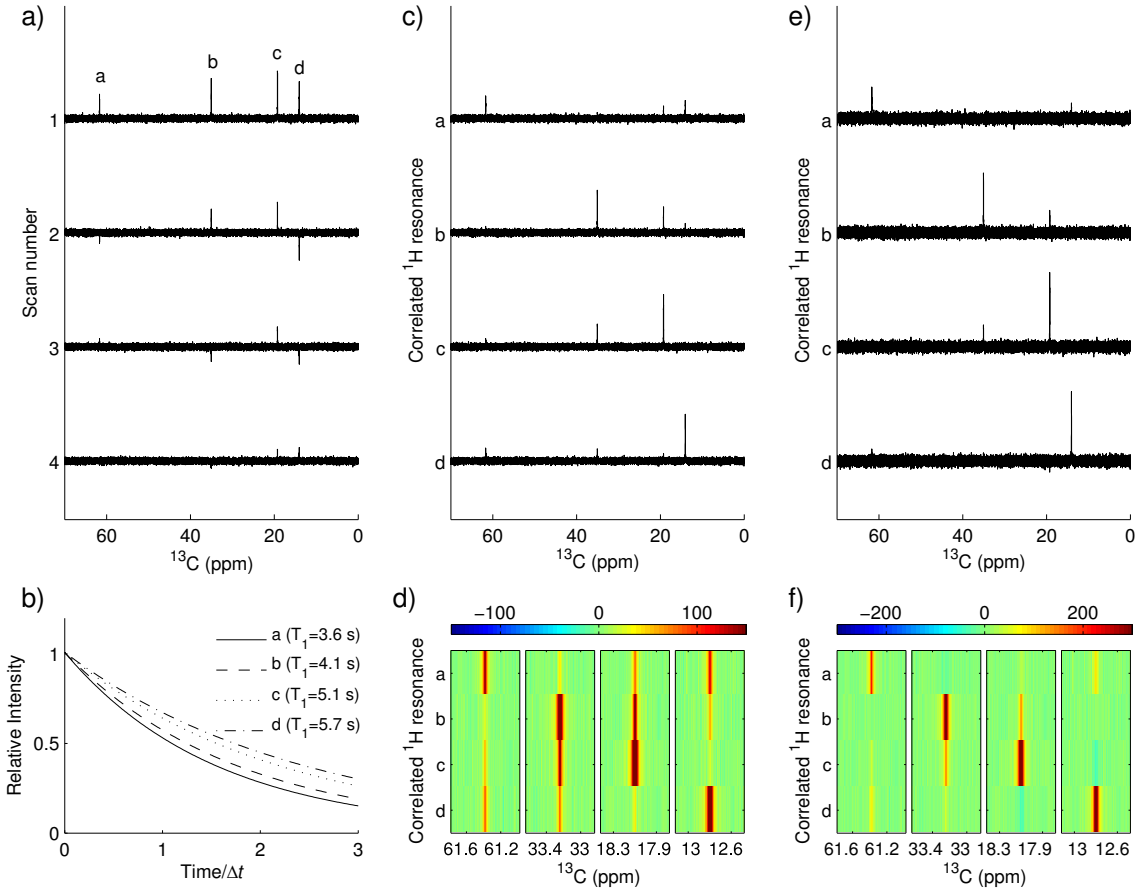


Figure A.4: Simulated Hadamard spectra with low signal-to-noise ratio. a) Simulated Hadamard encoded spectra. The average SNR in the first scan is chosen to be ~10. b) Decay of signal intensity due to $T_1$ relaxation. The relaxation rate chosen for each spin is indicated in the figure. c) The corresponding Hadamard decoded spectra without using MaxEnt rescaling. d) Strips of the pseudo-2D spectrum of (c). e) The decoded spectra using MaxEnt rescaling. f) Strips of the pseudo-2D spectrum of (e).

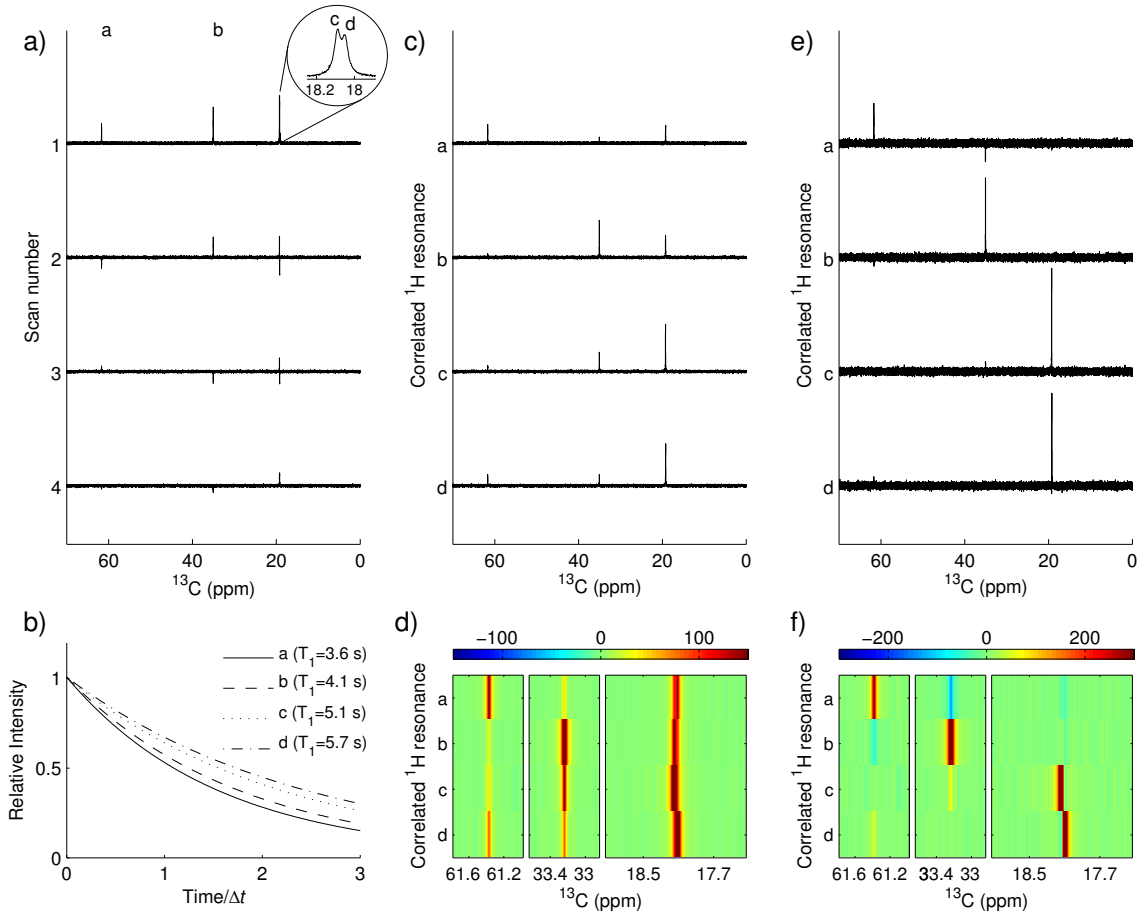


Figure A.5: Simulated Hadamard spectra in the presence of overlapping resonances. a) Simulated Hadamard encoded spectra. b) Decay of signal intensity due to $T_1$ relaxation. The relaxation rate chosen for each spin is indicated in the figure. c) The corresponding Hadamard decoded spectra without using MaxEnt rescaling. d) Strips of the pseudo-2D spectrum of (c). e) The decoded spectra using MaxEnt rescaling. f) Strips of the pseudo-2D spectrum of (e).

APPENDIX B

SUPPORTING INFORMATION FOR "FLOW-INJECTION FOR DISSOLUTION DYNAMIC NUCLEAR POLARIZATION"

One-dimensional image acquired using pulse field gradient spin echo sequence (PFGSE) was used to investigate the sample filling in the flow cell. Figure B.1 shows images obtained with a z-gradient strength of 0.014 T/m. In an ideal filling with no bubbles present in the cell, the smooth feature in the image (dashed line) was observed. However, if having air bubbles trapped, the image often shows the feature of unevenness.

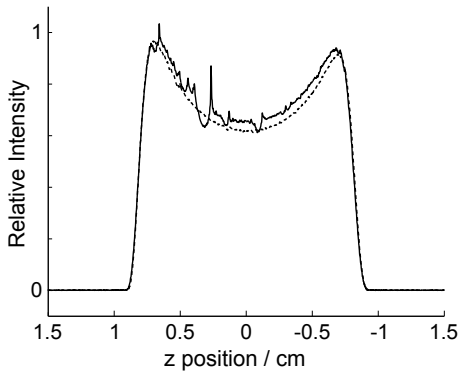


Figure B.1: 1D images obtained by using a pulse field gradient spin echo sequence. An image containing irregularities, presumably due to gas bubbles (solid line) is superimposed with a homogeneous profile (dashed line).

Figure B.2b shows the echo trains from the first four readouts ($m$=1 – 4) by applying the pulse sequence (Fig. B.2a) on a stationary water sample. The acquisition parameters are included in the main article. The different indices $n$ refer to different degrees of winding in the magnetization helix, which is typically quantified by the wavenumber, $k = \gamma G_z t_n/(2\pi)$. Here, $t_n$ is the time between the pulses $\alpha_n$ and $\pi/2$ storage pulse and is

equal to $n\delta + \delta_d$ ($n = N$ for the first pulse and $n = 1$ for the last pulse). The $\gamma$ and $G_z$ are the gyromagnetic ratio of nucleus in interest and the gradient strength along the $B_0$ field applied during the measurement. As an example, Figure B.2c shows the signal attenuation of stimulated echoes with different $k$. Diffusion coefficients derived from data (as selected shown in Fig. B.2c) are summarized in Figure B.2d. The values converge to the self-diffusion coefficient of $H_2O$ at 298 K.

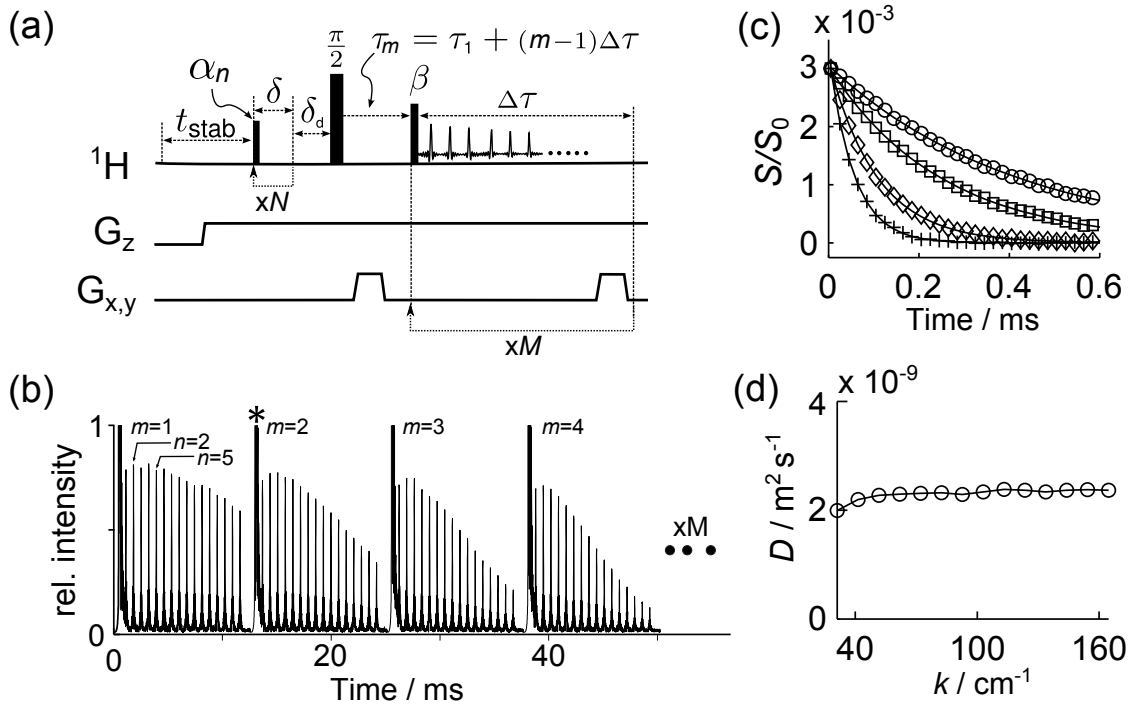


Figure B.2: a) Pulse sequence for diffusion measurement in a single scan[c]. b) The first four stimulated echo trains obtained from a stationary sample of $H_2O$. Symbol $*$ indicates FID directly originated from the application of pulse, $\beta$. c) Amplitude of selected echoes from the same winding of magnetization helices ($S/S_0$) as a function of time ($\circ$: $k$=31.4 cm$^{-1}$, $\square$: $k$=52.3 cm$^{-1}$, $\diamond$: $k$=94.0 cm$^{-1}$, +: $k$=135.7 cm$^{-1}$). Solid lines are fit results obtained using the Equation 4 in the main text. d) Diffusion coefficients ($D$) obtained from the data shown in part in (c).

When using liquid driven injector, a correct timing to switch the V2 (Fig. 5a in the main article) is of importance for achieving the optimal mixing of the hyperpolarized solution and the second sample. The instant color change of a pH indicator is employed as a tool for this purpose. Reagents used to determine the injection parameter ($t_{mix}$) include the bromophenol blue prepared in 10 mM citrate buffer, pH=6 (reagent A) and 200 mM citrate buffer, pH=3 (reagent B). The reagent A is used as an analogue of HP samples in test injections. When 10 $\mu$L of reagent A is mixed with the reagent B at correct timing, the instant color change from purple to yellow resulting from pH jump can be clearly observed as shown in Figure B.3. On the other hand, if the reagent B is injected too late, both blue and yellow color will be observed. The mixing ratio of two reagents is, however, determined by NMR signals from samples added in each reagents.

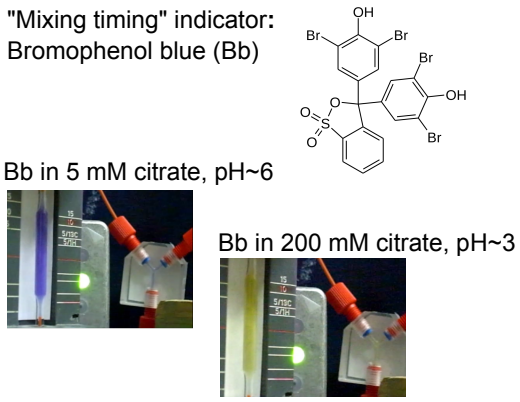


Figure B.3: Distinct color change of bromophenol due to a pH change upon mixing was employed to determine the timing for injection of the non-hyperpolarized sample in loop L2.

[c] S. Peled et al., *J. Magn. Reson.*, vol. 140, pp. 320–324, 1999.
J. Granwehr et al., *J. Chem. Phys.*, vol. 132, pp. 244507–244513, 2010.

APPENDIX C

# SUPPORTING INFORMATION FOR "AN ULTRA-LOW COST NMR DEVICE WITH ARBITRARY PULSE PROGRAMMING"

The spectrometer is optimized for maximum flexibility by implementing most functions within the FPGA. The associated electronics still required consists primarily of amplifiers for both radio-frequency (RF) and low-frequency (LF), LF bandpass filters, RF mixers and LF signal level shifters. The schematic is presented in Figure 6.2 in the main article. The following supporting Tables and Figures details the analog circuits for associated functions and corresponding costs.

## C.1 Circuit Block Diagrams

*1. LF amplifier (element #8 in Figure 6.2)*

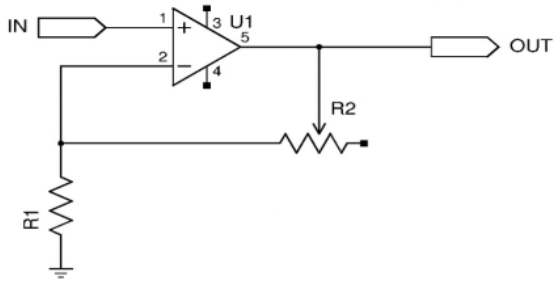


Figure C.1: Low-frequency amplifier used after down-conversion of NMR signal. (Gain: 1+R2/R1).

| Name | Attributes |
|---|---|
| R1 | 1k Ω |
| R2 | 33-500 kΩ |
| U1 | OPA-37 |

*2. RF signal amplifier (element #1 in Figure 6.2)*

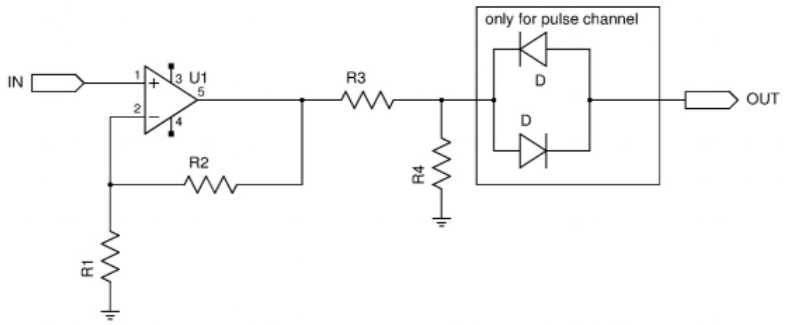


Figure C.2: Radio-frequency output stage. Here, the signal input is directly from DE0 education board.

| Name | Attributes for pulse channel | Attributes for reference channel |
|---|---|---|
| R1 | 500 Ω | 1 kΩ |
| R2 | 1 kΩ | 500 Ω |
| R3 | 50 Ω | 50 Ω |
| R4 | 50 Ω | 25 Ω |
| D | 1N4148 | 1N4148 |
| U1 | MAX4383EUD+ | MAX4383EUD+ |

*3. On-board RF preamplifier (element #5 in Figure 6.2)*

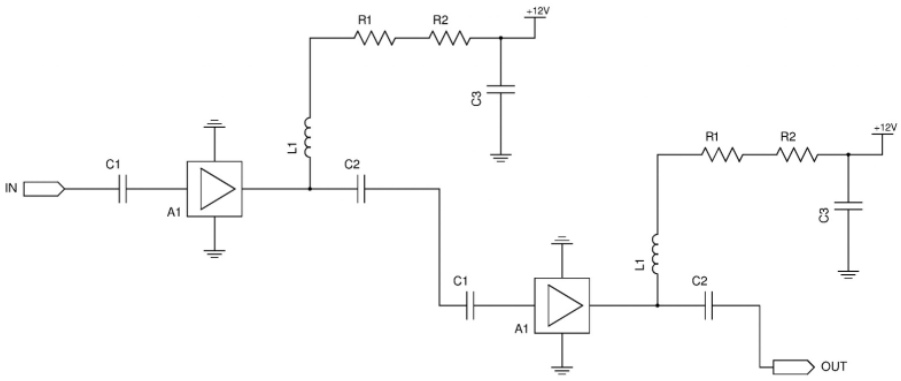


Figure C.3: Radio-frequency preamplifier.

| Name | Attributes |
|---|---|
| C1 | 2400 pF |
| C2 | 2400 pF |
| C3 | 100 nF |
| R1 | 523 Ω |
| R2 | 8.25 Ω |
| L1 | TCCH-80+ (Minicircuits) |
| A1 | MAR-6SM+ (Minicircuits) |

*4. LF bandpass filter (element #7 in Figure 6.2)*

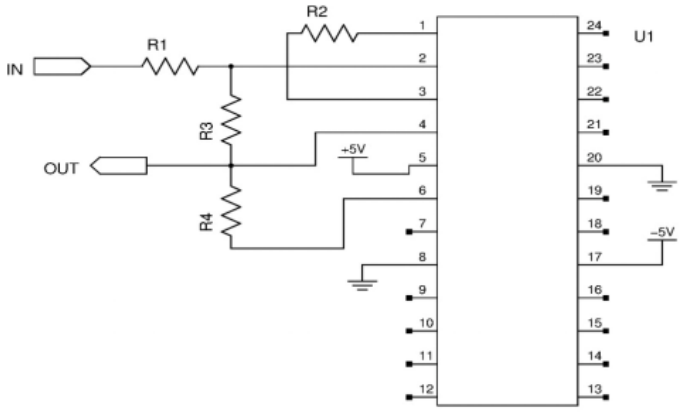


Figure C.4: Low-frequency bandpass filter. One MAX274 can serve four channels. Equivalent pins: 1=12=13=24, 2=11=14=23, 3=10=15=22, 4=9=16=21, 6=7=18=19. For different filter designs, a simulation software is provided by Maxim Integrated. The bandwidths for 10 kHz and 50 kHz filter are 7 kHz and 75 kHz (±3dB), respectively.

| Name | Attributes (for 10/50 kHz center frequency and Q=2/1) |
|---|---|
| R1 | 60 kΩ/6 kΩ |
| R2 | 200 kΩ/40 kΩ |
| R3 | 80 kΩ/8 kΩ |
| R4 | 195 kΩ/35 kΩ |
| U1 | MAX274 (Maxim Integrated) |

*5. Low-frequency level shifter (element #9 in Figure 6.2)*

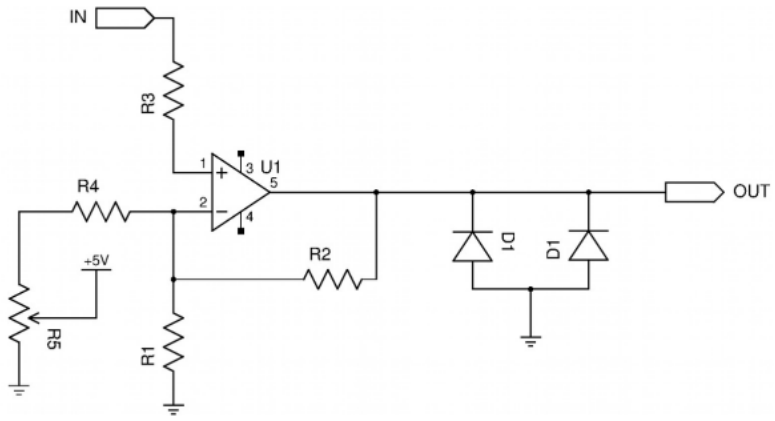


Figure C.5: Level shifter is used to ensure the input is non-negative for DE0 input. The Zener diodes (D1) are used to avoid spurious high voltage.

| Name | Attributes |
|---|---|
| R1 | 1.5 kΩ |
| R2 | 500 Ω |
| R3 | 1.5 kΩ |
| R4 | 2.6 kΩ |
| R5 | 2 kΩ |
| D1 | 1N4729A |
| U1 | OPA-27 |

## C.2 Cost of Major RF Components

Table C.1 : Major RF/LF components for each transmit and receiver channel and the corresponding cost.

| Item | Product number | Cost (USD) |
|---|---|---|
| DE0-NANO Evaluation Board | P0082 | $90 |
| CMOS signal amplifier | MAX4384EUD+ | $17.2 |
| RF bandpass filter | PBP-21.4+ | $21.2 |
| Pulse amplifier | ZHL-3A+ | $229 |
| Tx/Rx switch[1] | ZX80-DR230+ | $59.95 |
| Low noise preamplifier[2] (external) | ZFL-500LN+ | 79.95 |
| Low noise preamplifier (surface mount)[2] | | |
| - -Wideband amplifier | - -MAR-6SM+ | $1.21 |
| - -RF choke | - -TCCH-80+ | $3.45 |
| CMOS signal amplifier | ADE-1L | $3.95 |
| RF bandpass filter | MAX274A | $14.37 |
| LF signal amplifier[1] | OPA-37 | $3.1 |
| CMOS level shifter[1] | OPA-27 | $3.2 |

Note:
1. One for each Rx channel.
2. Typically, two sets of the components are used for a single Rx channel.
3. One of MAX274A chips provides the filter function for two Rx channels.